THE UNIVERSITY OF HULL

Towards an *ab Initio* Description of Adsorbate Vibrations

by

Sergey Chulkov

A thesis submitted in partial fulfilment

of the requirements for the degree of

Doctor of Philosophy

in the University of Hull

November, 2013

Abstract

This thesis investigates accurate theoretical prediction of anharmonic vibrational frequencies of molecules adsorbed on metal surfaces. Such adsorbed systems are composed of two parts with different electronic properties, the adsorbate and the surface. However, most existing quantum mechanical methods are not identically accurate for both parts. Moreover, methods that can accurately describe extended system are very time consuming and significantly complicates their usage for standard anharmonic calculations.

This thesis introduces a fragment method to overcome this difficulty. Within our method an energy correction is computed using high-level *ab initio* quantum mechanical method by considering an adsorbed molecule separately from the metal surface. The reliability of this approach is demonstrated for two test systems: an acetylene molecule adsorbed on a Cu(001) surface and a thiophene molecule adsorbed on a Au(111) surface. In both cases intra-adsorbate anharmonic frequencies obtained using the fragment method show better agreement with experimental data than the corresponding anharmonic frequencies computed using a standard approach. Moreover, a correlation between the accuracy of the fragment method and the accuracy of the *ab initio* method used for adsorbed molecule is observed. This correlation provides a way to systematically improve adsorbate frequencies by improving the quality of the potential energy surface used.

Finally, for each test systems we established a correlation between the strength of adsorption and the value of the frequencies shift upon adsorption. This allows us to conclude that terthiophene is only weakly adsorbed on a Au(111) surface based on the similarity between the adsorbate and the gas-phase vibrational spectra.

Keywords: quantum chemistry, vibrational spectroscopy, anharmonicity, fragment methods, adsorbate vibrations, ab initio calculations.

Contents

Chapter 1

Introduction

Molecules adsorbed on metal surfaces remain a current theoretical interest. Adsorption is normally classified into two types according to the type of binding. The first type is physisorption, which is caused by weak van der Waals interactions between an adsorbed molecule and its metallic support. Physisorption is a reversible process that usually does not alter molecular geometry and usually does not alter much the local structure of the surface near its adsorption site. However, this type of adsorption is non-specific to the particular adsorbate and the metallic surface and can be observed at low temperature for almost all adsorbed systems.

The second type of adsorption is chemisorption when a molecule forms chemical bonds with the adsorbent. In contrast with physisorption, chemisorption is usually highly selective. In particular, catalytic properties of metallic surfaces are defined by their ability to chemisorb as this often enhances the reactivity of adsorbed molecules by altering their conformations, or changing their electronic distribution [1]. For this reason, information about adsorbate's equilibrium geometry as well as about its adsorption site becomes very important, as it provides a better understanding of catalytic reactions induced by metallic surfaces and gives the ability to control them.

There are a number of experimental techniques, such as scanning tunnelling microscopy (STM) [2] and low energy electron diffraction (LEED) [3, 4], which can provide direct information about the structure of such adsorbed systems. However, in the case of a large adsorbed molecule it is still very difficult to observe experimentally

an actual adsorption site, as the structure of metallic support is covered by adsorbates. The situation becomes more involved as chemisorption affects not only the adsorbed molecule but often leads to reorganisation of the surface structure itself. Fortunately, this kind of information can potentially be obtained from the analysis of vibrational spectra, as these spectra contain important information not only about the system's constituents but also about its actual molecular geometry. For adsorbed systems vibrational spectroscopy also probes the arrangement of molecules on a surface [5] that may be inaccessible by other methods.

There are several experimental techniques that have been developed to record vibrational spectra of adsorbed molecules, such as (high resolution) electron energy loss spectroscopy (HR)EELS [6, 7], infrared reflection absorption spectroscopy (IRRAS) [8, 9], surface enhanced Raman spectroscopy (SERS) [10], inelastic electron tunnelling spectroscopy (IETS) [11], and many others. Moreover, the IETS technique combined with STM also allows one to record the vibrational spectra of a specific part of a complex molecule [12]. Nevertheless, the assignment of measured transition frequencies to certain vibration modes still remains a very difficult task.

There are four commonly used approaches to perform this assignment. The first one is based on characteristic vibrational frequencies which implies that the vibrational motion of some group of atoms has a similar frequency in different molecules. However, these characteristic frequencies often lie within widely overlapping intervals of possible values, and the precise value strongly depends on the actual molecular conformation and environment [13]. Furthermore, vibrational overtones from various functional groups may appear in the vicinity of fundamental frequencies of other functional groups, making the spectra even more difficult to interpret. In connection with adsorbed systems this excessive sensitivity, however, is a very promising feature of vibrational spectroscopy, as it potentially allows to distinguish between different adsorption sites [14].

The second widely used approach is based on an isotopic effect. Thus, the replacement of a given atom with its isotope affects the transition frequencies of those vibrational modes which involve the replaced atom. The value of such

isotopic shift can be estimated theoretically using a classical oscillator model. The peaks in the target spectrum that experience this shift can be easily identified. Unfortunately, a complete analysis of a vibrational spectrum using this approach may be very expensive and time consuming, as it requires the synthesis of many different isotopomers. Moreover, separate vibrational spectra need to be measured for all of these isotopomers.

Alternatively, in gas phase conditions peaks can also be assigned to a particular mode based on different selection rules which take place for different experimental techniques. For example, the fact that IR and Raman spectra of molecules with an inversion centre are complementary to each other can be used to assign a particular symmetry along the inversion centre for every peak. However, in case of adsorbed systems many other factors have to be taken into account and complicate the assignment process based on selection rules. Persson and Baratoff [15] theoretically proved that IETS can potentially detect all vibrational transitions of an adsorbate molecule. However, the majority of peaks have low intensity due to "propensity rules" [16, 17] and they are hidden by a noise signal. These propensity rules are complex and depend on many factors such as a molecular symmetry, the symmetry of molecular orbitals involved in each tunnelling channel, the type of vibration, and experimental conditions [16]. The variety of these factors can prevent a reliable interpretation of spectra and often means that we need to use additional sources of information.

Finally, the vibrational modes can be assigned using theoretical simulations. Nowadays it is massively used for interpretation of vibrational spectra as it does not require extra experiments. It provides a way not only to do mode assignment but also allows to recover some structural data from a vibrational spectrum by comparing calculated spectra of possible structures with experiment [14]. The standard framework for such theoretical predictions is the harmonic approximation. Its popularity originates from the fact that its computational demands grow linearly with the number of atoms. This is especially important for adsorbed systems as often, in order to simulate them properly, hundreds of atoms should be taken into

consideration. Unfortunately, the direct comparison between experimental and harmonic frequencies is rarely possible, as these harmonic frequencies are usually significantly overestimated. This overestimation is caused by the lack of anharmonicity and in case of molecules in the gas phase can reach up to 15% [18, 19]. Moreover, anharmonicity is also very important for adsorbed systems including systems with weak molecule–surface interaction [20].

The simplest widely used technique to account for anharmonicity is to introduce empirical scaling factors that are dependent on the particular *ab initio* method/basis set used and the type of vibration [21]. This approach relies on transferability of the scaling factors and was tested only for a relatively small set of molecules in the gas phase. However, the question about its applicability to adsorbed systems still remains open.

An important alternative to scaling factors to account for anharmonic effects are approaches based on the vibrational self consistent field (VSCF) method [22], such as (degeneracy-corrected) second order Møller–Plesset perturbation theory ((DC)VMP2) [23, 24], vibrational configuration interactions (VCI) [25], vibrational coupled clusters (VCC) [26], and perturbation selected interactions VCI (VCIPSI) [27]. These methods are analogous to the corresponding ones from electronic structure theory, and provide a fully quantum mechanical description of the nature of the anharmonicity. They also provide a regular way to improve the accuracy, by increasing the quality of used potential energy surface (PES) and the level of theory.

The thesis is organised as following. Chapter 2 contains a brief introduction into the theory of molecular vibrations. Chapter 3 discusses methods of electronic structure theory and basic principles of fragment methods. It also describes a method adapted to improve the accuracy of a PES in case of adsorbed systems. Chapter 4 describes algorithmical aspects of my own implementation of general m-dimensional VSCF and VCI solvers. The proposed fragment method is tested on an acetylene molecule adsorbed on a Cu(100) surface (Chapter 5) and on a thiophene molecule adsorbed on a Au(111) surface (Chapter 6) Finally, Chapter 7 summarises the obtained results.

Chapter 2

The theory of molecular vibrations

According to the quantum chemistry, a molecule can be thought as a collection of positively charged nuclei and negatively charged electrons with electrostatic interactions between them. The stationary properties of such system are fully described by a wave function $\Psi(\mathbf{r}, \mathbf{R})$ which depends on the positions of all nuclei ($\mathbf{R}$) and electrons ($\mathbf{r}$). This wave function also depends on the spin of the electrons, but for the purpose of simplicity this dependence is not indicated explicitly.

The wave function $\Psi(\mathbf{r}, \mathbf{R})$ and the corresponding energy E are obtained by solving the time-independent non-relativistic Schrödinger equation:

$$\hat{H}\Psi(\mathbf{r}, \mathbf{R}) = E\Psi(\mathbf{r}, \mathbf{R}) \tag{2.1}$$

which is totally determined by a Hamiltonian operator $\hat{H}$. This operator describes interactions between particles which forms a molecular system and for this reason it is unique for every molecular system. The Hamiltonian contains kinetic energy operators of the nuclei ($\hat{T}_n$) and the electrons ($\hat{T}_e$), as well as an electron-nucleus attraction ($\hat{V}_{en}$) operator along with electron-electron ($\hat{V}_{ee}$) and nucleus-nucleus ($\hat{V}_{nn}$) repulsion operators. In case of the molecular system composed from N_a nuclei and

N_e electrons, it has the following form:

$$\hat{H} = \underbrace{-\frac{1}{2}\sum_{\alpha}^{N_a}\frac{1}{M_\alpha}\nabla_\alpha^2}_{\hat{T}_n} \underbrace{+\sum_{\alpha<\beta}^{N_a,N_a}\frac{Z_\alpha Z_\beta}{|\mathbf{R}_\alpha-\mathbf{R}_\beta|}}_{\hat{V}_{nn}} \underbrace{-\frac{1}{2}\sum_{i}^{N_e}\nabla_i^2}_{\hat{T}_e} \underbrace{+\sum_{i<j}^{N_e,N_e}\frac{1}{|\mathbf{r}_i-\mathbf{r}_j|}}_{\hat{V}_{ee}} \underbrace{-\sum_{\alpha,i}^{N_a,N_e}\frac{Z_\alpha}{|\mathbf{R}_\alpha-\mathbf{r}_i|}}_{\hat{V}_{en}} \tag{2.2}$$

where Z_α is the charge of the α-th nucleus and M_α is its mass in atomic units [1].

Usually there are many wave functions that satisfy the Schrödinger equation (2.1) for a particular Hamiltonian. Each of them represents some nuclear-electronic state of the molecular system, while the total energy of this state is equal E. These energies aggregate to form a molecular spectrum which contains information about electronic, vibrational, and rotational transitions. For this reason, in order to simulate the vibrational spectra the vibrational component of the Hamiltonian operator $\hat{H}$ should be separated from the electronic and the rotational ones and then the obtained vibrational Schrödinger equation needs to be solved.

2.1 Born-Oppenheimer approximation

Solving of the Schrödinger equation (2.1) is a very laborious task, as it depends on many variables. In particular, the molecular Hamiltonian [Eq. (2.2)] contains the term $\hat{V}_{en}$ which couples nuclei and electrons together. Without this term, the Hamiltonian could be decomposed into the sum of two "reduced" Hamiltonians; one depending on nuclear coordinates, while the other depends on electronic coordinates only. This leads to a separation of the original Schrödinger equation into electronic and nuclear equations of lesser dimensionality, which depend on their own disjoint set of coordinates. Once solving these two equations, the total energy can be computed as a sum of electronic and nuclear energies, and the total wave function expressed as a product of the corresponding electronic and nuclear wave functions.

However, in reality the operator $\hat{V}_{en}$ cannot be ignored, as it is responsible for interaction between nuclei and electrons. Nevertheless, the ability to such separation

[1] e (elementary charge; 1.602×10^{-19} C) = m_e (electron mass; 9.109×10^{-31} kg) = a_0 (Bohr radius; 5.292×10^{-11} m) = $\hbar$ (reduced Planck constant; 1.055×10^{-34} J·s) = 1 a.u.

can be postulated within the Born-Oppenheimer approximation [28] in assuming that electrons instantly adapt to any alteration of nuclear positions. Thus, the total wave function of a molecular system is sought in a form of superposition of a nuclear $[\Psi_n(\mathbf{R})]$ and electronic $[\Psi_e(\mathbf{r};\mathbf{R})]$ wave functions:

$$\Psi(\mathbf{r},\mathbf{R}) \simeq \Psi_e(\mathbf{r};\mathbf{R})\Psi_n(\mathbf{R}). \tag{2.3}$$

The electronic wave function depends explicitly only on the electron coordinates ($\mathbf{r}$) and it is the solution of the electronic Schrödinger equation:

$$\hat{H}_e\Psi_e^k(\mathbf{r};\mathbf{R}) = \left\{\hat{T}_e + \hat{V}_{ee} + \hat{V}_{en}\right\}\Psi_e^k(\mathbf{r};\mathbf{R}) = E_e^k(\mathbf{R})\Psi_e^k(\mathbf{r};\mathbf{R}), \tag{2.4}$$

At the same time, the nuclear coordinates are considered as parameters which enumerate different electronic Schrödinger equations. This means that Eq. (2.4) should be thought as a set of equations; each of them corresponds to a particular fixed arrangement of the nuclei.

The electronic Schrödinger equation (2.4) can be solved using variety of methods developed within the electronic structure theory [29]. As the result, a set of electronic wave functions $\Psi_e^k(\mathbf{r};\mathbf{R})$ along with the corresponding electronic energies $E_e^k(\mathbf{R})$ are obtained. Being computed for different nuclear coordinates together with nuclear repulsion term, these electronic energies form a potential energy surface (PES):

$$\hat{V}^k(\mathbf{R}) = \hat{V}_{nn}(\mathbf{R}) + E_e^k(\mathbf{R}) \tag{2.5}$$

Once computed, this PES can be used within a nuclear Schrödinger equation for the k-th electronic state:

$$\hat{H}_n\Psi_n^{k,\gamma}(\mathbf{R}) = \left\{\hat{T}_n + \hat{V}^k\right\}\Psi_n^{k,\gamma}(\mathbf{R}) = E^{k,\gamma}\Psi_n^{k,\gamma}(\mathbf{R}). \tag{2.6}$$

This equation allows to determine wave functions $\Psi_n^{k,\gamma}(\mathbf{R})$ for various vibrational, translational, and rotational states (γ) along with the corresponding energies ($E^{k,\gamma}$).

From now on I will omit the index k for the purpose of simplicity, as this work is dominantly focused on molecules in their electronic ground states.

2.2 Elimination of translational and rotational motions

The different types of nuclear motions can be classified as internal and external ones. External motions represent movements of a molecular system as a whole, while internal ones represent the inter-atomic movements within the system. Thus, molecular vibrations – which are the main interest of this work – is an example of pure internal motion. As such, internal coordinates are better suited for their description rather than the regular Cartesian coordinates $\mathbf{R}$.

In addition to vibrational motion, the molecular system can also move as a whole along some trajectory in three-dimensional space. This translational motion does not affect inter-atomic distances and for this reason it corresponds to a pure external motion. As translations and vibrations correspond to different types of motion, it is possible to separate them completely by using a centre-of-mass frame instead of an original laboratory frame. The origin of this centre-of-mass frame is determined as:

$$R_{\mathrm{CM}} = \frac{\sum_{\alpha=1}^{Na} M_\alpha R_\alpha}{\sum_{\alpha=1}^{Na} M_\alpha}. \tag{2.7}$$

In fact, changing a coordinate system is equivalent to invent a new set of nuclear coordinates:

$$\boldsymbol{\Xi} = \{\xi_i\}_{i=1}^{3N_a} \equiv \{\tilde{R}_{\alpha x}, \tilde{R}_{\alpha y}, \tilde{R}_{\alpha z}\}_{\alpha=1}^{N_a}, \tag{2.8}$$

where the new coordinates are expressed using the old ones ($\mathbf{R}$) as follows:

$$\xi_i = \sum_{\beta=1}^{N_a} \left(c_{i;\beta x} R_{\beta x} + c_{i;\beta y} R_{\beta y} + c_{i;\beta z} R_{\beta z} \right). \tag{2.9}$$

A particular choice of the transformation coefficients $\{c_{i;\beta x}, c_{i;\beta y}, c_{i;\beta z}\}_{i=1\ldots3N_a}^{\beta=1\ldots N_a}$ solely depends on the transformation technique used.

Figure 2.1. A formaldehyde molecule in a laboratory Cartesian coordinate system (centre) and in two different centre-of-mass frames with Jacobi (left) and Cartesian (right) coordinates.

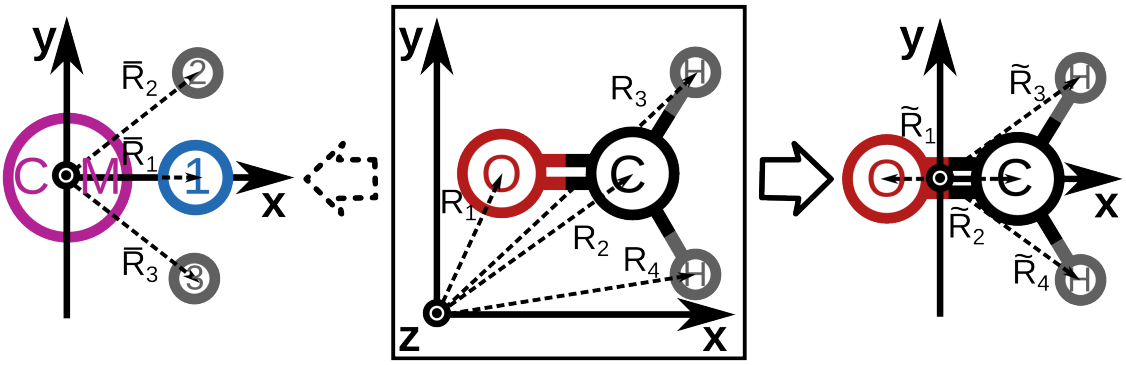

One way to perform this separation is to use Jacobi coordinates [30]. Within this framework, the original molecular system composed from N_a atoms is replaced by the system of N_a effective particles. The first particle represents the centre of mass of the molecular system which is involved into translational motion. The other $N_a - 1$ effective particles define positions of the real N_a nuclei about the centre of mass. As an advantage, the Jacobi coordinates allow to extract the kinetic energy of the centre of mass from the original nuclear Hamiltonian reducing its dimensionality by three. However, these coordinates are rarely used in practice for molecules with more than three atoms [31], as the original atoms do not longer exist in them (see Figure 2.1). However, changing the type of coordinates is not necessary at this stage. Instead, the origin of the laboratory frame can be simply shifted to the centre of mass. This trick does not reduce the dimensionality of the nuclear Hamiltonian immediately, but the translational coordinates are naturally separated during the resolution of the vibrational equation.

The molecular system may be also involved into rotation along some axis. However, in contrast with translations and vibrations, it is not possible to assign the rotational motion to a particular type according to external/internal classification. If we assume fixed inter-atomic distances, the molecular system would experience a rigid rotation. In this case it would be possible to separate this rotation from vibrations by bringing the axes of the centre-of-mass frame into coincidence with the principal inertia axes of the molecular system. With this approach, the rotation is fully described by three

Eulerian angles [32, p. 286], which are completely invariant from translational and vibrational motion. This particular selection of the coordinate system was firstly proposed by Eckart [33] and it is called an Eckart frame [34].

In real molecular systems, however, vibrations may have an influence on rotation by constantly altering its instantaneous angular momentum. At the same time, rotational motion can also distort the atomic vibrational trajectories by enforcing atoms to move in a perpendicular direction. This coupling between rotations and vibrations is called Coriolis interaction [35]. The strength of such interaction is usually small and can be ignored, which makes an approximate separation possible. It also should be mentioned, that separation of rotational motions is only needed in case of molecules in the gas phase. For periodic systems this separation is not required as this type of systems is not involved into rotation.

2.3 Harmonic approximation

Prior to solving the nuclear equation (2.6), a suitable set of vibrational coordinates has to be chosen. The reason is that the regular Cartesian coordinates do not represent the actual shape of vibrations in polyatomic molecules, as these vibrations primarily change the internal position of the atoms in a molecular system. Ideally, this set of coordinates also should be intuitive and should have a simple physical interpretation. As an example, a set of internal coordinates composed from interatomic distances, angles and dihedral angles can be used which together define a Z-matrix. This particular set of internal coordinates allows to classify molecular vibrations by types, such as stretching modes, bending modes, internal rotational modes, and others.

However, the number of such internal coordinates is less than the number of Cartesian coordinates by the number of translational and rotational degrees of freedom. In order to avoid degeneracy during coordinate transformation, the set of internal coordinates is usually completed by three Cartesian coordinates of the centre

of mass and by Eulerian angles in the Eckart frame which represent the translational and rotational motions respectively.

Once the set of internal coordinates $\mathbf{q} = \{q_i\}_{i=1}^{3N_a}$ has been chosen, the nuclear Hamiltonian expressed in Cartesian coordinates $\mathbf{\Xi} = \{\xi_i\}_{i=1}^{3N_a}$ in the Eckart frame:

$$\hat{H}_n = \hat{T}_n(\mathbf{\Xi}) + \hat{V}(\mathbf{\Xi}) = \sum_{i=1}^{3N_a} \frac{1}{2M_i} \frac{\partial^2}{\partial \xi_i^2} + \hat{V}(\xi_1, \ldots, \xi_{3N_a}) \tag{2.10}$$

needs to be rewritten in terms of these new internal coordinates $\mathbf{q}$. In order to do so, the old coordinates $\mathbf{\Xi}$ are expanded into Taylor series at the equilibrium point:

$$\xi_k = \xi_k^0 + \sum_{i=1}^{3N_a} \left(\frac{\partial \xi_k}{\partial q_i} \right)_0 q_i + \ldots . \tag{2.11}$$

If only the first two terms in the Taylor series [Eq. (2.11)] are taken into account, the kinetic part of the Hamiltonian in Eq. (2.10) expressed in $\mathbf{q}$ has the simplest form:

$$\hat{T}_n \simeq -\frac{1}{2} \sum_{i=1}^{3N_a} \sum_{j=1}^{3N_a} \left(\frac{1}{M_i M_j} \sum_{k=1}^{3N_a} \frac{\partial \xi_k}{\partial q_i} \frac{\partial \xi_k}{\partial q_j} \right) \frac{\partial}{\partial q_i} \frac{\partial}{\partial q_j} = -\frac{1}{2} \sum_{i=1}^{3N_a} \sum_{j=1}^{3N_a} g_{ij} \frac{\partial}{\partial q_i} \frac{\partial}{\partial q_j}. \tag{2.12}$$

Here, M_i is a mass of the atom which is described by the i-th Cartesian coordinate ξ_i.

Meanwhile, the potential energy in internal coordinates can also be expanded into a Taylor series at the equilibrium point:

$$V(\mathbf{q}) = V_0 + \sum_{i=1}^{3N_a} \left(\frac{\partial V}{\partial q_i} \right)_0 q_i + \frac{1}{2} \sum_{i=1}^{3N_a} \sum_{j=1}^{3N_a} \left(\frac{\partial^2 V}{\partial q_i \partial q_j} \right)_0 q_i q_j + \ldots . \tag{2.13}$$

Here, the constant term V_0 is not important and can be set to zero, as the interpretation of vibrational spectra does not require absolute energies but energy differences between vibrational states. The linear term can be omitted as well, because all first derivatives at the minimum point are constantly zero. Moreover, the cubic and higher-order terms can also be ignored in assumption that the amplitude of

vibrations is small. Finally, the remaining quadratic term:

$$V(\mathbf{q}) \simeq \frac{1}{2}\sum_{i=1}^{3N_a}\sum_{j=1}^{3N_a}\left(\frac{\partial^2 V}{\partial q_i \partial q_j}\right)_0 q_i q_j = \frac{1}{2}\sum_{i=1}^{3N_a}\sum_{j=1}^{3N_a} f_{ij} q_i q_j \tag{2.14}$$

is positive-definite on a neighborhood of the equilibrium point due to the fact that a molecular system reaches a minimum energy in its equilibrium configuration. Accordingly, there is a mass-weighted normal coordinate basis set $\mathbf{Q} = \{Q_i\}_i$ that diagonalises the Hessian matrix $\mathbf{K} = (f_{ij})$ composed from force constants f_{ij} and the $\mathbf{G} = (g_{ij})$ matrix (see Eq. (2.12)) at the same time [36, p. 310]:

$$\mathbf{Q}^{+}\mathbf{G}\mathbf{Q} = \mathbf{1}, \tag{2.15}$$

$$\mathbf{Q}^{+}\mathbf{K}\mathbf{Q} = \mathbf{\Lambda}. \tag{2.16}$$

Here, $\mathbf{1}$ is the identity matrix and $\mathbf{\Lambda} = (\lambda_i, \ldots, \lambda_N, 0, \ldots, 0)$ is a diagonal matrix contains N non-zero diagonal elements for all vibrational modes and zero elements for translational and rotational ones. By this mean, the original complicated vibrational Schrödinger equation is decomposed into a series of N independent harmonic oscillator equations:

$$\frac{1}{2}\left(-\frac{\mathrm{d}^2}{\mathrm{d}Q_i^2} + \lambda_i Q_i^2\right)\phi_i^{v_i}(Q_i) = \epsilon_i^{v_i}\phi_i^{v_i}(Q_i), \tag{2.17}$$

$$E^{\mathbf{v}} = \sum_{i=1}^{N}\epsilon_i^{v_i}, \qquad \Psi^{\mathbf{v}}(\mathbf{Q}) = \prod_{i=1}^{N}\phi_i^{v_i}(Q_i). \tag{2.18}$$

The solution of Eq. (2.17) for the i-th normal mode and for the v_i-th vibrational state is a Hermite orthogonal function [32, p. 37]:

$$\phi^{v_i} = \frac{1}{\sqrt[4]{\pi}}\sqrt{\frac{\gamma_i}{2^{v_i}v_i!}}\mathcal{H}_{v_i}(\gamma_i Q_i)\mathrm{e}^{-\gamma_i^2 Q_i^2/2}, \tag{2.19}$$

$$\mathcal{H}_n(\zeta) = (-1)^n \mathrm{e}^{\zeta^2}\frac{\mathrm{d}^n}{\mathrm{d}\zeta^n}\mathrm{e}^{-\zeta^2}, \quad \gamma_i = \sqrt[4]{\lambda_i},$$

along with the corresponding single-mode energy (ϵ^{v_i}) and a harmonic frequency (ω_i):

$$\epsilon^{v_i} = \omega_i \left(v_i + \frac{1}{2} \right) = \sqrt{\lambda_i} \left(v_i + \frac{1}{2} \right). \tag{2.20}$$

2.4 Diagonal anharmonicity

The harmonic approximation implies that a molecular potential $V(\mathbf{Q})$ in normal coordinates has a quadratic form. However, this is not the case for real molecular systems. One reason is that the potential energy does not approach infinity when increasing the inter-atomic distance. Instead, increasing this distance leads to dissociation of the molecule into non-interacting fragments. The total potential energy of this dissociated system is a finite value which is equal to the sum of potential energies of all disconnected fragments. The value of this total energy except the equilibrium potential energy is called dissociation energy (D_e). In fact, the real dissociation energy (D_0) is lower than D_e by the difference in zero-point vibrational energies (ZPE) of the original molecule and all disconnected fragments. This is because the broken bond reduces the total number of vibrational modes and this "released" vibrational energy from the destroyed modes should also be taken into account. Figure 2.2 illustrates the difference between D_e and D_0 in case of a diatomic molecule.

Alternatively, when an inter-atomic distance becomes shorter, the repulsion energy between the nuclei and – as a result – the total potential energy of the molecule increase rapidly. Moreover, both of these energies tend to infinity at zero distance. At the same time, the harmonic potential has a finite value at any finite coordinates, including the case of zero inter-atomic distance. This means that the harmonic potential does not fit well the actual potential energy while atomic displacements from their equilibrium positions becomes large.

This deviation between the real potential and the harmonic one is caused by diagonal anharmonic effects [37] as all normal modes are still thought to be independent from each other. For diatomic molecules this type of anharmonicity can

Figure 2.2. Anharmonic (solid line) and harmonic (dash line) potentials of a diatomic molecule as a function of internuclear distance R. D_e and D_0 denote dissociation energy with and without zero-point vibrational energy (ZPE) respectively. An equilibrium internuclear distance is equal to R_e, while v is a vibrational quantum number.

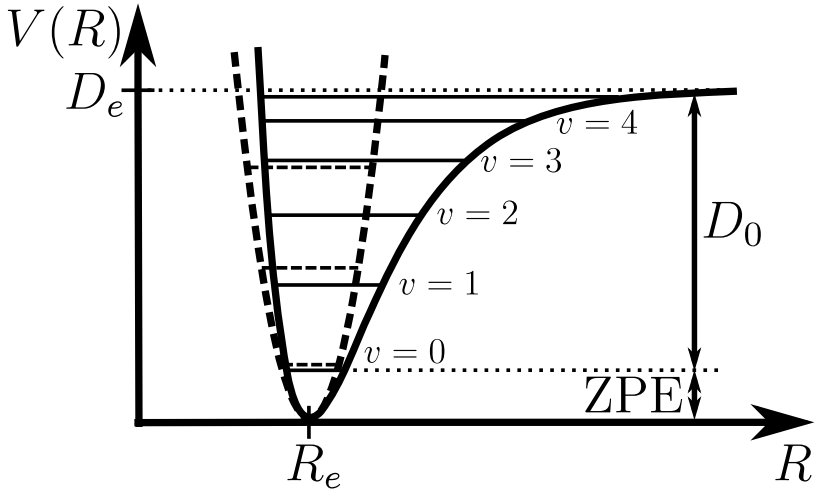

be approximately taken into account by using a potential function proposed by Morse [38] in 1929. This potential function with respect to the inter-atomic distance R has the following form:

$$V(R) = D_e \left[1 - e^{-\alpha(R-R_e)}\right]^2, \tag{2.21}$$

where D_e is a dissociation energy, R_e is the equilibrium inter-atomic distance, and α is a constant specific for each electronic state which determines the second derivative of the Morse potential function at the equilibrium point:

$$\left.\frac{\mathrm{d}^2 V(R)}{\mathrm{d}R^2}\right|_{R=R_e} = 2D_e\alpha^2. \tag{2.22}$$

The advantages of this potential is that it allows the analytical solution of the vibrational Schrödinger equation. Thus, the energy levels for any vibrational quantum number v can be computed using the following formulae:

$$E_v = \omega\left(v + \frac{1}{2}\right) - \frac{\omega^2}{4D_e}\left(v + \frac{1}{2}\right)^2, \tag{2.23}$$

where $\mu = M_1M_2/(M_1 + M_2)$ is the effective mass of the diatomic molecule, and

$\omega = \alpha\sqrt{2D_e/\mu}$ is the corresponding harmonic frequency. The last statement becomes clearer after considering the transition energy between two adjacent vibrational levels with quantum numbers v and $v+1$:

$$E_{v+1} - E_v = \omega - \frac{\omega^2}{2D_e}(v+1)\,. \tag{2.24}$$

Thus, when the dissociation energy goes to infinity as well as in case of a harmonic potential, the energy difference becomes constant and equal to ω. Alternatively, in case of a finite dissociation energy the distance between two adjacent vibrational levels decreases with v.

However, the Morse potential is not an ideal model. Sometimes it is not suitable for highly excited vibrational states [39] as it contains only two parameters. These parameters determine the shape of the Morse potential based on the behaviour of the real molecular potential near the equilibrium point and at the dissociation limit, but not in the intermediate region. Moreover, as well as the harmonic potential, it has a finite value at zero internuclear distance. Finally, it cannot be used for molecular systems with negative anharmonicity, such as methyl radical and chloromethyl radical, for which the harmonic approximation gives underestimated frequencies [40, 41].

In general, the diagonal anharmonicity can be taken into account by solving the one-dimensional vibrational Schrödinger equation:

$$\left\{-\frac{1}{2}\frac{\mathrm{d}^2}{\mathrm{d}Q^2} + V^{(1)}(Q)\right\}\phi^v = \epsilon^v\phi^v \tag{2.25}$$

with an actual one-dimensional potential curve $V^{(1)}(Q)$ computed along a mass-weighted normal coordinate Q. This equation can be solved by choosing a normalized orthogonal basis set $\zeta_i(Q)_k$ – for example using a series of harmonic functions in Eq. (2.19) – which approximates the target wave function:

$$\phi^v = \sum_k C_k\zeta_k(Q). \tag{2.26}$$

Then a Hamiltonian matrix can be constructed numerically by computing the integrals:

$$\begin{aligned} H_{ij} &= \left\langle \zeta_i(Q) \left| \hat{T} \right| \zeta_j(Q) \right\rangle + \left\langle \zeta_i(Q) \left| \hat{V} \right| \zeta_j(Q) \right\rangle \\ &= \left\langle \zeta_i(Q) \left| -\frac{1}{2}\frac{\mathrm{d}^2}{\mathrm{d}Q^2} + V^{(1)}(Q) \right| \zeta_j(Q) \right\rangle, \end{aligned} \tag{2.27}$$

After diagonalisation of this Hamiltonian matrix:

$$\mathbf{HC} = \mathbf{EC} \tag{2.28}$$

its diagonal elements **E** contains the vibrational energies while the matrix **C** determines the expansion coefficients C_k of the corresponding wave functions in terms of the chosen basis set.

An obvious drawback of this approach is the necessity to chose some basis set *a priori* that enforces to make some assumptions about the nature of vibrational states. Fortunately, a Fourier-grid-Hamiltonian (FGH) method [42, 43] provides an elegant way to overcome this difficulty. This method is based on observation that contributions to the Hamiltonian matrix ([Eq. (2.27)]) from the kinetic and potential parts have a simpler form in different basis sets. Thus, for a basis set composed from functions which associate the normal coordinate Q with independent variables $\zeta_k(Q) = N_k Q_{(k)}$ orthonormal to each other, the contribution from the potential energy operator becomes diagonal:

$$\left\langle \zeta_k(Q) \left| V^{(1)}(Q) \right| \zeta_l(Q) \right\rangle = N_k^2 V^{(1)}(Q_k)\delta_{kl}. \tag{2.29}$$

Alternatively, the contribution from the kinetic energy operator has a similar diagonal form in the basis set $\tilde{\zeta}_k(Q) = \tilde{N}_k \exp(\mathrm{i}\tilde{Q}_{(k)})$:

$$\left\langle \tilde{\zeta}_k(Q) \left| -\frac{1}{2}\frac{\mathrm{d}^2}{\mathrm{d}Q^2} \right| \tilde{\zeta}_l(Q) \right\rangle = \frac{1}{4}\tilde{N}_k^2 \tilde{Q}_{(k)}^2 \delta_{kl}, \tag{2.30}$$

which can be derived from the basis set $\{\zeta_k(Q)\}_k$ using a Fourier transformation. This

property allows to obtain an analytical expression for the elements of the Hamiltonian matrix [43]:

$$H_{ii} = \frac{\pi^2}{L^2}\frac{n^2+2}{6} + V^{(1)}(Q_i), \tag{2.31}$$

$$H_{ij} = \frac{\pi^2}{L^2}\frac{(-1)^{i-j}}{\sin^2(\pi(i-j)/n)}, \qquad i \neq j \tag{2.32}$$

when the potential $V^{(1)}(Q)$ is defined on an uniform grid $[Q_1, \ldots, Q_n]$ with length $L = Q_n - Q_1$ at the even number of points n. Again, diagonalisation of this Hamiltonian matrix gives the set of vibrational energies and the corresponding wave functions. However, in contrast with the regular approach, the matrix $\mathbf{C}$ in Eq. (2.28) contains the amplitudes of the wave functions at the grid points, rather than the expansion coefficients in some basis set.

2.5 Coupling anharmonicity

The harmonic approximation is also based on assumption that different normal modes are independent from each other. However, it is feasible only for vibrations with small amplitude when the high-order terms in the Taylor series expansion [Eq. (2.14)] of the potential energy can be ignored. As for real systems this requirement is not fulfilled, in normal mode coordinates, where the kinetic energy operator has a diagonal form, the potential energy is no longer diagonal due to the presence of these high-order terms. It couples normal modes together introducing coupling anharmonicity which is also known as off-diagonal anharmonicity [37].

The coupling anharmonicity leads to the following N-dimensional vibrational Schrödinger equation expressed in normal mode coordinates:

$$\left\{\sum_{i=1}^{N}\frac{\partial^2}{\partial Q_i^2} + V(\mathbf{Q})\right\}\Psi_{\mathbf{v}}(\mathbf{Q}) = E_{\mathbf{v}}\Psi_{\mathbf{v}}(\mathbf{Q}), \tag{2.33}$$

where the cumulative index $\mathbf{v} = \{v_1, \ldots, v_N\}$ enumerates vibrational states. This equation can be approximately solved using vibrational self-consistent field (VSCF)

method originally proposed by Bowman [22]. The method assumes that the vibrational wave function is factorizable into single-mode wave functions:

$$\Psi_{\mathbf{v}}(\mathbf{Q}) = \prod_{i=1}^{N} \phi_i^{v_i}(Q_i). \tag{2.34}$$

This reduces the original equation (2.33) into a system of N single-mode Schrödinger equations:

$$\left\{ -\frac{1}{2}\frac{\partial^2}{\partial Q_i^2} + V_{i;\mathbf{v}}^{\text{eff}}(\mathbf{Q}) \right\} \phi_i^{v_i}(Q_i) = \epsilon_i^{v_i} \phi_i^{v_i}(Q_i), \tag{2.35}$$

where each modal wave function, $\phi_i^{v_i}(Q_i)$, is coupled with the others through the effective potential [44]:

$$V_{i;\mathbf{v}}^{\text{eff}}(Q_i) = \left\langle \prod_{j\neq i}^{N} \phi_j^{v_j}(Q_j) \left| V(\mathbf{Q}) \right| \prod_{j\neq i}^{N} \phi_j^{v_j}(Q_j) \right\rangle. \tag{2.36}$$

Finally, the VSCF energy of the vibrational state $\mathbf{v}$ can be computed as the sum of modal energies $\epsilon_i^{v_i}$ corrected for the average value of the potential, which has been counted multiple times:

$$E_{\mathbf{v}}^{\text{VSCF}} = \sum_{i=1}^{N} \epsilon_i^{v_i} - (N-1) \left\langle \prod_{i}^{N} \phi_i^{v_i}(Q_i) \left| V(\mathbf{Q}) \right| \prod_{i}^{N} \phi_i^{v_i}(Q_i) \right\rangle. \tag{2.37}$$

Within the VSCF framework, the PES is usually expressed in terms of a many-mode expansion [44–47] of the potential $V(\mathbf{Q}) = V(Q_1, \ldots, Q_N)$ in the order of anharmonicity:

$$V(\mathbf{Q}) = [V(\mathbf{0})] + \sum_{i=1}^{N} V_i^{(1)}(Q_i) + \sum_{i=1}^{N}\sum_{j>i}^{N} V_{ij}^{(2)}(Q_i, Q_j) + \sum_{i=1}^{N}\sum_{j>i}^{N}\sum_{k>j}^{N} V_{ijk}^{(3)}(Q_i, Q_j, Q_k) + \ldots \tag{2.38}$$

Here, $V(\mathbf{0}) = V(0, \ldots, 0)$ is the energy of the molecular system at their equilibrium structure. This term shifts all the vibrational energies $E^{\mathbf{v}}$ in Eq. (2.33) by a constant and can be set to zero without loss of generality. The first-order term, $V_i^{(1)}(Q_i)$,

denotes a one-dimensional potential along the i-th normal coordinate:

$$V_i^{(1)}(Q_i) = V(0, \ldots, Q_i, \ldots, 0) - V(0, \ldots, 0, \ldots, 0), \tag{2.39}$$

and is responsible for diagonal anharmonicity. The second-order term, $V_{ij}^{(2)}(Q_i, Q_j)$, corresponds to a pair-coupling between modes i and j:

$$V_{ij}^{(2)}(Q_i, Q_j) = V(0, \ldots, Q_i, \ldots, Q_j, \ldots, 0) - V_i^{(1)}(Q_i) - V_j^{(1)}(Q_j), \tag{2.40}$$

while other terms refer to higher-order couplings:

$$\begin{aligned} V_{ijk}^{(3)}(Q_i, Q_j, Q_k) = {} & V(0, \ldots, Q_i, \ldots, Q_j, \ldots, Q_k, \ldots, 0) \\ & - V_{ij}^{(2)}(Q_i, Q_j) - V_{ik}^{(2)}(Q_i, Q_k) - V_{jk}^{(2)}(Q_j, Q_k). \end{aligned} \tag{2.41}$$

A special case of the expansion [Eq. (2.38)], when only diagonal (1-D) terms and second-order (2-D) terms are considered to be important, is known as a pairwise approximation [48].

The weak point of the VSCF method is that the vibrational wave function has to be known in advance in order to construct the effective potential end to solve VSCF equations (2.35). However, it is still possible to solve them iteratively. On the first iteration step, the normal modes are thought to be uncoupled by cutting the expansion [Eq. (2.38)] up to the first-order terms, $V_i^{(1)}(Q_i)$, inclusively. This eliminates the implicit dependence of the effective potential along the i-th normal mode from all other modes, that reduces the VSCF equation to the case of diagonal anharmonicity. These equations provide the first approximation for the vibrational wave function, that can be then used to construct the effective potential. This procedure is repeated until convergence, which can be determined as stability of the VSCF modal energies or the total VSCF energy.

The VSCF scheme does not provide exact energies of vibrational states as the interactions between modes are accounted implicitly. Thus, the mean-field potential

$V_{\mathbf{v}}^{\text{eff}}(\mathbf{Q})$ differs from the actual multidimensional potential $V(\mathbf{Q})$ by the value:

$$\Delta V^{\mathbf{v}}(\mathbf{Q}) = V(\mathbf{Q}) - \sum_{i=1}^{N} V_i^{(1)}(Q_i) - \sum_{i=1}^{N} V_i^{\mathbf{v};\text{eff}}(Q_i). \tag{2.42}$$

Neglecting of this difference potential introduce an error called correlation energy:

$$E_{\text{corr}}^{\mathbf{v}} = E^{\mathbf{v}} - E^{\mathbf{v};\text{VSCF}}, \tag{2.43}$$

which can be taken into accounted using a series of approach.

When this correlation energy is small, the Møller-Plesset perturbation theory can be used in order to estimate its value. This approach was described in details by Norris et al. [23] and it is known as correlation-corrected VSCF (CC-VSCF) [44] or vibrational Møller-Plesset perturbation theory (VMP) [49]. For systems with no degenerate vibrational states, at the second order of this theory the energy correction is defined as the sum of squared expectation values over the various VSCF wave functions divided by the difference of the corresponding VSCF modal energies:

$$E_{\mathbf{v}}^{\text{VMP2}} = E_{\mathbf{v}}^{\text{VSCF}} + \sum_{\mathbf{u}\neq\mathbf{v}} \frac{|\langle\Psi_{\mathbf{v}}|\Delta V_{\mathbf{v}}|\Psi_{\mathbf{v}}^{\mathbf{u}}\rangle|^2}{\sum_i^N(\epsilon_i^{v_i} - \epsilon_i^{u_i})} \tag{2.44}$$

When a molecular system contains degenerate states, this method predicts non-physically large correlation energy due to the small number in the denominator. As an alternative, various degenerate perturbation theories [24, 50] can be used for this kind of systems which treat such degenerate states in a different manner, for example, using a variational approach.

The vibrational correlation energy can also be estimated using vibrational configuration interaction (VCI) method. This method is based on approximation of an exact wave function by a linear combination of configuration state functions (CSFs):

$$\Psi(\mathbf{Q}) = \sum_{\mathbf{u}} C_{\mathbf{u}}\Psi_{\mathbf{u}}(\mathbf{Q}). \tag{2.45}$$

The Hamiltonian is then diagonalised in the basis of these CSFs by solving a secular equation:

$$\left(\mathbf{H}^{\mathrm{VCI}} - \mathbf{ES}\right)\mathbf{C} = \mathbf{0}, \tag{2.46}$$

with a symmetric Hamiltonian matrix:

$$H^{\mathrm{VCI}}_{\mathbf{vu}} = H^{\mathrm{VCI}}_{\mathbf{uv}} = \langle \Psi_{\mathbf{v}} | \mathbf{H} | \Psi_{\mathbf{u}} \rangle , \tag{2.47}$$

and a symmetric overlap matrix:

$$S_{\mathbf{vu}} = S_{\mathbf{uv}} = \langle \Psi_{\mathbf{v}} | \Psi_{\mathbf{u}} \rangle . \tag{2.48}$$

There are two main VCI schemes which differ by a construction method of the CSFs. One of them uses a basis of VSCF-optimized wave functions as a set of CSFs [51]. The advantage of this scheme is that the secular equation needs to be solved only once in order to obtain the energies of all vibrational states from the CSF space. However, these CSFs are non orthogonal to each other, that does not allow to reduce the secular equation to a single matrix diagonalisation. Moreover, the size of the CSF space is usually much larger then the number of interesting vibrational states, but for every CSF the iterative VSCF procedure has to be performed.

An alternative approach is a state-specific VCI (VSCF/VCI) [25]. Within this approach CSFs are constructed from a set of orthogonal single-mode wave functions optimized for a particular vibrational state $\mathbf{v}$:

$$\Psi^{\mathbf{u}}_{\mathbf{v}} = \prod_{i}^{N} \phi_i^{u_i;(\mathbf{v})}(Q_i). \tag{2.49}$$

The advantage of this scheme is orthogonality of CSFs, as well as its non-iterative nature. However, the secular equation needs to be solved separately for each vibrational state under the question.

The VCI method yield to exact solution when the number of CSFs approaches infinity. Nevertheless, from the computational point of view this number should be

finite and as small as possible. Within the VSCF/VCI method this can be achieved by restricting a number of single-mode wave functions which are used for generation of the CSF space up to the certain vibrational quanta $u_{\max}$. Moreover, only one-mode and two-mode excitations to the reference VSCF wave function are usually taken into account. In addition, the size of the CSF space can be reduced by including only those CSFs which have a large coefficients in decomposition [Eq. (2.45)]. Unfortunately, these coefficients are unknown beforehand and some screening technique needs to be used.

Vibrational configuration interaction with perturbation selected interactions (VCIPSI) method proposed by Scribano and Benoit [27] provides an efficient way to solve VSCF/VCI equation. Within this method, the VSCF/VCI equation is solved iteratively within a small active space of CSFs. At each iteration step the active space is then expanded by adding configurations which give sufficient contribution to the VMP2 perturbation correction. These iterations are continued until convergence of the total energy.

2.6 Fast-VSCF

A general way to construct a PES is to compute it numerically on a grid [52]. This direct evaluation increases the cost of the calculation by the time needed for construction of this PES. In fact, construction of the PES is the most limiting stage of such direct methods. Moreover, the number of coupling terms in the many-mode expansion ([Eq. (2.38)]) increases dramatically with the number of atoms in a molecular system. This makes difficult the construction of the PES even within the pairwise approximation [48] when only the pair-couplings taken into account. One way to increase the performance is to construct only those coupling terms which contribute significantly to the anharmonic effect.

There are two basic approaches. The first approach is based on assumption that a coupling term primarily affects those modes which are directly coupled through them.

Other modes may also be altered through their couplings with the affected modes. Nevertheless, this influence is usually significantly weaker as it appears indirectly.

This assumption might be used when only several vibrational modes of a large molecular system are of the main interest. Adsorbed systems are one of the important example. On the one hand, such systems usually contain hundreds of atoms, and the total number of their vibrational modes are enormously large. On the other hand, the intra-adsorbate vibrational modes and vibrations between the adsorbed molecule and its support are particularly important as they contain information about the alteration of the molecular structure and electronic properties of the adsorbed molecule upon adsorption. In this case all coupling can be split into three groups. The first group contains the most important couplings between each target mode, such as intra-adsorbate and adsorbate-support couplings. The second group contains terms that couple these target modes to other modes. The remaining couplings which do not directly affect the target modes fall into the third category. Neglecting the couplings from this third group leads to a single-to-all (STA) approach proposed by Benoit [53] who demonstrated the good accuracy of such approach along with its scalability using the example of acyclic alcohols.

Alternatively, an approach when only the couplings between a selected number of modes are taken into account is well suited for adsorbed systems. In fact, a partial Hessian technique [54, 55] which is commonly used for such adsorbed systems also implies weak vibrational couplings. In particular, this partial Hessian technique divides all atoms of the original molecular system into the active atoms which are involved into vibration and the inactive atoms which are considered to be frozen. Then only a reduced mass-weighted Hessian matrix $\bar{\mathbf{K}}$ is diagonalised which is composed from the force-constants of the active atoms only:

$$\bar{K}_{ij} = \frac{1}{\sqrt{M_i M_j}} f_{ij}. \tag{2.50}$$

This diagonalisation provides a set of active normal coordinates $\mathbf{Q}_A$. In order for this set of coordinate to be reliable, the couplings between this active vibrational mode

and the excluded ones should be small. The correctness of such assumption was tested on many systems [14, 54–57], in particular on water on a Al(111) surface [54] and 4-mercaptopyridine on a Au(111) surface [14].

The second approach is called Fast-VSCF. It is based on a hypothesis that there is a direct proportion between the intensity of a coupling term and the shift in vibrational frequencies introduced by the coupling. It follows thence that not all the couplings are equally important, therefore ignoring the weak couplings can reduce the required computational costs dramatically. Unfortunately, the intensities of the couplings are unknown beforehand, however they can be estimated using various pre-screening techniques [58]. Thus, a coupling potential $V^{(m)}_{i_1,\ldots,i_m}$ can be pre-scanned using a computationally cheap method or can be constructed on a sparse grid. Finally, the strong coupling potentials should be detected according to some measure.

There are several intensity criteria proposed in the literature. One of them is a ζ-measure which is based on the average absolute value of a coupling potential. Thus, for the m-dimensional coupling term $V^{(m)}_{i_1,\ldots,i_m}$ constructed on an $n_{i_1} \times \cdots \times n_{i_m}$ grid the measure can be computed using the following formula [59]:

$$\zeta(i_1,\ldots,i_m) = \frac{1}{n_{i_1}\cdots n_{i_m}} \sum_{i_1=1}^{n_{i_1}} \cdots \sum_{i_m=1}^{n_{i_m}} \left| V^{(m)}_{i_1,\ldots,i_m}(Q_{i_1},\ldots,Q_{i_m}) \right|. \tag{2.51}$$

A similar measure is based on a root mean square average value [58]:

$$\mu(i_1,\ldots,i_m) = \left(\frac{\sum_{i_1=1}^{n_{i_1}} \cdots \sum_{i_m=1}^{n_{i_m}} [V^{(m)}_{i_1,\ldots,i_m}(Q_{i_1},\ldots,Q_{i_m})]^2}{n_{i_1}\cdots n_{i_m}} \right)^{1/2}. \tag{2.52}$$

Alternative criteria [58] are also available, however these two ones are presumably the most frequently used, due to their simplicity.

The main problem concerning with the Fast-VSCF technique is the selection of threshold. On the one hand, it should be chosen in such a way that the number of included weak coupling terms should be minimal. On the other hand, none of the intense couplings should be filtered, even if it has reduced weight according to a pre-scanned PES. Unfortunately, it is not possible to know the optimal threshold

Figure 2.3. An artificial coupling between a bending mode and a stretching mode in rectilinear coordinates. The coordinate along the axis ξ coincides with a normal coordinate. For a large angle φ the position of the H-atom in normal coordinates is equal to $\xi^{\text{norm.}}$, while the projection of its actual position on the ξ axis is equal to ξ^{real}. The red line represents the error magnitude, and the blue line shows artificial elongation of the internuclear distance.

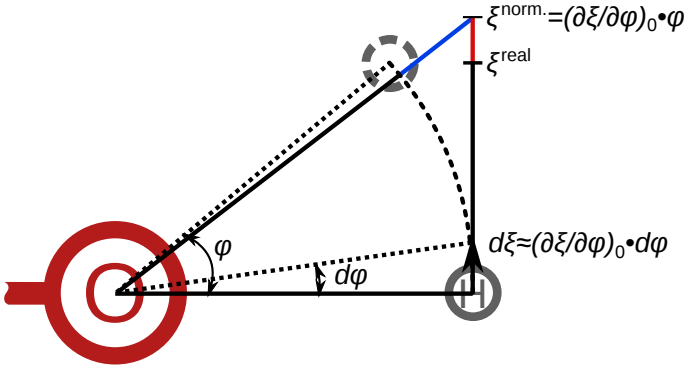

value in advance and it should be evaluated carefully for each system. Benoit [59] demonstrated using a set of test molecules, that in case of 2-D coupling terms the 20% value of threshold $\zeta_{\text{thr}} = 0.2\zeta_{\text{max}}$ should be sufficient in many cases. Alternatively, when the number of vibrational modes are large, the value of threshold can be estimated using statistical analysis [14] in assumption that coupling intensities are normally distributed. Finally, the threshold value can be selected iteratively, by computing couplings in descent order according to their intensities. These iterations continue until convergence of the VSCF energy of some reference state.

2.7 Rectilinear and curvilinear coordinates

Rectilinear normal mode coordinates Q_i introduced within the harmonic approximation is a good choice and they allow a reasonable description of many systems. However, one assumption that was used in order to obtain them was small amplitude vibrations. For high-amplitude motions, they can lead to artificial couplings.

Figure 2.3 illustrates this using the example of an O−H bending mode. In internal coordinates this mode is described by an angle ϕ, while in normal-mode coordinates it is described as displacement along a tangent line. This tangent line coincides with the circular motion at the initial stage and introduces only small deviation when the

amplitude is small. However, in case of large amplitude the deviation is significant. In reality the atom moves in a circular orbit preserving the inter-atomic distance, but in rectilinear coordinates the atom moves along a straight line stretching the bond. This introduces an artificial coupling between this O−H bending mode and the O−H stretching mode. Moreover, when the number of such bending and stretching modes is greater than two, all of them become coupled simultaneously, which leads to the necessity to take into account these high-order coupling terms as well. However, internal valence coordinates could potentially reduce the number of this artificial coupling terms and leads to faster convergence of the N-body expansion of the PES.

Curvilinear coordinates are also important for description of internal rotation where one part of a molecule turns about an axis while the other part remains fixed. A well known example of such type of motion is internal rotation of hydroxyl group in methanol. Unfortunately, this type of motion is very difficult to describe using rectilinear coordinates as the motion along the corresponding normal-mode coordinate leads to "dissociation" of the hydroxyl group into constituent atoms. As it was demonstrated by Scribano et al. [60] the rectilinear coordinate representation doubles the frequency of this mode, while in curvilinear coordinates the obtained frequency is very close to the experimental value.

Unfortunately, using a different set of coordinates ($\mathbf{q}$) instead of normal-mode coordinates leads to a non-diagonal complex form of the kinetic energy operator [60, 61]:

$$\hat{T}_n(\mathbf{q}) = -\frac{1}{2}\sum_{i,j}\rho(\mathbf{q})^{-1}\frac{\partial}{\partial q_i}\rho(\mathbf{q})G^{-1}_{ij}(\mathbf{q})\frac{\partial}{\partial q_j}, \tag{2.53}$$

where G is the metric tensor, and $\rho(\mathbf{q})$ is a weight function which converts volume elements between the curvilinear ($\mathbf{q}$) and rectilinear ($\mathbf{Q}$) coordinates:

$$\mathrm{d}Q_1 \cdots \mathrm{d}Q_N = \rho(\mathbf{q})\,\mathrm{d}q_1 \cdots \mathrm{d}q_N. \tag{2.54}$$

Moreover, all components of this metric tensor are dependent on curvilinear coordinates, what makes their evaluation very challenging. For this reason some assumption is required. Thus, if all components of the inverted metric tensor are constant, the

kinetic energy operator becomes simpler [60]:

$$\hat{T}_n(\mathbf{q}) = \sum_{i,j} G^{-1}_{ij,0} \frac{\partial}{\partial q_i} \frac{\partial}{\partial q_j}. \tag{2.55}$$

Despite of the fact that this simplification does not eliminate coupling anharmonicity completely. most of the artificial coupling terms can now be avoided, that dramatically increases the accuracy of the computed anharmonic frequencies.

Chapter 3

Electronic structure methods and fragment methods

3.1 Wave function based methods

There are two types of methods for solving the electronic Schrödinger equation 2.4. The first type of methods is based on a wave function formalism where the electronic wave function depending on $3N_e$ spatial coordinates and N_e spin variables is sought. As a first approximation, all electrons are thought as independent and interacting with each other through mean-field potential. This method is called self-consistent field (SCF) [29, p. 86] or Hartree-Fock (HF) method and it is analogous to VSCF which was described in section 2.5. However, in contrast with latter method, the electronic wave function is sought as an antisymmetrised product of one-electron wave functions which form one Slater determinant Φ_0 rather than a direct product.

This approach does not account for explicit electronic motion (electronic correlation) which can be estimated using different methods. Thus, the energy can be estimated using the configuration interaction (CI) method [29, p. 137], where an exact electronic wave function Ψ is approximated by a linear combination of Slater determinants of the ground and excited electronic states.

$$\Psi = \sum_{i=0} C_i \Phi_i \tag{3.1}$$

The maximal excitation level is usually limited up to a certain order that gives a particular CI methods. The simplest CI methods are are CI with double excitations (CID) and CI with single and double excitations (CISD). State energies are then obtained by diagonalisation of the Hamiltonian matrix in the basis of these determinants. Alternatively, when the correlation energy is small it can also be estimated using Møller-Plesset perturbation theory [62]. Within this method, the wave function is expanded into a power series of λ and the state energy is computed as a sum of corrections to energy.

Electronic correlation can also be taken into account using coupled-cluster (CC) method [63]. Similarly to the CI approach, CC method approximates an exact electronic wave function by combination of Slater determinants. However, these determinants are constructed in a consistent fashion using an excitation cluster operator:

$$\Psi = \exp(\hat{T})\Psi_0. \tag{3.2}$$

The cluster operator can be expanded into a series according to the excitation order:

$$\hat{T} = \hat{T}_1 + \hat{T}_2 + \hat{T}_3 + \dots. \tag{3.3}$$

Applying the operator $\hat{T}_1$ to a wave function gives all single-excited wave functions with respect to the reference one, while the $\hat{T}_2$ operators gives all double-excited ones, and so on.

Truncation of the series (3.3) defines a particular CC method. In particular, keeping only the second term in Eq. (3.3) gives coupled-cluster doubles (CCD) method. In this method the wave function is expressed as:

$$\Psi^{\mathrm{CCD}} = \exp(\hat{T}_2)\Psi_0 = \left(1 + \hat{T}_2 + \frac{\hat{T}_2^2}{2} + \frac{\hat{T}_2^3}{6} + \dots\right)\Psi_0. \tag{3.4}$$

However, in contrast with the CID method where the wave function approximated using the ground and the doubly excited configurations only, the CCD wave function also contains excitation of the highest order. Moreover, the weights of such high-order

excitations in Ψ^{CCD} are not independent from each other, but sought as a product of the corresponding second-order coefficients:

$$\Psi^{\mathrm{CCD}} = \Psi_0 + \sum_{i,a} \sum_{j>i,b>a} C_{ij}^{ab} \Psi_{ij}^{ab} + \sum_{i,a} \sum_{j>i,b>a} \sum_{k>l,c>b} \sum_{l>m,d>c} C_{ij}^{ab} C_{kl}^{cd} \Psi_{ijkl}^{abcd} + \ldots, \quad (3.5)$$

that makes them coupled.

The other frequently used CC methods are CC with single and double excitations (CCSD) [64], and CC with single, double, and triple excitations (CCSDT) [65]. Despite of the importance of triple excitations, taking them into account is very time consuming and it is usually tractable only for relatively small molecules. Instead, they are usually taken into account approximately using a perturbation theory that leads to the CC singles, doubles and perturbative triples (CCSD(T)) method [66].

3.2 Density functional theory

Computational demands of wave function based methods grow rapidly with the number of electrons, which makes them impracticable for large molecular systems, such as biomolecules or adsorbed systems. For such systems density functional theory (DFT) [29, p. 232] becomes an attractive alternative as it describes them in terms of electron density $\rho(\mathbf{r})$ rather than wave function. The electron density depends only on three spatial coordinates and uniquely defines the properties of the system. The electron density that minimizes an energy functional $E[\rho]$ is a true density of the system.

The energy functional consists of three parts: the kinetic energy of electrons $T[\rho]$, the energy of electrons in a nuclear potential $V_{en}[\rho]$, and an interaction energy between electrons $V_{ee}[\rho]$:

$$E[\rho] = T[\rho] + V_{en}[\rho] + V_{ee}[\rho]. \quad (3.6)$$

Here, $V_{en}[\rho]$ corresponds to the Coulomb interaction between nuclei and electrons and can be expressed as an explicit functional of the density:

$$V_{en}[\rho] = -\int \sum_{\alpha=1}^{N_a} \frac{Z_\alpha}{|\mathbf{R}_\alpha - \mathbf{r}|} \rho(\mathbf{r}) \mathrm{d}\mathbf{r}, \tag{3.7}$$

where Z_α and $\mathbf{R}_\alpha$ are the charge and the position of the α-th nucleus, respectively. It is assumed that all characteristic properties of the molecular system, which distinguish it from other systems, are solely determined by $V_{en}[\rho]$. It is also assumed that the remained terms from the energy functional:

$$F[\rho] = T[\rho] + V_{ee}[\rho], \tag{3.8}$$

form an universal functional which is independent from the particular molecular system [67].

In case of non-interacting electrons (for example, when all electrons are infinitely distant), the energy functional contains only the kinetic part:

$$T_s[\rho] = -\frac{1}{2} \sum_{i=1}^{N_e} \left\langle \phi_i(\mathbf{r}) \left| \nabla_i^2 \right| \phi_i(\mathbf{r}) \right\rangle. \tag{3.9}$$

Here, $\phi_i(\mathbf{r})$ are a set of one-electron orbitals which are related to the electron density ρ as:

$$\rho = \sum_{i=1}^{N_e} |\phi_i(\mathbf{r})|^2. \tag{3.10}$$

Moreover, since $F[\rho]$ is a universal functional of the density regardless of the distance between electrons, $T_s[\rho]$ is also a universal functional.

Finally, the interaction energy between electrons $V_{ee}[\rho]$ among others includes an electron-electron repulsion energy $J[\rho]$:

$$J[\rho] = \frac{1}{2} \int \int \frac{\rho(\mathbf{r})\rho(\mathbf{r}')}{|\mathbf{r} - \mathbf{r}'|} \mathrm{d}\mathbf{r}' \mathrm{d}\mathbf{r}, \tag{3.11}$$

which is also a universal functional of ρ. The residual term is called an exchange-correlation (XC) functional $E_{\mathrm{xc}}[\rho]$:

$$V_{ee}[\rho] = J[\rho] + E_{\mathrm{xc}}[\rho], \tag{3.12}$$

with an unknown form. Once $E_{\mathrm{xc}}[\rho]$ is determined, the energy functional $E[\rho]$ can be minimized by solving a Kohn-Sham equation, which is in fact a set of one-electron Schrödinger equations with a Kohn-Sham effective potential v_{s}:

$$\left(-\frac{1}{2}\nabla_i + v_{\mathrm{s}}\right)\phi(\mathbf{r}) = \epsilon_i\phi(\mathbf{r}). \tag{3.13}$$

This effective potential consists of an external potential v_{en} which is responsible for interactions between nuclei and electrons:

$$v_{en}(\mathbf{r}) = \sum_{\alpha=1}^{N_a} \frac{Z_\alpha}{|\mathbf{R}_\alpha - \mathbf{r}|}, \tag{3.14}$$

as well as from a Hartree potential:

$$v_{\mathrm{H}}(\mathbf{r}) = \int \frac{\rho(\mathbf{r}')}{|\mathbf{r} - \mathbf{r}'|}\mathrm{d}\mathbf{r}', \tag{3.15}$$

and an exchange correlation potential:

$$v_{\mathrm{XC}}(\mathbf{r}) = \frac{\delta E[\rho]}{\delta\rho(\mathbf{r})}. \tag{3.16}$$

This XC-functional can be formally split into an exchange functional $E_{\mathrm{X}}[\rho]$, which is caused by indistinguishability of electrons, and a correlation functional $E_{\mathrm{C}}[\rho]$, which describes simultaneous movement of electrons:

$$E_{\mathrm{XC}}[\rho] = E_{\mathrm{X}}[\rho] + E_{\mathrm{C}}[\rho]. \tag{3.17}$$

Because the universal XC-functional is unknown, a large number of approximate functionals have been proposed. Among them are Perdew-Burke-Ernzerhof (PBE) [68]

and Becke88 three-parameters Lee-Yang-Parr (B3LYP) [69] functionals which are used in this work. The PBE functional is classified as a generalised gradient approximation (GGA) functional as it explicitly depends on the density ρ and on the density gradient:

$$E_{\mathrm{XC}}^{\mathrm{PBE}}[\rho] = \int \rho(\mathbf{r}) \epsilon_{\mathrm{XC}}^{\mathrm{PBE}}(\rho, \nabla\rho) \mathrm{d}\mathbf{r}. \tag{3.18}$$

In particular, this functional approaches to the uniform electron gas limit for slowly varying density and for this reason it describes metal surfaces at a reasonable level. At the same time, it is less accurate for molecular systems with small number of electrons, due to the fact that it does not compensate in full non-physical repulsion of electrons from themselves [70] caused by the DFT formalism. The B3LYP functional also depends on ρ and $\nabla\rho$, but in addition it tries to compensate the self-interaction problem by using Hartree-Fock (HF) exact exchange. For this reason, B3LYP functional becomes very attractive for small molecules but it is less accurate for surfaces as it is no longer approaches the uniform electron gas limit.

3.3 Fragment methods

In fragment methods a complex system is divided into fragments and then the total energy of the system is approximated using the energies of these fragments. There are two main approaches to express a total energy in terms of fragment energies. Within an additive scheme, a target system is split into several non-overlapping fragments. Thus, a large enzyme molecule can be divided into an active site, which determines its catalytic properties, and surrounding atoms which are responsible for steric properties of the protein. All fragments are then simulated independently using different methods, for example using a quantum mechanical (QM) methods for atoms from the active site and molecular mechanics (MM) for the other atoms. The total energy is usually defined as a sum of fragment energies, each of them computed at their respective level of theory. This obviously leads to loss in connectivity between the fragments and requires an additional treatment of the boundary region. Thus, for a two fragment system A − B, the total energy within additive schemes is expressed

as:

$$E(\mathrm{A}-\mathrm{B}) = E_{\mathrm{I}}(\mathrm{A}) + E_{\mathrm{II}}(\mathrm{B}) + E_{\mathrm{III}}(\mathrm{A},\mathrm{B}), \tag{3.19}$$

where $E_{\mathrm{I}}(\mathrm{A})$ and $E_{\mathrm{II}}(\mathrm{B})$ are energies of the fragments A and B computed at levels I and II respectively, and $E_{\mathrm{III}}(\mathrm{A},\mathrm{B})$ is the energy correction due to the connectivity of the original molecular system. This additive scheme is dominantly used in various QM/MM approaches, for example in ones proposed by Bakowies and Thiel [71] or by Field et al. [72]

Alternatively, within a subtractive scheme the most important part of the molecular system is carved out and this model system is simulated using an accurate "high-level" method, while the entire system is described using a "low-level" method with a less computationally demanding technique. The accurate total energy of the real system is then approximated as its low-level energy corrected by the energy differences for each model system computed at high and low levels:

$$E(\mathrm{A}-\mathrm{B}) = E_{\mathrm{low}}(\mathrm{A}-\mathrm{B}) - E_{\mathrm{low}}(\mathrm{A}) + E_{\mathrm{high}}(\mathrm{A}). \tag{3.20}$$

Important examples of such methods are IMOMM (Integrated Molecular Orbital + Molecular Mechanics) [73], ONIOM (Our own N-layered Integrated molecular Orbital and molecular Mechanics) [74], and QMPot (a combined quantum mechanics inter-atomic potential function) [75].

The main challenge of additive schemes is to chose a reliable model that represents the interaction between detached fragments. Thus, Field et al. [72] proposed a special interaction Hamiltonian which reduces the actual complex interaction within an original molecular system to van der Waals interaction between nuclei belonging to different fragments, as well as to electrostatic interaction of nuclei and electrons from one fragment with a series of point charges representing other fragments. Alternatively, this interaction can be approximated using a special electrostatic potential which can be constructed in many different ways, for example, using empirical [76] or semi-empirical [77] approaches. In contrast, fragment methods based on subtractive model do not require any additional Hamiltonian as interaction between various

parts are already taken into account by describing the whole system at low level of theory. However, the problem still persists when the fragmentation leads to cutting covalent bonds.

There are two main strategies to treat broken bonds. The most frequently used approach – and probably the earliest one – is to saturate these bonds ($A-B$) by link atoms (L). Thus, within additive schemes these fictitious atoms are usually added on either side of a broken bond [72, 78]. Subtractive schemes preserve integrity of the original molecular system, and for this reason within these schemes link atoms are added only to the detached model system [73]. These link atoms are usually hydrogens, but different atoms such as halogens are also popular. Sometimes parametrised atoms which imitate particular groups of atoms [79] or even model potentials [80] are used.

When a fragment method is used for the optimization of a large molecular system, link atoms introduce additional degrees of freedom. However, it is possible to eliminate them by imposing certain restrictions upon their possible position. Thus, because the bond between atoms A and L mimics the original $A-B$ bond, a reasonable constraint could be to place the link atom L on the line along the $A-B$ bond and enforce it to stay on this line. Within the IMOMM method, the enforcement is achieved by freezing all three atoms (A, B and L) during the geometry optimisation. An alternative approach is implemented within QMPot framework where the $A-L$ distance is kept fixed, but the $A-B$ distance is adjusted during the optimization in order to minimize a force acting on the link atom [81]. In contrast to all of the mentioned schemes, the ONIOM approach allows the A-L bond length to vary in direct proportion to the real bond.

The second strategy to deal with broken bonds is to use localized bond orbitals [82, 83]. This set of approaches assumes similarity of molecular orbitals representing a bond between two atoms in similar molecules. For this reason, the broken bond in a large molecular system can be described using precomputed orbitals of a small molecule. Ref. [84] showed that neither frozen orbitals strategy nor link atoms strategy gives accurate results for all systems. Nevertheless, this localized bond

orbital approach is non-adaptable for molecules adsorbed on metal surfaces, due to the delocalized character of the electron density of metallic surfaces.

3.4 Fragment method for improvement of anharmonic adsorbate frequencies[1]

Despite of the long history of fragment methods, they are rarely used to study adsorption on metallic surfaces. The reason being that fragment methods were designed for acceleration purposes and additional acceleration is usually not required for adsorbed systems. Thus, periodic DFT already provides reasonable speed as a surface is described using a unit cell with a small number of atoms. Moreover, the electron density in metals is uniformly distributed and thus XC-functionals that fulfil homogeneous electron gas limit, such as PBE, are known to give very reliable results in this case.

However, such functionals are liable to self-interaction error [85]. This error is caused by the possibility of an electron to interact with itself and leads to over-delocalization of the electrons which introduces an error when applied to isolated molecules. This error can be partially neglected by using hybrid XC-functionals (for example, Heyd-Scuseria-Ernzerhof (HSE) functional [86]) at the cost of efficiency, as computing the HF exchange for metallic systems is time consuming. However, an accurate description of the adsorbed molecule is especially important as the most interesting aspects of adsorbed systems is related to the change in molecular properties and behaviour of the adsorbed species during the adsorption process.

An alternative solution is to use a fragment method where each part of the adsorbed system (metallic surface and adsorbed molecule) is simulated at the appropriate level of theory. Our fragment method [87] is based on a subtractive scheme, and it does not require a special treatment of the region between adsorbate and metallic support. Within this approach the metallic surface and the adsorbed molecule

[1] Reprinted in part with permission from **S. K. Chulkov** and D. M. Benoit, "A fragment method for systematic improvement of anharmonic adsorbate vibrational frequencies: Acetylene on Cu(001)", *J. Chem. Phys.*, **139**, 214704 (2013). Copyright 2013, AIP Publishing LLC.

is described using periodic DFT (method I). In addition, the total energy of the adsorbed molecule is computed using gas phase *ab initio* method, for example using the CCSD(T) method (method II). Finally, the energy of the isolated adsorbed molecule is computed using periodic DFT (method I) to obtain a hybrid correction to the total energy of the system.

The total energy at the hybrid level (I|II) is computed using a subtractive scheme as:

$$E(\mathrm{I|II}) = E(\mathrm{I}) - E_a(\mathrm{I}) + E_a(\mathrm{II}), \tag{3.21}$$

where $E(\mathrm{I})$ is the total energy for the whole system at level I, while $E_a(\mathrm{I})$ and $E_a(\mathrm{II})$ denote the energies of adsorbed part at levels I and II respectively. This implies that in order to compute the energy at hybrid level three calculations are needed for each single point on the PES.

As our fragment method is based on a subtractive scheme, an "extracted" adsorbed molecule remains connected with the surface through the $E(\mathrm{I})$ term in Eq. (3.21). For this reason, for a weak adsorption, additional treatments are not required. However, for a moderate chemisorption, the geometry of adsorbate molecule is usually significantly altered. Often such molecule, being detached from the surface, has a multi-reference wave function that requires the use of a multi-reference approach at level II. Unfortunately, in order to be able to compute $E_a(\mathrm{I})$ term in Eq. (3.21) a multi-reference approach has to be used for the periodic model system, that can cause issues with standard DFT approaches.

In order to avoid this difficulty, extra link atoms L can be added in the line between the atom from the adsorbed molecule A and the metallic surface B. The exact position of the link atoms is similar to the ONIOM [74] method and determined by:

$$\vec{\mathbf{r}}_{\mathrm{L}} = \vec{\mathbf{r}}_{\mathrm{A}} + g(\vec{\mathbf{r}}_{\mathrm{B}} - \vec{\mathbf{r}}_{\mathrm{A}}), \tag{3.22}$$

where g is a constant scaling factor and $\vec{\mathbf{r}}_{\mathrm{L}}$, $\vec{\mathbf{r}}_{\mathrm{A}}$, $\vec{\mathbf{r}}_{\mathrm{B}}$ are Cartesian coordinates of the link atom, and the atoms A and B respectively. However in contrast to the ONIOM scheme where the g factor is defined as ratio between "standard" bond lengths, which

are in fact empirical parameters, in the current implementation this ratio is computed based on equilibrium distances obtained using methods I and II:

$$g = \frac{|\vec{\mathbf{r}}_{\mathrm{A}} - \vec{\mathbf{r}}_{\mathrm{L}}|_{\mathrm{II}}}{|\vec{\mathbf{r}}_{\mathrm{A}} - \vec{\mathbf{r}}_{\mathrm{B}}|_{\mathrm{I}}}. \tag{3.23}$$

This approach allows to avoid needless empiricism, and to estimate this scaling factor for a different systems in a consistent fashion.

In the current implementation, the method is based on assumption that the periodic DFT describes the equilibrium structure of the adsorbed system reasonably well. For this reason this fragment method is used for computing of anharmonic PES only, while geometry optimization and the calculation of a Hessian matrix are solely performed at level I. Fortunately, this assumption is usually fulfilled that is supported by two test cases: acetylene on Cu(100) surface (see Chapter 5) and on thiophene on Au(111) surface (see Chapter 6).

Chapter 4

Local implementation

For the purposes of this work, the vibrational Schrödinger equation (2.33) is solved using a PVSCF computer code [88]. This vibrational Schrödinger equation, of course, can be solved using widely available quantum mechanical (QM) program packages, such as GAMESS-US [89] or MOLPRO [90]. However, there are some disadvantages connected with this approach.

1. Using a vibrational self-consistent field (VSCF) solver from one of the mentioned QM packages forces us to use a potential energy surface (PES) constructed with one of the QM method available in the particular program. Thus, MOLPRO stores a precomputed PES in a binary restart file with proprietary format and for this reason using the PES constructed outside of MOLPRO is close to impossible. In contrast with MOLPRO, GAMESS-US stores the PES in a text file with an apparent format. However, it is still very difficult to locate a point on a PES having only its internal index stored in the GAMESS restart file.

2. The maximal order of mode coupling terms in the many-mode expansion of the PES (2.38) in the majority of QM packages is often limited up to the 2nd, 3rd or sometimes up to the 4th order. The reason being that the contribution to the transition frequencies from the coupling terms decreases with increasing of their order, and therefore the highest terms are rarely needed. Moreover, construction of these highest order coupling terms are very time consuming and it may be impractical. However, in the future with advances in computer hardware

the highest terms may become tractable and the general m-dimensional (m-D) implementation of VSCF based methods may be required.

3. Some available VSCF solvers (e.g. in GAMESS-US) need all coupling terms in the many-mode expansion up to the certain order which depends on chosen accuracy level. However, not all of them are important and actually need to be taken into account. Fast-VSCF based methods can reduce the computational costs up to few order of magnitudes [91]. Moreover, the acceleration becomes more significant for high-order coupling terms.

The current implementation of the PVSCF code focuses on a balance between an accuracy and a time consumption. It uses a PES defined on a grid (both regular and non-regular grid are allowed), and makes no assumptions about the actual functional form of the PES. For each tabulated point on the grid PVSCF generates an input file based on a template provided by user. When all single-point energy (SPE) calculations are done, the potential file with an intuitive and well described format should be created by user which is used within VSCF-based approaches. This architecture makes the program compatible with any existing QM packages, that is in fact a big advantage of PVSCF.

Another key feature of the PVSCF code is a fast and accurate solver of 1-D vibrational Schrödinger equation described in details in Ref. [88]. This solver is based on the Fourier-grid-Hamiltonian (FGH) method [42] discussed in Section 2.4 and inherits all of the advantages of this approach. Thus, it can naturally deal with aperiodic and periodic potentials that can be useful for adsorbed systems.

My contribution to this code was to implement a general efficient solver for VSCF and VSCF/VCI methods which can deal with a coupling potential of an arbitrary dimensionality. In order to do this, a set of interrelated problems were sorted out. Thus, the number of tabulated points on a PES, where an energy should be evaluated, significantly increases with the order of coupling terms. The amount of time required to construct these coupling terms, however, is mainly dependent on the performance of the implementation of a particular *ab initio* electronic structure

method. The separate VSCF code gives an opportunity to chose the most efficient implementation of the particular *ab initio* method. Whereas there is no other way to speed up a single SPE calculation, an additional acceleration may be achieved by distributing these SPE tasks over a number of computational nodes. Then, the constructed high-dimensional coupling potentials should be interpolated using a general m-dimensional (m-D) interpolation technique. Finally, the constructed high order coupling terms should be used within VSCF and VSCF/VCI frameworks, so an effective parallel m-D implementation needs to be developed.

4.1 GridDatabase interface[1]

The computational bottleneck of direct VSCF-based methods is the generation of an accurate PES. Thus, for typical systems the number of single point energies (SPE) that have to be computed usually lies between 10^3 and 10^6. This upper boundary can be easily reached even within the pairwise approximation [48] for systems with more than 35 active atoms. Moreover, at the same time computational efforts which are required even for one SPE calculation increase drastically with the number of atoms in a molecular system. A similar problem may occur during construction of the Hessian matrix. Thus, if an analytical gradient is not available for the chosen *ab initio* level of theory, the number of displacements grows as the square of the number of active atoms and reaches a million SPEs for a system with 236 active atoms. In both cases, the amount of processing time (wall time) can be reduced through parallel computing, the obvious technique being to distribute serial tasks across available computing cores. This method can be easily implemented and yields directly to a linear scaling approach (in terms of the number of points). Nevertheless, in order to use computational resources efficiently, some important questions need to be considered.

[1]Reprinted in part with permission from D. M. Benoit, B. Madebene, I. Ulusoy, L. Mancera, Y. Scribano, and **S. Chulkov**, "Towards a scalable and accurate quantum approach for describing vibrations of molecule–metal interfaces", *Beilstein J. Nanotechnol.*, **2**, 427–447 (2011). Copyright 2011, Beilstein Institut.

First, some queueing systems on grid resources distribute jobs on each node, not to each core, such that several serial jobs need to be started on each node simultaneously, in order to optimise computational power use. Unfortunately, the different jobs, which run on the same node, may take different computational time. This situation happens very often, because during the PES generation the displacements far from the equilibrium position usually require a longer iteration cycle in order to achieve convergence. It is also very difficult to predict how many nodes and cores may be expected, due to different priority policies for each computer grid. Thus, we need a balancing mechanism which allows us to utilise all cores on all available nodes evenly. The solution involves implementing a distribution system that submits points dynamically to every single node. Instead of submitting a batch script, a special universal executable script (UES) is submitted. This script connects to a SQL database, downloads the first unprocessed grid point, related files and an appropriate external executable script (EES), and runs the EES on the particular node and core. This additional EES provides a way to extend functionality dynamically. For example, a switching between several alternative PES which are computed using different quantum packages can be performed on a regular basis without necessity of releasing an occupied computational node and resubmit the UES. As jobs should have an ability to run on different clusters, grids and individual nodes with different kinds of processors and under various operating systems, all scripts have to be cross-platform.

The distribution system was implemented using the Perl programming language, as it has pure MySQL and PostgreSQL database interfaces which do not use dynamic libraries written in other languages. This is a critical point given that usually MySQL/PostgreSQL client programs and libraries are not installed on the computational nodes. Moreover, almost all Perl interpreters provide a command line option to specify the location of non-standard modules, which makes the installation procedure simple and flexible.

Second, due to the unreliable nature of distributed computing across various locations, some results can go missing for various reasons. In order to avoid missing points, an intelligent system is needed to recognise and react to various failures, such

as when a node goes down, job killed by queueing system or abnormally terminated due to convergence problems, network or SQL server troubles, and so on. Such a system was implemented in two stages. After the calculation of a grid point, the EES parses the output file and looks for results. It then sends the results to the UES and returns an exit code. Depending on this code, the results will be uploaded back to the database, or the current point or even all points within a project may be marked as erroneous and will be no longer considered. In the meantime, if there are no results during a specified period of time, it is assumed that something went wrong and the point will be resubmitted.

Third, due to various security policies, there are some grid locations where outgoing direct connections to the SQL server are not allowed. In order to use these computational nodes as well, a special script was developed. This script exports a specified number of grid points along with dependent files from the database and generates a regular batch script that can be submitted manually on these non-standard locations. The calculated results can then be uploaded to the database using a separate Perl script which scans log files and processes the exported grid points exactly as if they were distributed in an automatic fashion. Moreover, this export feature does not conflict with the automatic distribution mode, because the exported points are marked appropriately and no longer considered as available.

In summary, the grid-based PES construction process is composed of the following steps (Figure 4.1):

1. Generate the set of grid points and upload them to the database. Upload an EES designed specifically to perform a particular single point calculation along with dependent files, such as templates, external basis sets, restart files, etc.

2. Submit batch scripts using PBS, SGI, xgrid or any other batch system, which will start one UES for each CPU, and/or start the UES manually on the local workstation.

3. After the UES is started, it downloads the EES and correspondent files once for each grid location. Then it downloads the first available grid point, runs the EES

Figure 4.1. Diagrammatic representation of the GridDatabase interface.

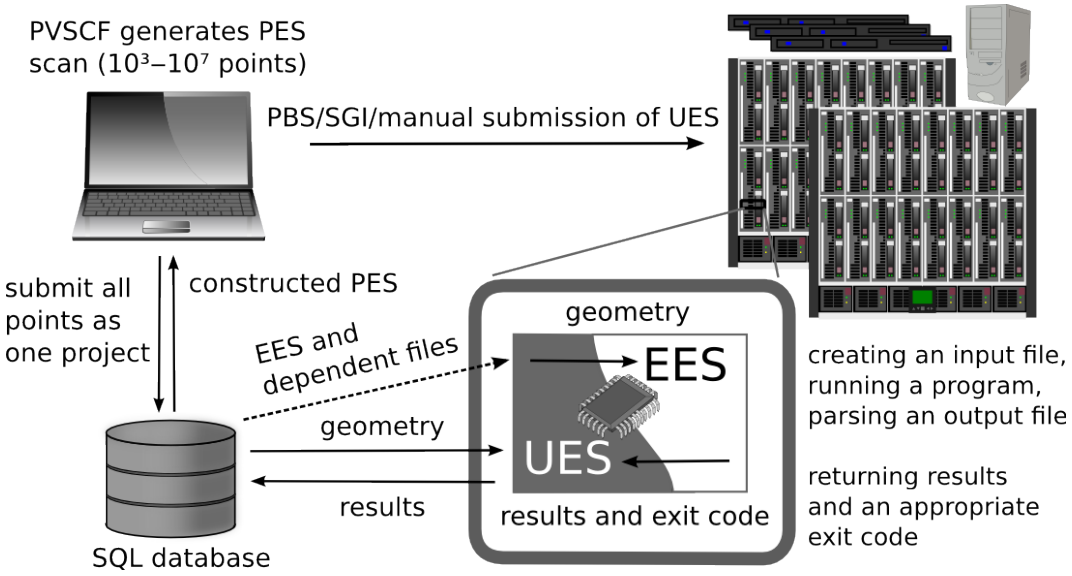

and sends the geometry of the system at the selected grid point to the EES. At the meantime, the EES produces a valid input file from a downloaded template file and provided geometry, runs the particular *ab initio* program, and, when it finished, parses the results and sends them back to the UES along with an appropriate exit code After termination of the EES, the UES returns results to the database or marks the grid point as defective, and tries to download the geometry of the next grid point. This step is repeated until no more points available.

4. If the UES is unable to establish an outgoing Internet connection to the SQL database, for example due to a strict firewall policy, an alternative batch script which runs a bundle of SPE jobs can be automatically generated and then submitted manually to a particular grid location. After termination of this batch script the obtained results can then be uploaded back to the database in a consistent fashion.

5. Retrieve constructed PES and the list of non-converged points from the database.

4.2 Interpolation

The automated distribution system described in the previous section dramatically accelerates the performance of the PES generation process. However, because PVSCF

uses grid-based representation of the PES, a numerical integration algorithm needs to be used in order to solve 1-D vibration Schrödinger equations. According to the previous experience [88], the optimal number of grid points required for an accurate numerical integration lies between 32 and 128 along each vibrational coordinate. However, from the computational perspective it is impractical to compute the energy at all of these grid points using an *ab initio* electronic structure method. Instead, the PES can be constructed on a sparse grid where, for example, only 16 SPEs along each coordinate are accurately computed. The energies at other grid points can be approximated using various interpolation techniques.

This section discusses three interpolation methods implemented in PVSCF, such as a cubic spline interpolation, a bicubic interpolation, and a Shepard interpolation. The first two methods have their own application area while the Shepard interpolation can be used for surfaces with any dimensionality. The reliability of these three methods is then tested with model systems against each other and against available analytical vibrational frequencies.

4.2.1 Cubic spline interpolation

One of the interpolation technique that is commonly used and implemented in PVSCF code for 1-D potential curves along a single normal mode is a cubic spline interpolation [92, p. 120]. Within this technique an energy at any arbitrary point x which lies between two reference points x_{i-1} and x_i is calculated as the value of a piecewise cubic polynomial:

$$f_i(x) = A_i(x - x_i)^3 + B_i(x - x_i)^2 + C_i(x - x_i) + E_i, \tag{4.1}$$

where A_i, B_i and C_i are polynomial coefficients and E_i is a tabulated energy value computed at the grid point x_i. With an assumption that all of these polynomials as well as their first and second derivatives are continuous their coefficients can be

determined using the following relations:

$$h_{i+1}B_{i+1} + 2\left(h_{i+1} + h_i\right)B_i + h_iB_{i-1} = 3\left(\frac{E_{i+1} - E_i}{h_{i+1}} - \frac{E_i - E_{i-1}}{h_i}\right), \quad (4.2)$$

$$A_i = \frac{(B_i - B_{i-1})}{3h_i}, \qquad C_i = h_iB_i - h_i^2A_i + \frac{E_i - E_{i-1}}{h_i}, \qquad h_i = x_i - x_{i-1}.$$

The equation (4.2) makes a connection between the second derivatives of the cubic spline at three adjacent tabulated points. However, the number of such equations are two less than the total number of grid points n. For this reason two boundary conditions at the first (x_0) and the last (x_{n-1}) tabulated grid points need to be defined. The following two boundary conditions are implemented in PVSCF.

1. An assumption that the second derivatives at the first and the last grid points are both equal zero ($B_0 = B_{n-1} = 0$) gives *natural cubic splines*. These splines were dominantly used for the interpolation of 1-D potential curves. Moreover, originally PVSCF uses linear extrapolation to estimate the validity of a PES range. In fact, it is equivalent to the natural cubic spline extrapolation as the natural cubic spline becomes linear outside the interpolation interval $[x_0 \dots x_{n-1}]$.

2. The required PES range often can be estimated more accurately using splines which preserve their behaviour on the boundary subintervals outside of the interpolation interval. For example, if the potential curve has a quadratic shape on a subinterval $[x_0 \dots x_1]$, it probably remains quadratic from the left of x_0. This behaviour can be achieved by fixing the values of second derivatives at the first and the last grid points equal to those at the nearest neighbour grid points ($B_0 = B_1, B_{n-1} = B_{n-2}$).

4.2.2 Bicubic interpolation

In contrast with the cubic spline interpolation, a bicubic interpolation approach [92] is designed to manipulate with 2-D rectangular surfaces. This approach is based on an assumption that the value of a bivariate function at some point with coordinates (x, y) within a rectangular region $[x_{i-1}, y_{i-1} \dots x_i, y_i]$ can be estimated as a value of

Figure 4.2. Evaluation of a first derivative along the x coordinate. The red circle marks the reference point which together with 3 green tabulated points forms an adjacent points set. The selected nearest points outside of the adjacent points set are marked in blue. The orange line represent a least-square-line.

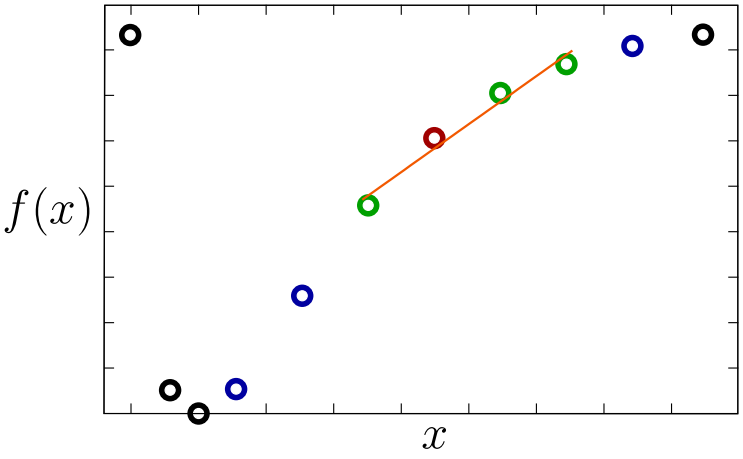

the following bivariate piecewise cubic polynomial:

$$f_i(x,y) = \sum_{k=0}^{3}\sum_{l=0}^{3} A_i^{(kl)}(x-x_i)^k(y-y_i)^l, \tag{4.3}$$

where $A^{(kl)}$ are 16 polynomial coefficients specific for a particular rectangular region. These coefficients are computed from four values of interpolated function at the tabulated grid point in the corners of the region along with values of the first partial derivatives $(\partial f_i(x,y)/\partial x,\ \partial f_i(x,y)/\partial y)$ and mixed second partial derivatives $(\partial^2 f_i(x,y)/(\partial x \partial y))$ at these reference grid points. However, the value of these derivatives are often unknown *a priori* and need to be computed numerically from known tabulated values. The bicubic interpolation approach does not specify how exactly the evaluation of these derivatives should be performed. Moreover, as the accuracy of an interpolated surface depends mainly on the accuracy of these derivatives, a differentiation algorithm should be chosen carefully.

PVSCF program uses an approach suggested by Akima [93] for this purpose. Using the example of a one-dimensional function, the first partial derivative over x at the grid point x_i can be computed within this framework through the following steps (see Figure 4.2):

1. Select the nearest six grid points in such a way that three of them are located to the left of the reference tabulated grid point x_i, while the other three ones are located to the right of x_i. If the reference point x_i does not have enough neighbours on one of the sides, all available points from this side have to be selected. Using these six grid points group them into four adjacent sets in such a way that each adjacent set contains the reference grid point x_i.

2. For each adjacent set of four points calculate the coefficients of a cubic polynomial. These coefficients are then used to compute four primary estimates of the first partial derivative at the grid point x_i (one for each point set).

3. For every adjacent set:

   (a) Fit the points with least-squares line and compute the variability factor by summing up the squares of the deviations between the actual value of the function at the grid point and the predicted value using this least-squares-line.

   (b) Compute the distance factor by summing up the squares of the distances between x_i and its three neighbours in a set.

   (c) Compute a weight factor by multiplying the variability factor and corresponding distance factor.

4. Normalise the obtained four weight factors and use them to compute the value of the first partial derivative over x at the grid point x_i by averaging four primary estimates.

The mixed second-order partial derivatives are computed using a similar algorithm, except of the fact that six nearest grid points are selected along both x and y direction at the step 1. It follows, therefore, that 16 primary estimates, instead of just four ones, need to be precomputed and that a least-squares-fit plane instead of the least-squares-fit line have to be used at the step 3a.

The bicubic interpolation can be generalised for m-dimensional (m-D) surfaces giving m-cubic interpolation. Unfortunately, the complexity of the algorithm increases

significantly with the number of dimensions. Thus in case of 3-dimensional PES 64 polynomial coefficients have to be determined, that is four times larger in comparison with bicubic interpolation approach. Moreover, as the number of these polynomial coefficients is increased, all mixed partial derivatives up to the third order are now required for each tabulated point on the 3-D grid. Unfortunately, as the main bottleneck of such algorithms is the accurate evaluation of these partial derivatives, using m-cubic interpolation for the large m may be impractical.

4.2.3 Shepard interpolation

Against this background, a Shepard interpolation algorithm [94, 95] looks particularly promising. In fact, the Shepard interpolation is a specific instance of a more general approach called normalized radial basis function interpolation [92, p. 139], as it uses a weight factor based on a distance between grid points. Within the Shepard interpolation, a function of m variables $f(\mathbf{Q}) = f(Q^{(1)}, Q^{(2)}, \ldots, Q^{(m)})$ defined on a grid is expanded in a Taylor series in the neighbourhood of each tabulated point $\mathbf{Q_j} = (Q^{(1)}_{j_1}, Q^{(2)}_{j_2}, \ldots, Q^{(m)}_{j_m})$:

$$\begin{aligned} f_{\mathbf{j}}(\mathbf{Q}) &= f(\mathbf{Q_j}) + \sum_{k=1}^{m} \left[Q^{(k)} - Q^{(k)}_{j_k}\right] \frac{\partial f(\mathbf{Q})}{\partial Q^{(k)}} \Bigg|_{\mathbf{Q}=\mathbf{Q_j}} \\ &+ \frac{1}{2!} \sum_{k=1}^{m} \sum_{l=1}^{m} \left[Q^{(k)} - Q^{(k)}_{j_k}\right] \left[Q^{(l)} - Q^{(l)}_{j_l}\right] \frac{\partial^2 f(\mathbf{Q})}{\partial Q^{(k)} \partial Q^{(l)}} \Bigg|_{\mathbf{Q}=\mathbf{Q_j}} + \ldots . \end{aligned} \quad (4.4)$$

By substituting actual coordinates of the point in question $\mathbf{Q}$ into Eq. (4.4), a primary estimate of the value of the function $f(\mathbf{Q_j})$ with respect to the tabulated point $\mathbf{Q_j}$ can be computed. In case of complete expansion, the value of these estimates does not depend from the reference point $\mathbf{Q_j}$ used, but it does in case of a truncated series. For this reason, in order to obtain the approximate value of $f(\mathbf{Q})$, all estimates are averaged as follows:

$$f(\mathbf{Q}) = \sum_{\mathbf{j}=1}^{n_1 \cdot n_2 \cdot \ldots \cdot n_m} W_{\mathbf{j}}(\mathbf{Q}) f_{\mathbf{j}}(\mathbf{Q}), \quad (4.5)$$

$$W_{\mathbf{j}}(\mathbf{Q}) = \frac{w_{\mathbf{j}}(\mathbf{Q})}{\sum_k w_{\mathbf{k}}(\mathbf{Q})}, \quad (4.6)$$

where n_i is the number of tabulated grid points along the i-th coordinate. There are several ways to define the weight function $w_k(\mathbf{Q})$ [94]. All of these factors, however, depend on the inverse distance between the reference point and the point in question, as for smooth functions the Taylor series [Eq. (4.4)] converges faster with decreasing this distance.

One of the most significant advantage of the Shepard interpolation is its high scalability with increasing of the dimensionality of a PES. Thus, even in case of complete decomposition, its complexity increases by the factor of $[\exp(1 + 1/m) - 1]n_{m+1}$ with increasing the number of dimensions from m to $m + 1$, where n_{m+1} is the number of tabulated grid points along the new $m+1$-th dimension. In particular, for large m the complexity of incrementing the number of dimension approaches the value of $1.7n_{m+1}$ asymptotically. The actual factor, however, is even smaller as not all terms in the Taylor series (4.4) need to be computed. Moreover, in contrast with m-cubic interpolation, the maximal order of partial derivatives which need to be evaluated is usually small and remains constant for surfaces of any dimensionality. This makes the Shepard interpolation approach more preferable for the large m.

The Shepard interpolation as implemented in PVSCF can deal with the PES of any dimensionality. The following steps are applied separately for each coupling term:

1. All partial derivatives of the function $f(\mathbf{Q})$ are computed numerically up to the certain order at each tabulated point. The differentiation is performed recursively using difference formulae of the first- and the second-order from Ref. [96, p. 884]. Despite the absence of any algorithmic limitations of the maximal order of derivatives, it is limited in practice by accumulation of numerical errors during recursive differentiation. This is usually not a problem, because the convergence of Eq. (4.4) can be improved by increasing the number of tabulated points. Alternatively, this computational error can be reduced by using analytical derivatives of the lowest orders. In particular, the availability of such derivatives can significantly reduce the number of reference grid points and, as a sequence, to accelerate the construction of a PES [97, 98]. Moreover, some insight into the

nature of the high-order coupling terms can be revealed that leads to additional acceleration [99] At the current stage, however, we compute analytical derivatives and estimates them numerically using the sparse PES only. This is caused by the limitation of the PVSCF code which forgets about transformation between the Cartesian and normal coordinates since the construction of the PES has been done. However, this transformation has to be retained, as analytical derivatives provided by electronic structure programs are usually computed in Cartesian coordinates.

2. For all interpolation point:

   (a) Check if it coincides with a tabulated one. Return the found tabulated value if coincidence was detected.

   (b) Otherwise compute primary estimates in the vicinity of the target point and average them using the following weight function:

$$w_{\mathbf{j}}(\mathbf{Q}) = \left(\sum_{k=1}^{m} \left(Q^{(k)} - Q_{j_k}^{(k)} \right)^2 \right)^{-p}, \tag{4.7}$$

   where p is some positive number. Ishida and Schatz [100] and Oyanagi et al. [98] demonstrated that $p = 6$ is a very reliable choice in terms of accuracy. Moreover, it leads to a rapid decay of the weight function $w_{\mathbf{j}}(\mathbf{Q})$ with the distance between target and tabulated points, and makes conditions for rapid convergence of the interpolated energy with respect to a number of used tabulated points. Thus, all tabulated points are sorted in terms of the distance to the reference point in ascent order. The interpolation continues as long as the total contribution to the energy from all equidistant points is greater than a threshold $\Delta E_s^{\max} = 10^{-10}$ Hartree with introducing the next distance (see Figure 4.3).

To validate the correctness of the implementation of these three interpolation techniques, vibrational frequencies for three test systems were calculated using PES interpolated with different approaches. Of course, the accuracy of the cubic spline

Figure 4.3. Interpolation of the pair coupling term between symmetric (Q_1) and antisymmetric (Q_2) OH stretching modes of a water molecule computed at the CCSD(T)/aug-cc-pVQZ level of theory. The width of a line passing through tabulated points schematically represents the weight of the estimate $w_{\mathbf{j}}(\mathbf{Q})$ with respect to the target point (in black).

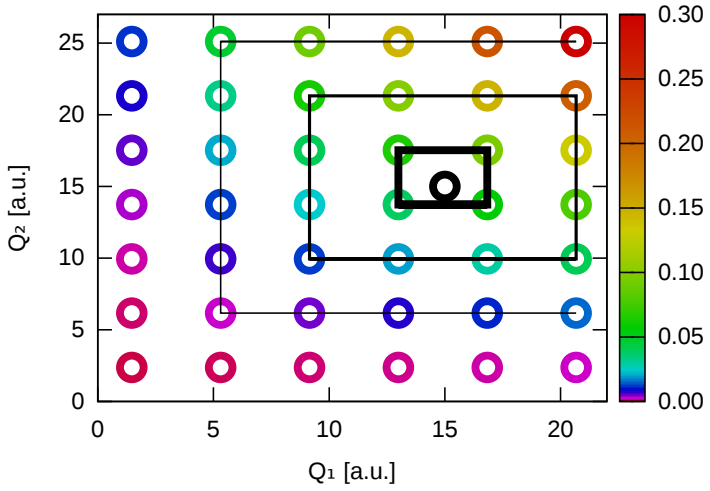

interpolation and bicubic interpolation cannot be directly compared with each other as this techniques designed the surfaces with different dimensionality. However, these techniques can be justified against the Shepard interpolation, as the last one was implemented in general m-D case and can be applied to surfaces of any dimensionality.

4.2.4 Test system: a Morse oscillator

The first test system is a Morse oscillator whose Hamiltonian in atomic units is expressed in a form:

$$\hat{H} = -\frac{1}{2\mu}\frac{\partial^2}{\partial R^2} + D_e\left[1 - e^{-\alpha R}\right]^2, \tag{4.8}$$

with the following parameters (in atomic units): $D_e = 0.1740$, $\alpha = 1.0346$, $\mu = 918.6811$. This oscillator corresponds to the stretching mode of a H_2 molecule in the gas phase. These parameters were determined by fitting the *ab initio* 1-D PES of a H_2 molecule in the gas phase obtained at the CCSD(T) / aug-cc-pVQZ level of theory. The advantage of this system is that the transition frequencies can be calculated analytically using Eq. (2.23).

A test PES was precomputed on a 16 point uniform grid on the interval between -0.75 Bohrs and 2.75 Bohrs from the equilibrium point. This PES was then interpolated

Table 4.1. First eight vibrational eigenvalues of the Morse oscillator computed within FGH approach using PES-s obtained with cubic spline interpolation and 1-D Shepard interpolation up to the second- and the third-order. Relative CPU time is estimated based on interpolation of 10^6 curves. Eigenvalues are given in cm^{-1}.

v	0	1	2	3	4	5	6	7	RMSD	Time
Analytical	2178	6341	10248	13900	17296	20437	23321	25950	—	—
Cubic spline	2186	6344	10231	13866	17262	20413	23312	25954	20	1
Shepard (2)	2180	6345	10252	13901	17297	20438	23324	25952	3	14
Shepard (3)	2178	6341	10249	13900	17296	20436	23321	25949	1	20

on the uniform grid with 128 points using natural cubic splines. At the same time, extra two interpolated PES-s were obtained using the Shepard interpolation algorithms where all derivatives up to the 2nd and the 3rd order derivatives were taken into account. The vibrational eigenvalues for the ground state and for the first seven excited states were obtained using three different PES along with the corresponding exact analytical solution are shown in Table 4.1.

The results obtained using the PES interpolated with the Shepard interpolation technique perfectly match the analytical solution. Thus, when all the third order derivatives in Eq. (4.4) are taken into account, the RMSD averaged over these 8 states lies within 1 cm^{-1} which is within the spectroscopic accuracy. Decreasing the level of approximation down to the second order terms increases the RMSD up to 3 cm^{-1}.

Alternatively, in contrast with the Shepard interpolation up to the third derivatives, cubic spline interpolation can boost the performance up to 20 times. However, the cubic spline interpolation can introduce a relatively large error on a very sparse grid. Thus, in this case the RMSD value over the lowest eight eigenvalues is equal to 20 cm^{-1}. The main contribution to this error comes from excited states with vibrational quantum number v between 2 and 5 inclusively. The reason being that he energy raises very rapidly with the reduction of the inter-atomic distance beyond the equilibrium position, but only 4 tabulated points reside in this region. Despite of the fact, that an extra tabulated point reduces the RMSD down to 1 cm^{-1} for all interpolation techniques, the Shepard interpolation is the most robust as it allows to obtain very accurate results regardless of the sampling technique.

4.2.5 Two-dimensional test case: two oscillators in Henon-Heiles potential

As the second test the eigenstates of a system of two oscillators coupled together by the Henon-Heiles potential were computed. This potential was originally introduced by Contopoluos [101] to describe a motion of stars in a galaxy and then was generalised Henon and Heiles [102]. The potential reads:

$$V(Q_1, Q_2) = \frac{1}{2}\omega_1^2 Q_1^2 + \frac{1}{2}\omega_2^2 Q_2^2 + \lambda Q_1 \left(\eta Q_1^2 + Q_2^2\right), \tag{4.9}$$

with parameters ω_1^2 = 0.29375, ω_2^2 = 2.12581, λ = -0.1116, η = 0.08414 [103]. This set of parameters makes the frequencies to be sensitive to errors incurred by numerical computation. For this reason, it is often used to test various numerical algorithms [22, 60].

A 2-D test PES was precomputed on the 8×8 uniform grid on the intervals between -9.0 Bohrs and 9.0 Bohrs and between -6.0 Bohrs and 6.0 Bohrs along the first and the second vibrational mode respectively. This PES was than interpolated on the uniform 128×128 grid using bicubic interpolation and the Shepard interpolation with all derivatives up to the second and the third order. To maintain the experimental integrity, two 1-D PES were generated on the dense uniform grid with 128 points along each mode. The vibrational eigenvalues were computed using VSCF/VCI method with configuration space limited up to 7 excitation quanta for each normal mode.

The comparison between different interpolation techniques are given in Table 4.2. Bicubic interpolation demonstrates the excellent performance, however the eigenvalues differ from exact solution by 0.0009 Hartree according to the RMSD. When only the second derivatives are taken into account, the Shepard interpolation demonstrates an increased RMSD (by 30%) coincidently with increasing in time by factor of 7. Third-order derivatives doubles the time consumption of the Shepard interpolation dramatically improving accuracy (up to 0.0001 Hartree).

Table 4.2. Deviation of the first four vibrational eigenvalues of 2-D oscillator in the Henon-Heiles potential from the exact quantum solution. Relative CPU time was estimated based on interpolation of 10^4 PES. Eigenvalues are given in Hartree.

(v_1, v_2)	(0,0)	(1,0)	(2,0)	(1,1)	RMSD, 10^{-3}	Rel. CPU Time
Exact quantum [103]	0.9916	1.5159	2.0308	2.4188	—	—
Bicubic	0.0002	-0.0004	-0.0005	0.0017	0.9	1
Shepard (2)	0.0004	0.0001	-0.0019	0.0014	1.2	7
Shepard (3)	0.0000	0.0001	0.0001	0.0001	0.1	14

Note, that in this test the number of grid points along each mode is only half as much as in the previous 1-D test. In case of 2-D PES computed on the 16×16 grid all three methods yield identical results, and the RMSD is equal to 0.0001 Hartree for all of them. For this reason, despite of the excessive time consumption, the Shepard (3) method can significantly increase the overall performance because it requires a sparser grid for the same accuracy.

4.3 A general VSCF algorithm

Jung and Gerber's variant [44] of the vibrational self-consistent field (VSCF) method, which has been described in Section 2.5, does not rely on any representation of the potential $V(\mathbf{Q})$. It is possible, however, to accelerate this algorithm slightly by simplifying the form of the effective potential V_i^{eff} [Eq. (2.36)]. Thus, splitting the potential into diagonal and coupling terms

$$V(\mathbf{Q}) = \sum_{i=1}^{N} V_i^{(1)}(Q_i) + V_c(\mathbf{Q}) \tag{4.10}$$

allows to group these diagonal terms together with the kinetic energy operator:

$$\hat{h}(\mathbf{Q}) = \sum_{i=1}^{N} \hat{h}_i(Q_i) = \sum_{i=1}^{N} \left(-\frac{1}{2}\frac{\partial^2}{\partial Q_i^2} + V_i^{(1)}(Q_i) \right). \tag{4.11}$$

The vibrational Schrödinger equation (2.33) for a state $\mathbf{v}$ takes an equivalent form up to notation:

$$\left\{\sum_{i=1}^{N}\hat{h}_i(Q_i)+V_c(\mathbf{Q})\right\}\Psi^{\mathbf{v}}(\mathbf{Q})=E_{\mathbf{v}}^{\mathrm{VSCF}}\Psi^{\mathbf{v}}(\mathbf{Q}), \tag{4.12}$$

Therefore, on a subspace of factorizable wave functions $\Psi^{\mathbf{v}}(\mathbf{Q})$ [Eq. (2.34)] is reduced to the system of 1-D Schrödinger equations:

$$\left\{\hat{h}_i(Q_i)+\bar{V}_{i;\mathbf{v}}^{\mathrm{eff}}(\mathbf{Q})\right\}\phi_i^{v_i}(Q_i)=\bar{\epsilon}_i^{v_i}\phi_i^{v_i}(Q_i), \tag{4.13}$$

where $\phi_i^{v_i}(Q_i)$ and $\bar{\epsilon}_i^{v_i}$ are modal wave functions and corresponding VSCF modal energies. However, in contrast with Jung and Gerber's formulation, the effective potential

$$\bar{V}_{i;\mathbf{v}}^{\mathrm{eff}}(\mathbf{Q})=\left\langle\prod_{j\neq i}^{N}\phi_j^{v_j}(Q_j)\,|V_c(\mathbf{Q})|\prod_{j\neq i}^{N}\phi_j^{v_j}(Q_j)\right\rangle \tag{4.14}$$

does not contain any diagonal terms from $V(\mathbf{Q})$, This allows to avoid evaluation of N one-dimensional integrals and, as a result, slightly improves the performance of the algorithm. Elimination of diagonal terms from multi-dimensional potential, of course, alters modal energies according to relation:

$$\epsilon_i^{v_i}=\bar{\epsilon}_i^{v_i}+\sum_{j\neq i}^{N}\left\langle\phi_j^{v_j}(Q_j)\left|V_i^{(1)}(Q_i)\right|\phi_j^{v_j}(Q_j)\right\rangle. \tag{4.15}$$

However, the VSCF total energy remains unchanged:

$$\begin{aligned}
E_{\mathbf{v}}^{\mathrm{VSCF}}&=\sum_{i=1}^{N}\bar{\epsilon}_i^{v_i}-(N-1)\left\langle\phi_1^{v_1}(Q_1)\left|V_{1;\mathbf{v}}^{\mathrm{eff}}\right|\phi_i^{v_1}(Q_1)\right\rangle\\
&=\sum_{i=1}^{N}\bar{\epsilon}_i^{v_i}-(N-1)\left\langle\prod_{i=1}^{N}\phi_i^{v_i}(Q_i)\,|V_c(\mathbf{Q})|\prod_{i=1}^{N}\phi_i^{v_i}(Q_i)\right\rangle\\
&=\sum_{i=1}^{N}\epsilon_i^{v_i}-(N-1)\left\langle\prod_{i=1}^{N}\phi_i^{v_i}(Q_i)\left|\sum_{j=1}^{N}V_1^{(1)}(Q_i)+V_c(\mathbf{Q})\right|\prod_{i=1}^{N}\phi_i^{v_i}(Q_i)\right\rangle
\end{aligned} \tag{4.16}$$

due to equality of Hamiltonians in Eqs. (2.33) and (4.12). Note, that the VSCF method was originally invented by Bowman [22, 104] following this strategy.

An extra acceleration in performance can be achieved by expressing the coupling potential $V_c(\mathbf{Q})$ using many-mode expansion [Eq. (2.38)]:

$$V_c(\mathbf{Q}) = \sum_{i=1}^{N}\sum_{j>i}^{N} V_{ij}^{(2)}(Q_i, Q_j) + \sum_{i=1}^{N}\sum_{j>i}^{N}\sum_{k>j}^{N} V_{ijk}^{(3)}(Q_i, Q_j, Q_k) + \dots \tag{4.17}$$

Considering the effective potential [Eq. (4.14)] for the mode i, all coupling terms can be divided into two groups according to their dependence on the i-th coordinate:

$$\begin{aligned}
\bar{V}_{i;\mathbf{v}}^{\text{eff}}(\mathbf{Q}) &= \left\langle \prod_{j\neq i}^{N} \phi_j^{v_j}(Q_j) \middle| \sum_{j=1}^{N}\sum_{k>j}^{N} V_{jk}^{(2)}(Q_j, Q_k) + \dots \middle| \prod_{j\neq i}^{N} \phi_j^{v_j}(Q_j) \right\rangle \\
&= \underbrace{\sum_{j\neq i}^{N} \left\langle \phi_j^{v_j}(Q_j) \middle| V_{ij}^{(2)}(Q_i, Q_j) \middle| \phi_j^{v_j}(Q_j) \right\rangle + \dots}_{\tilde{V}_{i;\mathbf{v}}^{\text{eff}}(\mathbf{Q})} \\
&\quad + \underbrace{\sum_{j\neq i}^{N}\sum_{k>j}^{N} \left\langle \phi_j^{v_j}(Q_j)\phi_k^{v_k}(Q_k) \middle| V_{jk}^{(2)}(Q_j, Q_k) \middle| \phi_k^{v_k}(Q_k)\phi_j^{v_j}(Q_j) \right\rangle + \dots .}_{\text{constant terms}}
\end{aligned} \tag{4.18}$$

If the dependence takes place, then averaging of such terms over all but the i-th vibrational coordinate leads to non-trivial one-dimensional operators which have to be taken into account. At the same time, the contribution from the remaining couplings to the effective potential does not depends on the i-th coordinate at all. These constant terms simply shift the i-th modal energy without any influence on the corresponding modal wave function, therefore they can be ignored. As a price, this trick complicates the expression for the VSCF total energy through the modal energies $\tilde{\epsilon}_i^{v_i}$:

$$\begin{aligned}
E_{\mathbf{v}}^{\text{VSCF}} &= \sum_{i=1}^{N} \tilde{\epsilon}_i^{v_i} - \left\langle \prod_{i=1}^{N} \phi_i^{v_i}(Q_i) \middle| \sum_{i=1}^{N}\sum_{j>i}^{N} V^{(2)}(Q_i, Q_j) \middle| \prod_{i=1}^{N} \phi_i^{v_i}(Q_i) \right\rangle \\
&\quad - 2\left\langle \prod_{i=1}^{N} \phi_i^{v_i}(Q_i) \middle| \sum_{i=1}^{N}\sum_{j>i}^{N}\sum_{k>j}^{N} V^{(3)}(Q_i, Q_j, Q_k) \middle| \prod_{i=1}^{N} \phi_i^{v_i}(Q_i) \right\rangle - \dots .
\end{aligned} \tag{4.19}$$

Note that this above formula is non-optimal, as it requires evaluation of all constant terms from Eq. (4.18) (in number of couplings) that we try to avoid. Instead, the equation above can be rewritten in an equivalent form introducing a corrective

effective potential, $\mathring{V}^{\text{eff}}_{i;\mathbf{v}}$:

$$E^{\text{VSCF}}_{\mathbf{v}} = \sum_{i=1}^{N} \tilde{\epsilon}_i^{v_i} - \underbrace{\sum_{i=1}^{N} \left\langle \phi_i^{v_i}(Q_i) \left| \mathring{V}^{\text{eff}}_{i;\mathbf{v}}(Q_i) \right| \phi_i^{v_i}(Q_i) \right\rangle}_{\Delta \tilde{E}_{\mathbf{v}}} . \tag{4.20}$$

This corrective potential contains only integrals which have already been evaluated during the construction of the effective potential $\tilde{V}^{\text{eff}}_{i;\mathbf{v}}(\mathbf{Q})$:

$$\begin{aligned} \mathring{V}^{\text{eff}}_{i;\mathbf{v}} = {} & \frac{1}{2} \sum_{j \neq i}^{N} \left\langle \phi_j^{v_j}(Q_j) \left| V^{(2)}_{ij}(Q_i, Q_j) \right| \phi_j^{v_j}(Q_j) \right\rangle \\ & + \frac{2}{3} \sum_{j \neq i}^{N} \sum_{k > j}^{N} \left\langle \phi_j^{v_j}(Q_j) \phi_k^{v_k}(Q_k) \left| V^{(3)}_{ijk}(Q_i, Q_j, Q_k) \right| \phi_k^{v_k}(Q_k) \phi_j^{v_j}(Q_j) \right\rangle + \dots . \end{aligned} \tag{4.21}$$

Here, the coefficient in front of the m-D coupling integrals is equal to $(m-1)/m$. Its numerator comes from Eq. (4.20) and is caused by the fact that the contribution from each m-D coupling term to the total energy has been counted m times instead of once. Moreover, each coupling term contributes to the corrective effective potential multiple times – once per coupled mode – that requires an additional scale factor $1/m$.

In PVSCF, evaluation of components of the effective potential is implemented by sequential reduction of their dimensionality. Thus, in order to compute a contribution to the $\tilde{V}^{\text{eff}}_{i;\mathbf{v}}(\mathbf{Q})$ from a 3-D coupling term $V_{ijk} = V^3_{ijk}(Q_i, Q_j, Q_k)$, this coupling can be firstly averaged over the k-th vibrational coordinate:

$$V^k_{ij}(Q_i, Q_j) = \left\langle \phi_k^{v_k}(Q_k) \left| V_{ijk}(Q_i, Q_j, Q_k) \right| \phi_k^{v_k}(Q_k) \right\rangle , \tag{4.22}$$

followed by averaging of the obtained 2-D potential over the j-th coordinate:

$$V^{jk}_i(Q_i) = \left\langle \phi_j^{v_j}(Q_j) \left| V^k_{ij}(Q_i, Q_j) \right| \phi_j^{v_j}(Q_j) \right\rangle . \tag{4.23}$$

Unfortunately, because coupling terms are defined numerically on a grid, computational costs increase exponentially with the dimensionality of an averaging coupling.

Figure 4.4. Evaluation of components of the effective potential by following the shortest route (a) and by combining similar coupling terms (b). Subscript indices denote modes which are coupled through the coupling term, while superscript indices correspond to modes over which the coupling term has already been averaged. Vertical line in subscript dichotomizes the coupled modes and marks the branch point of the shortest path algorithm. The coupling term which is shown in a dashed line may be integrated separately, as it only increases overall performance in specific circumstances (see text).

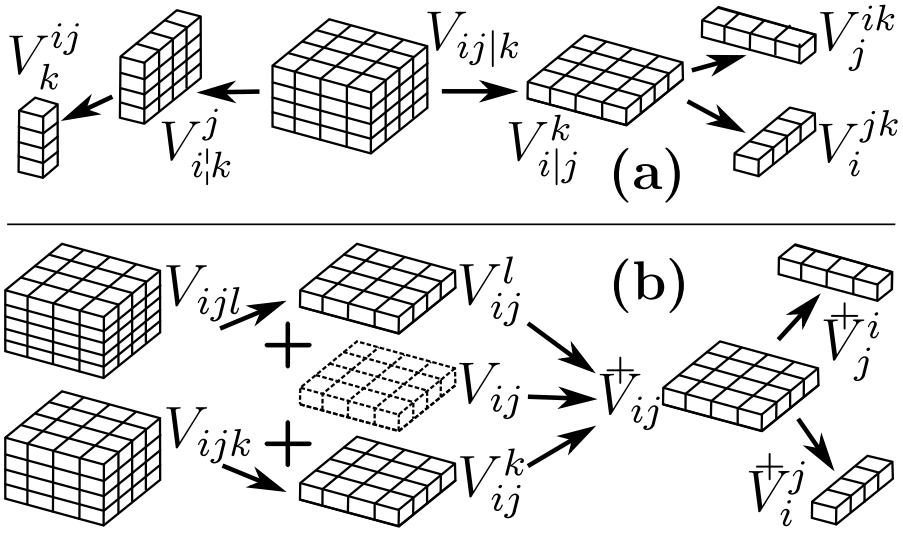

Thus, in case of uniformly distributed grid with n points along each mode, in order to average an m-D coupling term along one mode n^{m-1} integrals should be computed. Because for an accurate numerical integration the number of grid points should be relatively large, minimizing the number of high-dimensional couplings which have to be integrated is of critical importance.

To improve the performance, we use two approaches which are shown in Figure 4.4. The first approach finds the shortest route that gives the contributions from the particular coupling term to the effective potential along each coupled mode. The method is based on independence of averaged coupling terms from changing the order of integration. For example, the term $V_j^{ik}(Q_j)$, which contributes to the $\tilde{V}_{j;\mathbf{v}}^{\mathrm{eff}}(Q_j)$, can be obtained from $V_{ijk}(Q_i, Q_j, Q_3)$ by averaging over the mode k followed by averaging over the mode i. As an alternative route, one can use integration in inverse order. However, if the term $V_i^{jk}(Q_i)$ has previously been computed using Eq. (4.3), the term $V_{ij}^{k}(Q_i, Q_j)$ is already known. This makes the former route to be more optimal than the latter one, as it allows to skip unnecessary averaging of the 3-D coupling.

In general, the most optimal route can be found using a bisection method. Thus, all modes which are coupled together through the particular coupling term are divided into two groups with the same size. The coupling term is then averaged over the modes in each group independently, that gives two complementary directions. The procedure is applied recursively for each reduced coupling term until all of them become one-dimensional.

The construction of the effective potential can be further accelerated by combining the similar coupling terms and averaging them simultaneously. Supposing that in addition to the coupling term V_{ijk} there is also a term V_{ijl}. Being averaged over the l-th coordinate, the latter term transforms into the reduced term $V^l_{ij}(Q_i, Q_j)$. As well as $V^k_{ij}(Q_i, Q_j)$, this term contributes to the effective potential over the i-th and j-th coordinates, and for this reason they can be merged together and integrated simultaneously. Additionally, these terms could even be combined with a pair-coupling $V_{ij}(Q_i, Q_j)$. In most cases, however, mixing couplings of different dimensionality is not profitable. The reason being that the corrective potential $\mathring{V}^{\text{eff}}_{i;\mathbf{v}}(Q_i)$ should be also computed in order to calculate the VSCF total energy. Unfortunately, potentials $\tilde{V}^{\text{eff}}_{i;\mathbf{v}}(Q_i)$ and $\mathring{V}^{\text{eff}}_{i;\mathbf{v}}(Q_i)$ contain different scale factors, that leads to impossibility to construct such corrective potential using only precomputed components. However, this variant of contraction can be in principle helpful at intermediate VSCF iterations, if an alternative convergence criteria, such as the sum of modal energies itself, is used.

4.4 A general VSCF/VCI algorithm

The VSCF state energy $E^{\text{VSCF}}_{\vec{v}}$ obtained for the $\mathbf{v}$-th vibrational state can be further improved using a state-specific vibrational configuration interaction (VSCF/VCI) method described in Section 2.5. Within this approach a series of configuration state functions (CSFs), $\Psi^{\mathbf{u}}_{\mathbf{v}}$, is constructed from orthonormal VSCF modal wave functions,

$\psi_i^{u_i;(\mathbf{v})}(Q_i)$, optimized for the reference state $\mathbf{v}$:

$$\Psi_{\mathbf{v}}^{\mathbf{u}}(\mathbf{Q}) = \prod_{i=1}^{N} \psi_i^{u_i;(\mathbf{v})}(Q_i). \tag{4.24}$$

A symmetric VCI matrix is then computed on the basis of CSFs:

$$H_{\mathbf{uw}}^{\mathrm{VCI}} = H_{\mathbf{uw}}^{\mathrm{VCI}} = \left\langle \Psi_{\mathbf{v}}^{\mathbf{u}} \left| \mathbf{H} \right| \Psi_{\mathbf{v}}^{\mathbf{w}} \right\rangle. \tag{4.25}$$

Finally, the VCI energy of the $\mathbf{v}$-th state is obtained by diagonalisation of this VCI matrix.

For the PES expressed in terms of many-mode representation [Eq. (2.38)] a Hamiltonian matrix element between two CSF, $\Psi_{\mathbf{v}}^{\mathbf{u}}$ and $\Psi_{\mathbf{v}}^{\mathbf{w}}$, denotes as:

$$H_{\mathbf{uw}} = \left\langle \prod_{i=1}^{N} \phi_i^{u_i;(\mathbf{v})}(Q_i) \left| \sum_{i=1}^{N} \hat{h}_i(Q_i) + V_c(\mathbf{Q}) \right| \prod_{i=1}^{N} \phi_i^{w_i;(\mathbf{v})}(Q_i) \right\rangle, \tag{4.26}$$

where the diagonal operator is defined in Eq. (4.11). By adding and subtracting an effective potential $V_{i;\mathbf{v}}^{\mathrm{eff}}(Q_i)$ to the Hamiltonian operator, this matrix element can be split into three parts:

$$\begin{aligned} H_{\mathbf{uw}} = & \underbrace{\left\langle \prod_{i=1}^{N} \phi_i^{u_i;(\mathbf{v})}(Q_i) \left| \sum_{i=1}^{N} \left\{ \hat{h}_i(Q_i) + V_{i;\mathbf{v}}^{\mathrm{eff}}(Q_i) \right\} \right| \prod_{i=1}^{N} \phi_i^{w_i;(\mathbf{v})}(Q_i) \right\rangle}_{H_{\mathbf{uw}}^{\mathrm{a}}} \\ & \underbrace{- \left\langle \prod_{i=1}^{N} \phi_i^{u_i;(\mathbf{v})}(Q_i) \left| \sum_{i=1}^{N} V_{i;\mathbf{v}}^{\mathrm{eff}}(Q_i) \right| \prod_{i=1}^{N} \phi_i^{w_i;(\mathbf{v})}(Q_i) \right\rangle}_{H_{\mathbf{uw}}^{\mathrm{b}}} \\ & \underbrace{+ \left\langle \prod_{i=1}^{N} \phi_i^{u_i;(\mathbf{v})}(Q_i) \left| V_c(\mathbf{Q}) \right| \prod_{i=1}^{N} \phi_i^{w_i;(\mathbf{v})}(Q_i) \right\rangle}_{H_{\mathbf{uw}}^{\mathrm{c}}}. \end{aligned} \tag{4.27}$$

Note, that we make no assumption about the form of $V_{i;\mathbf{v}}^{\mathrm{eff}}(Q_i)$. Therefore, it may be defined either as $\bar{V}_{i;\mathbf{v}}^{\mathrm{eff}}(Q_i)$ [Eq. (2.36)] or as $\tilde{V}_{i;\mathbf{v}}^{\mathrm{eff}}(Q_i)$ [Eq. (4.18)] depending on the used VSCF formalism.

The first term in Eq. (4.27) can be simplified by considering the orthonormality of the modal wave functions. Thus, taking the summation sign out of the brackets gives:

$$H^{\mathrm{a}}_{\mathbf{uw}} = \sum_{i=1}^{N} \left\langle \phi_i^{u_i;(\mathbf{v})}(Q_i) \left| \left[\left\{ \hat{h}_i(Q_i) + V^{\mathrm{eff}}_{i;\mathbf{v}}(\mathbf{Q}) \right\} \right| \phi_i^{w_i;(\mathbf{v})}(Q_i) \right\rangle \right] \prod_{j \neq i}^{N} \delta_{u_j,w_j}, \tag{4.28}$$

where δ_{u_j,w_j} is a Kronecker's delta function. Moreover, because the expression in square brackets is the left-hand side of a 1-D Schrödinger equation (4.13) and because all the modal wave functions are solutions of that equation, $H^{\mathrm{a}}_{\mathbf{uw}}$ can be expressed in terms of modal energies $\epsilon_i^{u_i;(\mathbf{v})}$:

$$H^{\mathrm{a}}_{\mathbf{uw}} = \sum_{i=1}^{N} \epsilon_i^{w_i;(\mathbf{v})} \left\langle \phi_i^{u_i;(\mathbf{v})}(Q_i) \mid \phi_i^{u_i;(\mathbf{w})}(Q_i) \right\rangle \prod_{j \neq i}^{N} \delta_{u_j,w_j} = \delta_{\mathbf{u},\mathbf{w}} \sum_{i=1}^{N} \epsilon_i^{u_i;(\mathbf{v})}. \tag{4.29}$$

The second term in Eq. (4.27) can be simplified in a similar fashion. Thus, applying the orthonormality condition one can obtain:

$$H^{\mathrm{b}}_{\mathbf{uw}} = -\sum_{i=1}^{N} \left\langle \phi_i^{u_i;(\mathbf{v})}(Q_i) \left| V^{\mathrm{eff}}_{i;\mathbf{v}}(\mathbf{Q}) \right| \phi_i^{w_i;(\mathbf{v})}(Q_i) \right\rangle \prod_{j \neq i}^{N} \delta_{u_j,w_j}. \tag{4.30}$$

There are three possible cases depending on the CSFs $\Psi^{\mathbf{u}}_{\mathbf{v}}(\mathbf{Q})$ and $\Psi^{\mathbf{w}}_{\mathbf{v}}(\mathbf{Q})$:

$$H^{\mathrm{b}}_{\mathbf{uw}} = \begin{cases} -\sum_{i=1}^{N} \left\langle \phi_i^{u_i;(\mathbf{v})}(Q_i) \left| V_i^{\mathrm{eff}}(Q_i) \right| \phi_i^{u_i;(\mathbf{v})}(Q_i) \right\rangle, & \forall i : u_i = w_i; \\ -\left\langle \phi_k^{u_k;(\mathbf{v})}(Q_k) \left| V_k^{\mathrm{eff}}(Q_k) \right| \phi_k^{w_k;(\mathbf{v})}(Q_k) \right\rangle, & \forall i \neq k : u_i = w_i, u_k \neq w_k; \\ 0, & \text{otherwise.} \end{cases} \tag{4.31}$$

In case of diagonal matrix elements, $H^{\mathrm{b}}_{\mathbf{uu}}$, all delta functions in Eq. (4.30) are equal to unity, that transforms the term $H^{\mathrm{b}}_{\mathbf{uw}}$ into a sum of expectation values of the effective potential along each vibrational coordinate. Alternatively, when the CSFs differ in the k-th modal wave function, only the expectation value along this k-th coordinate persists. Finally, when the CSFs differ in more than one modal wave function, the terms $H^{\mathrm{b}}_{\mathbf{uu}}$ becomes constantly zero.

The last term in Eq. (4.27) is the most laborious one, because it requires the evaluation of multi-dimensional integrals. In many-mode expansion this term can be expressed as a sum of integrals:

$$H^{\mathrm{c}}_{\mathbf{uw}} = \sum_j \sum_{k>j} \left\langle \prod_{i=1}^{N} \phi_i^{u_i;(\mathbf{v})}(Q_i) \left| V^{(2)}_{jk}(Q_j, Q_k) \right| \prod_{i=1}^{N} \phi_i^{w_i;(\mathbf{v})}(Q_i) \right\rangle \tag{4.32}$$
$$+ \sum_j \sum_{k>j} \sum_{l>k} \left\langle \prod_{i=1}^{N} \phi_i^{u_i;(\mathbf{v})}(Q_i) \left| V^{(3)}_{jk}(Q_j, Q_k, Q_l) \right| \prod_{i=1}^{N} \phi_i^{w_i;(\mathbf{v})}(Q_i) \right\rangle + \dots .$$

However, some of these integrals are equal to zero and can be ignored. Thus, the orthonormality condition ensures that if the CSFs $\Psi^{\mathbf{u}}_{\mathbf{v}}(\mathbf{Q})$ and $\Psi^{\mathbf{w}}_{\mathbf{v}}(\mathbf{Q})$ differ in a mode that is not coupled through some coupling term, this coupling term does not contribute to the corresponding VCI matrix element at all. Moreover, if these CSFs differ from each other in m modal wave functions, all coupling terms up to the order $m-1$ can be ignored.

These obtained formulae can be validated against theory by considering two special cases. Thus, the diagonal VCI matrix element constructed from the VSCF reference state is equal to the VSCF energy:

$$H^{\mathrm{VCI}}_{\mathbf{vv}} = \sum_{i=1}^{N} \epsilon_i^{u_i;(\mathbf{v})} - \sum_{i=1}^{N} \left\langle \phi_i^{v_i;(\mathbf{v})}(Q_i) \left| V_i^{\mathrm{eff}}(Q_i) \right| \phi_i^{v_i;(\mathbf{v})}(Q_i) \right\rangle$$
$$+ \left\langle \prod_{i=1}^{N} \phi_i^{v_i;(\mathbf{v})}(Q_i) \left| V_c(\mathbf{Q}) \right| \prod_{i=1}^{N} \phi_i^{v_i;(\mathbf{v})}(Q_i) \right\rangle = E_i^{\mathrm{VSCF}}. \tag{4.33}$$

In particular, if the effective potential $\bar{V}_i^{\mathrm{eff}}(Q_i)$ is defined according to Eq. (4.14), the equation above is identical to Eq. (4.16) which defines the VSCF energy.

Alternatively, considering the matrix element $H^{\mathrm{VCI}}_{\mathbf{vu}}$, where the wave function $\Psi^{\mathbf{u}}_{\mathbf{v}}$ is different from the VSCF reference state by the k-th modal wave functions. It can

be proven, that this matrix element is constantly zero:

$$\begin{aligned} H^{\mathrm{VCI}}_{\mathbf{vu}} &= -\left\langle \phi_k^{v_k;(\mathbf{v})}(Q_k) \left| V^{\mathrm{eff}}_{k;\mathbf{v}}(Q_k) \right| \phi_k^{v_k;(\mathbf{v})}(Q_k) \right\rangle \\ &+ \left\langle \prod_{i=1}^{N} \phi_i^{v_i;(\mathbf{v})}(Q_i) \left| V_c(\mathbf{Q}) \right| \prod_{i=1}^{N} \phi_i^{v_i;(\mathbf{v})}(Q_i) \right\rangle \\ &= -\left\langle \phi_k^{v_k;(\mathbf{v})}(Q_k) \left| \bar{V}^{\mathrm{eff}}_{k;\mathbf{v}}(Q_k) \right| \phi_k^{v_k;(\mathbf{v})}(Q_k) \right\rangle \\ &+ \left\langle \phi_k^{v_k;(\mathbf{v})}(Q_k) \left| \bar{V}^{\mathrm{eff}}_{k;\mathbf{v}}(Q_k) \right| \phi_k^{v_k;(\mathbf{v})}(Q_k) \right\rangle = 0. \end{aligned} \tag{4.34}$$

This statement is known as a generalized Brillouin theorem [105].

The current implementation makes no assumption about the modal wave functions $\phi_i^{u_i;\mathbf{v}}$ which are used to construct CSFs. The number of these CSFs, however, grows very rapidly with the number of such modal functions, therefore some constraints can be imposed to make calculations feasible. Thus, in typical calculations the maximal excitation level from the reference state, $|u_i - v_i|$, remains fixed to the certain level $u_{\max}$. At the meantime, the number of non-zero matrix elements increases significantly with the maximal order of coupling terms. Thus, within the pairwise approximation all matrix elements between the states which differ in more than two orbitals can be ignored. However, it is not the case when 3-D coupling terms are taken into consideration, that additionally requires to account all CSFs which are different in three modal wave functions. This leads to a situation when the constructed VCI Hamiltonian matrix does not fit into the fast computer memory (RAM). As each matrix element requires some amount of time to be computed, straightforward usage of direct-diagonalisation approaches, which evaluate matrix elements on demand does not seem possible. In order to avoid this memory limitation, the precomputed matrix elements are stored in 1-D array along with their indices in the VCI matrix. This approach allows to keep only significant elements which is greater than a specified threshold $H^{\min}$. If however, the number of elements that have to be stored still does not fit to the available RAM, the new matrix elements replace the least significant ones which are less than a "maximal" threshold $H^{\max}$. In the most unfortunate case, when all residual matrix elements still cannot be resided in the main memory,

PVSCF will dump the Hamiltonian matrix on disk keeping in RAM the indices of the elements and will use the disk as a scratch space.

Finally, in order to make the diagonalisation of such sparse matrices possible, the direct Davidson diagonalisation approach described in details in Ref. [88] was modified. Thus, instead of recalculation of each matrix element $H_{\mathbf{uw}}$ on the fly, these elements are retrieved from the sparse storage. In order to increase access speed, all matrix elements are sorted in ascending order of their indices, and a fast search algorithm is used to locate the particular element by their index. Besides, if the scratch space is used, the index array is still kept in the main memory that makes possible direct retrieval of the matrix element from the scratch space without reading the entire data.

4.4.1 Complete potential: Water molecule

In order to validate the general implementation of the VSCF/VCI method, I used it to compute fundamental transition frequencies of a water molecule in the gas phase. The water molecule has three vibrational normal modes: HOH bending mode (δ(HOH)), symmetric (ν_{s}(OH)) and asymmetric (ν_{a}(OH)) OH stretching modes. Because the correlation potential contains terms up to the 3rd order, it is possible to construct the full PES and to account for all existing coupling terms. The PES was constructed in normal mode coordinates using CCSD(T) *ab initio* electronic structure method with Dunning's correlation consistent basis sets (cc-pVnZ, n=T,Q) [106]. The augmented version of the latter basis set (aug-cc-pVQZ) was also tested in order to approach the experimental data. The PES was computed on a uniform grid with 16 points along each normal mode (4912 points in total) and then interpolated on a uniform grid with 64 points using the Shepard (3) interpolation method. Table 4.3 contains deviations of obtained VCI transition frequencies from the experimental data. For each basis set two sets of frequencies are presented. The first one was obtained using the pairwise approximation (2-D) when only the diagonal and the pair-coupling terms in the PES expansion were taken into account. Alternatively,

Table 4.3. Deviations of VCI fundamental frequencies of a water molecule in the gas phase from the experimental data within pairwise approximation (2-D) and using the complete PES. The PES was computed using CCSD(T) *ab initio* level with cc-pVTZ, cc-pVQZ, and aug-cc-pVQZ basis sets. Eigenvalues are given in cm^{-1}.

mode	cc-pVTZ		cc-pVQZ		aug-cc-pVQZ		Exp.[107]
	2-D	3-D	2-D	3-D	2-D	3-D	
δ(HOH)	7	9	-5	-2	-14	-11	1595
ν_s(OH)	1	9	2	11	-10	2	3657
ν_a(OH)	-31	-11	-26	-6	-36	-14	3756
RMSD	18	10	15	7	23	10	—

fundamental transition frequencies were also computed using the full correlation potential (3-D).

The pairwise approximation significantly underestimates the vibrational frequency of the asymmetric OH stretching mode. Thus, this underestimation is equal to 31 cm^{-1} for the cc-pVTZ basis set, slightly decreases to 26 cm^{-1} for the cc-pVQZ basis set and becomes even larger for the largest basis (aug-cc-pVQZ). The frequencies of two remaining normal modes approach the experimentally observed values and slightly deviate with the basis set used.

In contrast, taking into account the 3-D coupling term significantly improves the most problematic ν_a(OH) mode. Thus, for all tested basis sets the difference between the theoretical and experimental frequencies lies within 14 cm^{-1} interval. At the same time, the frequency of the symmetric stretching mode obtained using cc-pVTZ and cc-pVQZ basis sets within the pairwise approximation accidentally matches the experimental data, while the inclusion of the 3-D coupling increases this frequency by 8 cm^{-1} and 9 cm^{-1} respectively. In case of the aug-cc-pVQZ basis set the reversed trend is observed: the frequency computed within the pairwise approximation is underestimated by 10 cm^{-1}, while the 3-D coupling increases it by 8 cm^{-1} approaching to the experimental value.

Summarizing, the RMSD shows the improvement of transition frequencies for 3-D PES with the basis set size. Probably, the further expansion of the basis set till aug-cc-pV5Z could lead to even better agreement.

Chapter 5

Acetylene on a Cu(001) surface

5.1 Introduction

The adsorption of acetylene on a transition metal surfaces has attracted the attention of researchers for some time [108–110]. The majority of metallic surfaces enhance the reactivity of an adsorbed acetylene molecule by distortion of its geometry. This activates the triple C−C bond and makes it more accessible for combination and polymerization reactions. For example, platinum and palladium surfaces are well known catalysts of the hydrogenation reaction of an adsorbed acetylene [111, 112]. A Pd(111) surface can also involve acetylene into a cyclotrimerization reaction to form benzene [113, 114]. Moreover, metallic copper can lead not only to this trimerization reaction [115], but also to a polymerization reaction to form cuprene [116].

This chapter is focused on vibrational properties of an acetylene molecule chemisorbed on a Cu(001) surface. The choice of the test system was governed by the large amount of information discovered in previous experimental [117–122] and theoretical [123–129] studies. Thus, using scanning tunnelling microscopy (STM) Stipe et al. [117] established that an adsorbed acetylene molecule resides on the fourfold hollow site of the surface (μ_4, see figure 5.1) and parallel to the [110] direction. This resolves a controversy about a preferable adsorption site, as various theoretical

Reprinted in part with permission from **S. K. Chulkov** and D. M. Benoit, "A fragment method for systematic improvement of anharmonic adsorbate vibrational frequencies: Acetylene on Cu(001)", *J. Chem. Phys.*, **139**, 214704 (2013). Copyright 2013, AIP Publishing LLC.

Figure 5.1. Theoretical adsorption sites of a C_2H_2 molecule on a Cu(001) surface reported in the literature: threefold hollow site (μ_3) [124], diagonal (μ_4) [125] and aligned ($\mu_4^{||}$) [123] fourfold hollow sites. According to the STM image [117], the correct adsorption site is μ_4.

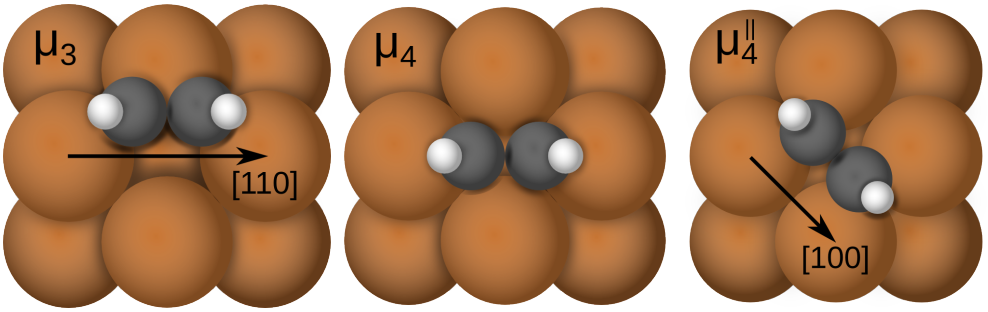

models predicts different sites. Thus, gas-phase DFT simulations of an acetylene molecule on top of a cluster constructed from 17 copper atoms using Becke's exchange [130] and Lee-Yang-Parr correlation [131] functionals (BLYP) and a double zeta basis set predicts that the aligned fourfold site ($\mu_4^{||}$) is the preferable one [123]. Alternatively, the analysis of an ultraviolet photoelectron spectrum (UPS) [124] shows that the adsorption is driven by electron donation from the highest occupied molecular orbital (HOMO) π of an acetylene molecule to a d orbital of copper which are very close in energy. This d orbital, however, interacts with acetylene's lowest unoccupied molecular orbital (LUMO) π^* through a back-donation mechanism [132] that requires an overlap between the anti-bonding π^* orbital and metallic d orbitals. Therefore, an acetylene molecule should be oriented along the [110] direction on the Cu(001) surface in order to maximize this overlapping. This proposed binding mechanism is in very good agreement with the STM image. However, in the original paper [124] Geurts and Avoird suggested an alternative 3-fold hollow site (μ_3) as a preferable one where an C_2H_2 molecule is equidistant from three copper atoms and parallel to the [110] direction. This conclusion was based on the calculation of orbital energy levels of an adsorbed acetylene molecule for various adsorption sites using the Hartree-Fock *ab initio* approach and a cluster model. The orbital energies obtained were then compared with the available UPS spectrum [120] and the adsorption site that gave the best agreement with this spectrum was declared as the preferred one. The subsequent theoretical simulations which were carried out

using periodic DFT approach [125, 133] demonstrate an enhanced contribution from the π^* back-donation stage and predict the μ_4 adsorption site. Moreover, the optimal geometry obtained using DFT-based approaches is in agreement with the surface extended X-ray adsorption fine structure (SEXAFS) experiment [122] which gives the height between the centre of C−C bond and the closest copper atom equal to 1.30 ± 0.05 Å.

In contrast with an acetylene molecule in the gas phase which has a triple CC bond and a linear structure, the molecule becomes non-linear upon adsorption on a Cu(001) surface and its point symmetry group reduces from $D_{\infty h}$ down to C_{2v}. At the same time, its C−C distance elongates from 1.20 Å [134] to 1.42 Å [122], that lies between that of ethylene (1.34 ± 0.02 Å [135]) and ethane (1.522 ± 0.002 Å [136], 1.55 ± 0.03 Å [135]) in the gas phase. This elongation is in good agreement with the proposed chemisorption mechanism as promoting of an electron from the acetylene's π HOMO (which binds both carbon atoms together) to its π^* LUMO should reduce the strength of the C−C bond and increase its length.

The fundamental vibrational frequencies of an acetylene molecule adsorbed on a Cu(001) surface are also well studied experimentally. Because the adsorbed acetylene molecule is no longer linear, it has six normal modes which represent intra-molecular vibrations (see Figure 5.2). Among them are symmetric [ν_s(CH)] and antisymmetric [ν_a(CH)] C−H stretching modes, one C−C stretching mode [ν(CC)], symmetric [δ_s(CH)] and antisymmetric [δ_a(CH)] in-plane C − H bending modes, and an out-of-plane antisymmetric C−H bending mode [γ_a(CH)]. The remaining six degrees of freedom (out of 12) of the adsorbed acetylene molecule appear as frustrated vibrations which correspond to translation- and rotation-like motions of the molecule relative to its solid support. The first of them is the frustrated rotation of the acetylene molecule in its own plane [$\rho_\angle(C_2H_2/Cu)$], that is equivalent to the change of the tilt angle. The second mode is the frustrated rotation of the adsorbed molecule in the plane of the surface [$\rho_\perp(C_2H_2/Cu)$], that tends to swap the acetylene molecule between two equivalent μ_4 adsorption sites along the [110] direction and the perpendicular [$1\bar{1}0$] direction. The last frustrated rotation corresponds to a change of dihedral angle

Figure 5.2. Schematic illustration of intra-acetylene and acetylene-copper normal vibrational modes of a C_2H_2 molecule on a Cu(001) surface. The mode notation is: ν – stretch, δ – in-plane bend, γ – out-of-plane bend, ρ – frustrated rotation, τ – frustrated translation. Labels s and a denote symmetric and antisymmetric vibrations about the σ_v plane of symmetry which is perpendicular to the $C-C$ bond. Labels x, y and z mark frustrated translations along the $[1\bar{1}0]$, $[110]$ and $[001]$ directions respectively, while labels $\angle$ and $\perp$ correspond to frustrated rotations in the acetylene's plane (affecting the tilt angle) and about the C_2 rotation axis of the adsorbed molecule (perpendicular to the solid surface).

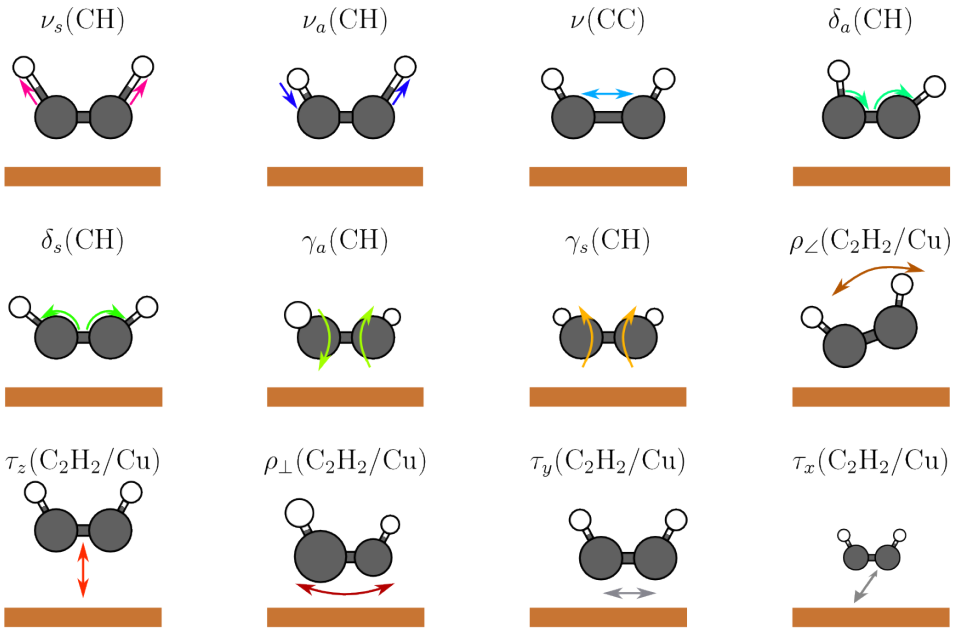

between the acetylene's plane and the solid support, and it is revealed as an out-of-plane symmetric $C-H$ bending mode [γ_s(CH)]. The remained three normal modes are frustrated translations [τ_x(C_2H_2/Cu), τ_y(C_2H_2/Cu), and τ_z(C_2H_2/Cu)] along orthogonal directions (see Figure 5.2). The most interesting one is the τ_z(C_2H_2/Cu) mode which represents the change in the substrate-adsorbate distance.

A high resolution electron energy loss (HREEL) spectrum [137] obtained at 140 K by exposure of clean Cu(100) surface to 2.5×10^{-6} Torr·s of acetylene gas detects almost all of the mentioned vibrations. This spectrum contains four intense peaks. The first one is a very broad peak at 2880 cm^{-1} with a small peak at 2940 cm^{-1} located on its shoulder. Both of these peaks corresponds to CH stretching modes, however a particular symmetry has not been assigned to them. In contrast with the previous two peaks, the strong peak at 1320 cm^{-1} is uniquely assigned to the CC

stretching mode. The remaining two intense peaks at 950 cm^{-1} and 630 cm^{-1} as well as one small peak at 1140 cm^{-1} corresponds to four CH bending modes. However, the available experimental data does not allow us to assign these fundamental transitions to a particular band. Moreover, as the number of these peaks is smaller than the number of CH bending modes, two of these fundamental frequencies probably fall close together giving broad shoulders for one of these peaks. Finally, the HREELS contains a weak broad peak at 420 cm^{-1} corresponding to the $\tau_z(C_2H_2/Cu)$ mode with an unassigned small peak at 340 cm^{-1} on its shoulder.

In addition to HREEL spectrum, Stipe et al. [118] measured the vibration frequency of one CH stretching mode at very low coverage (≈ 0.001 ML) using inelastic electron tunnelling spectroscopy together with scanning tunnelling microscopy (STM–IETS). The obtained value is equal to 2888 cm^{-1} which is in a good agreement with the HREELS data. This band has been lately assigned to be the antisymmetric CH stretch on basis of STM-IETS spectra for various acetylene isotopomers [138].

Several attempts to interpret these spectra using non-empirical quantum chemical calculation were recently made in the literature [125, 133]. Most of them were carried out using the periodic DFT within the harmonic approximation only, because the obtained harmonic frequencies were in a good agreement with the reference experimental data. However, anharmonic effects seem to be very important for this system. In particular, Ulusoy [133] demonstrated that anharmonicity significantly increases the deviation between theoretical and experimental frequencies of CH-stretches, which becomes underestimated by $100 - 200$ cm^{-1} depending on the exchange-correlation (XC) functional used for the construction of the anharmonic PES. This observation suggests that the close agreement between experimental and harmonic frequencies reported previously is the result of an accidental error cancellation, where the excessive softness of CH bonds is compensated by ignoring anharmonic contributions.

The aim of this chapter is to demonstrate the advantage of the proposed fragment method as a way of improving of the adsorbate vibrational frequencies. The second

aim is to demonstrate a correlation between the accuracy achieved for an isolated molecule and the same adsorbed molecule described at the same level of theory.

5.2 Computational details

Periodic DFT calculations were performed using the QuickStep [139] code (part of the CP2K [140] program version 2.2) with the PBE [68] functional and Goedecker-Teter-Hutter (GTH) pseudopotential parameter sets [141] optimized for PBE. The electronic wave function was described using both atomic-centred Gaussian functions and plane waves [139]. As a Gaussian-type basis set, the molecularly optimized triple-zeta valence basis set with two polarization functions (TZV2P-MOLOPT-GTH) [142] was used for all atoms except copper, for which the shorter range molecularly optimized double-zeta valence basis set with one polarization function (DZVP-MOLOPT-SR-GTH) was used.

The value of plane wave cutoff parameter, which determines the size of the auxiliary plane wave basis set, was chosen based on a convergence criterion. On the one hand, this cutoff value should be as minimal as possible because computational costs raise with the size of the plane wave basis set. On the other hand, it should be large enough to correctly represent electron density. Periodic boundary conditions ensure that all properties have a translational symmetry in three directions which coincide with lattice vectors of a simulated crystal. The lengths of these lattice vectors define the size of a repeating unit cell and have to be known *a priori*. This makes a straightforward geometry optimisation using a gradient-based technique difficult, because the rr(CuCu) distance that has to be optimized is in direct proportion with bulk copper lattice vectors which have to remain fixed. Fortunately, as bulk copper has a face-centred cubic crystal structure, its three lattice vectors are equal to each other. Therefore, this geometrical optimisation can be performed using a series of fast SPE calculations for various values of the lattice parameter, while the optimal r(CuCu) is derived from the value of the lattice parameter that gives the minimal energy.

Figure 5.3. An optimal bulk Cu-Cu distance calculated at PBE and PBE-D3 level of theory with respect to used plain-wave cutoff. MOLOPT-TZV2P-GTH basis set was used. Selected cutoff value is marked by the red point.

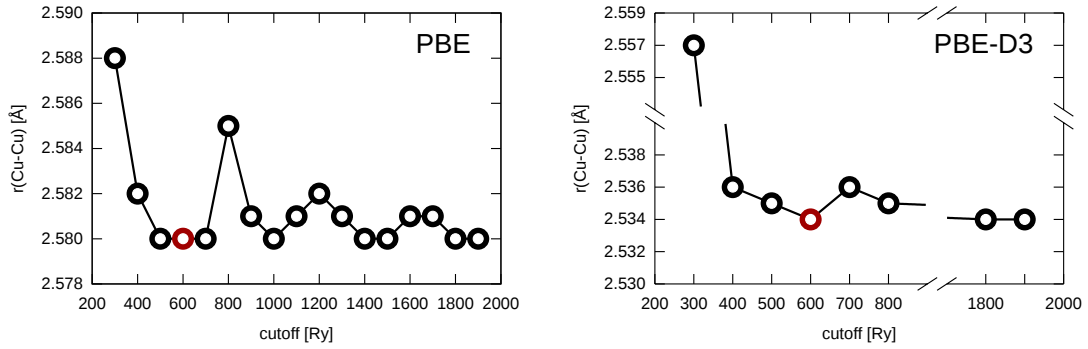

Structural optimisation of bulk copper for various cutoff value was performed using face-centred cubic unit cell with size $(2a \times 2a \times 2a)$ with a lattice parameter $a = \sqrt{2}$ r(Cu-Cu). The cell vector that gave a minimal total energy was considered to be optimal for a particular cutoff value. The dependence of the optimal r(Cu-Cu) distance against the cutoff parameter are illustrated in Figure 5.3. This optimal r(CuCu) distance obtained using the PBE functional decreases monotonically to 2.580 Å with increasing the plane wave cutoff up to 500 Ry, remains unchanged as the cutoff increases up to 700 Ry, and then oscillates within 0.005 Å converging to 2.580 Å at 1800 Ry onwards. At the same time, dispersion correction estimated using Grimme's DFT-D3 scheme [143] decreases this oscillation amplitude down to 0.002 Å. In this case, the optimal r(CuCu) distance asymptotically converges to 2.534 Å accidentally taking this value at 600 Ry. As the 600 Ry plane wave cutoff leads to asymptotic $r(\mathrm{Cu}-\mathrm{Cu})$ length both with and without dispersion correction, I used it for all subsequent periodic DFT calculations which were carried out in this chapter.

The Cu(001) surface was modelled as a slab of six layers of copper atoms using a $(3\sqrt{2} \times 3\sqrt{2})$R45 orthogonal surface unit cell with periodic boundary conditions applied in all directions. The slabs were separated by 25 Å of vacuum along the surface normal direction [001]. The adsorbate coverage was one acetylene molecule per unit cell or 1/9 ML.

In typical surface simulations one or several subsurface metallic layers are kept frozen. These layers are usually frozen in the bulk metal structure in order to avoid rearrangement caused by the vacuum region. However, the optimisation performed shows that the lowest copper layer remained almost flat without imposing any constraints, while the maximum displacement of Cu atoms from the plane did not exceed 0.02 Å. For this reason structure optimisation was performed without any frozen atoms (thus avoiding the necessity of a partial Hessian technique). Moreover the cell vector was varied within certain limits near the value for bulk copper (3.65 ± 0.10 Å) to obtain a minimal energy for the whole acetylene+copper system. Strict convergence criteria were applied during the optimisation process: root mean square (RMS) geometry displacement and gradient were 3×10^{-5} Hartree and 3×10^{-6} Hartree/Bohr correspondingly along with 10^{-7} SCF convergence accuracy.

The adsorption energy was computed as the difference between the obtained optimal energy of the adsorbed system and the sum of the energies of the relaxed Cu(100) surface and optimized acetylene molecule in the gas phase:

$$E_{\text{ads}} = E_e[\text{C}_2\text{H}_2/\text{Cu}(100)] - (E_e[\text{Cu}(100)] + E_e[\text{C}_2\text{H}_2]) \tag{5.1}$$

The Hessian matrix was computed numerically using a two point difference scheme with gradients computed by shifting all atoms by 10^{-2} Bohr along each the x, y, and z axis in both directions. After that, a vibrational analysis was carried out in order to obtain the harmonic frequencies and corresponding normal modes.

The anharmonic PES was constructed in rectilinear normal-mode coordinates. All 1-D and 2-D couplings between 10 adsorbate and adsorbate-lattice vibrations (excluding two in-plane frustrated translational modes $\tau_x(\text{C}_2\text{H}_2/\text{Cu})$ and $\tau_y(\text{C}_2\text{H}_2/\text{Cu})$) were taken into account. The remained two normal modes which correspond to frustrated translations For each normal mode, 14 single point energies (SPEs) for each 1-D curve and 14×14 SPEs for each 2-D coupling were computed (8960 SPEs in total). The frequencies were computed using the VCIPSI method where the number of possible virtual states was limited up to 7 excitation quanta for each normal mode.

Figure 5.4. Schematic representation of the hybrid correction in case of a C_2H_2 molecule on a Cu(001) surface.

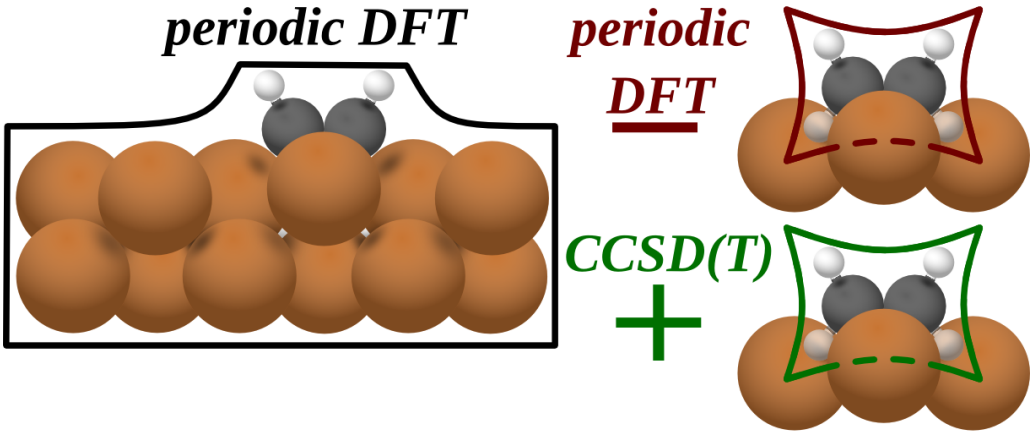

In addition to the periodic DFT, the adsorbed acetylene molecule was also described at CCSD(T) level of theory within our fragment method. At this level Dunning cc-pVTZ [106] was used while the calculation was performed using the GAMESS-US quantum chemical package [89]. The hybrid correction was computed using Eq. (3.21) (see figure 5.4)

Two link atoms were added in a line between carbon and copper atoms, while the exact position was determined using Eq. (3.23). The optimal $|\vec{\mathbf{r}}_{\mathrm{C}} - \vec{\mathbf{r}}_{\mathrm{Cu}}|_{\mathrm{I}}$ distance in the adsorbed system computed at the PBE level is equal to 1.969 Å, while the equilibrium $|\vec{\mathbf{r}}_{\mathrm{C}} - \vec{\mathbf{r}}_{\mathrm{H}}|_{\mathrm{II}}$ distance computed for ethane at CCSD(T) level is equal to 1.080 Å.

5.3 Adsorbate geometry and frequencies

Since vibrational frequencies are sensitive to the adsorbate structure, it is important at the early stage to make certain that the used model adequately represents the actual system. The easiest method to do this is to compare the predicted optimal structure with the results of experimental observation. The structural parameters computed at PBE and PBE-D3 levels of theory are listed in Table 5.1 along with experimental and reference theoretical data. In addition, the computed heat of adsorption is also shown in Table 5.1 and the optimal structure obtained at the PBE level along with the used labels is pictured in Figure 5.5.

Table 5.1. Optimal geometry and adsorption energy of an acetylene molecule on a Cu(001) surface. r(Cu/CC) denotes a distance between the centre of the C−C bond and the copper surface (the distance with respect to the closest side copper atom is given in brackets).

	r(CC),Å	r(CH),Å	r(Cu/CC),Å	α(HCC),°	r(CuCu),Å	E_{ads},eV
Experiment	1.42 [121, 122]	—	1.30 ± 0.05 [122]	—	2.55 [117]	—
PBE [125]	1.37	1.10	1.49	120	2.56*	—
PBE [128]	1.37	1.08	—	120	—	−1.38†
PW91 [144]	1.36	1.10	—	120	2.58	−1.31
PBE	1.37	1.10	1.48 (1.32)	119	2.62	−1.33
PBE-D3	1.37	1.10	1.52 (1.34)	119	2.57	−2.25

* Fixed at the experimental value without optimization.
† The energy of adsorption has not been corrected by the zero-point vibrational energy.

Figure 5.5. Optimized molecular geometry of a C_2H_2 molecule on a Cu(001) surface. Top and side views. The $(3\sqrt{2} \times 3\sqrt{2})$R45 unit cell is outlined with a dash line.

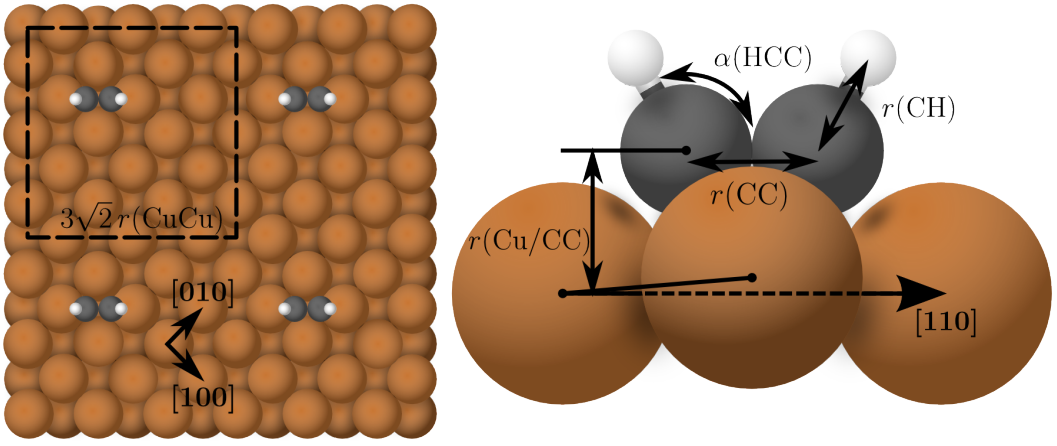

The calculated optimal geometry is consistent with experimental data. The acetylene molecule is found to be 1.48 Å above the Cu(001) surface at its μ_4 adsorption site. Despite the good agreement with an alternative periodic DFT (PBE) study [125] this is higher than observed in the SEXAFS experiment [122]. However, the Cu(001) surface becomes non-planar upon acetylene adsorption, due to vertical displacement (by 0.16 Å) of the closest copper atoms on each side of the C−C bond line. Accordingly, the height between these out-of-plane copper atoms and the centre of the C−C bond is equal to 1.32 Å that falls into the confidence interval of the SEXAFS experiment. The C−C bond length of the adsorbed acetylene molecule is equal to 1.37 Å that is shorter than the corresponding experimental value by 0.05 Å, however it is in a perfect match with other theoretical predictions [125, 128, 144]. The C−H bond length [r(CH)], H−C−C bond angle [α(HCC)], and the adsorption

Table 5.2. Comparison between HREELS and calculated harmonic (ω_0) frequencies for C_2H_2/Cu(001). Vibrational modes along with the corresponding notation are illustrated in Figure 5.2. For simplicity, the labels in brackets are omitted for all adsorbate-substrate modes as well as modes involving C−H bonds. All frequencies (ω_0) are given in cm^{-1} and all relative deviations $\Delta\omega_0$ are in percents.

	ν_s	ν_a	ν(CC)	δ_a	δ_s	γ_a	γ_s	$\rho_\angle$	τ_z	$\rho_\perp$	τ_y	τ_x	RMSD
HREELS [137]	2940	2880	1320	1140	950	—	630	—	420	—	—	—	—
ω_0, PBE	2972	2944	1346	1154	972	932	644	479	423	307	138	123	31
ω_0, PBE-D3	2985	2958	1341	1157	980	931	640	489	429	297	106	92	38
$\Delta\omega_0$, PBE	1.1	2.2	2.0	1.2	2.3	—	2.2	—	0.7	—	—	—	—
$\Delta\omega_0$, PBE-D3	1.5	2.7	1.6	1.5	3.2	—	1.6	—	2.1	—	—	—	—

energy [E_{ads}] are equal to 1.10 Å, 119°, and −1.33 eV respectively. Whereas the corresponding experimental data have not been reported so far, all of these results are also in good agreement with the previous theoretical studies.

The importance of weak van der Waals interaction was reported for adsorption of oxygen on Cu(110) [145]. However, in case of acetylene on Cu(001) this type of interaction does not affect significantly the geometrical parameters of adsorbed molecule. Nevertheless, the dispersion correction slightly increases the r(Cu/CC) height to 1.52 Å with respect to the top metal layer and 1.34 Å with respect to the non-planar Cu atoms. Besides, this correction increases the adsorption energy (up to −2.25 eV) and improves the intra-metallic distances of the Cu surface [rCuCu] from 2.62 Å to 2.57 Å. The obtained r(CuCu) distance is in very good agreement with the STM image of Ref. [117].

Table 5.2 compares the harmonic frequencies with the HREELS frequencies of Ref. [137]. It can be seen that the obtained frequencies lies in close proximity of the experimental peaks, and almost all peaks can be easily assigned. The only one exception is the peak at 950 cm^{-1} which can be assigned either to γ_a(CH) or δ_s(CH) mode. The latter mode, however, is the more preferable alternative because in this case all harmonic frequencies become overestimated relative to their HREELS counterparts. In particular, at the PBE level of theory the harmonic approximation overestimates experimental frequencies on average by 1.7%. The most overestimated modes are ν_a(CH), ν_s(CH), and ν(CC) whose harmonic frequencies differ from the corresponding experimental values by 64 cm^{-1}, 32 cm^{-1}, and 26 cm^{-1} respectively.

Figure 5.6. Contribution to the vibrational frequencies from 1-D and 2-D anharmonic corrections (in % with respect to the corresponding harmonic frequency).

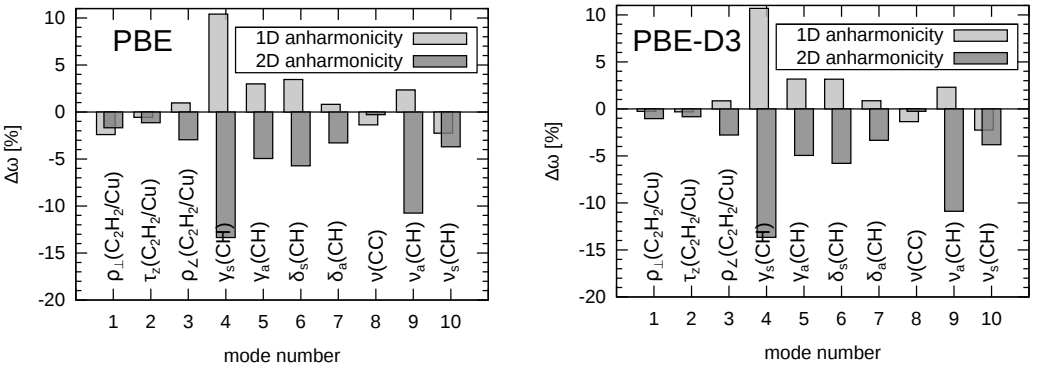

The gap between two C−H stretching modes is 28 cm^{-1} which is two times smaller than the experiment (60 cm^{-1}). The difference in harmonic frequencies of δ_s(CH) and γ_a(CH) bending modes is equal to 40 cm^{-1}. The harmonic frequencies for the other peaks resolved experimentally in HREELS are equal to 644 cm^{-1} and 423 cm^{-1} and correspond to γ_s(CH) and $\nu(C_2H_2/Cu)$ respectively.

The dispersion correction slightly increases the RMSD error (38 cm^{-1} instead of 31 cm^{-1} for the PBE PES). Both ν_s(CH) and ν_a(CH) frequencies increase by $\sim$ 14 cm^{-1}, reaching 2985 cm^{-1} and 2958 cm^{-1} respectively. The gap between them remains constant and amounts to 27 cm^{-1}. Conversely, the difference between δ_s(CH) and γ_a(CH) harmonic transitions with dispersion correction raises slightly to 49 cm^{-1} by virtue of increasing of δ_s(CH) to 980 cm^{-1}, while γ_a(CH) remains constant and is equal to 931 cm^{-1}. The other transition frequencies of acetylene vary but differ from dispersion uncorrected results by no more than 6 cm^{-1}.

It can be seen that the harmonic approximation yields surprisingly accurate frequencies at both PBE and PBE-D3 levels. All frequencies are slightly overestimated, and the dispersion correction increases this overestimation for all modes except ν(CC). However, anharmonicity plays an important role and taking this into consideration leads to drastic changes.

The distribution of the 1-D and 2-D anharmonicity over the vibrational modes is demonstrated in Figure 5.6, while the resulting anharmonic frequencies are given in Table 5.3. It can be seen that the anharmonic effect is the same regardless

Table 5.3. Anharmonic (ν) fundamental transition frequencies for C_2H_2/Cu(001) computed using pairwise approximation (1D+2D) and their relative deviation (in %) from the HREELS data. Vibrational modes along with the corresponding notation are illustrated in Figure 5.2 For simplicity, the labels in brackets are omitted for all adsorbate-substrate modes as well as modes involving C−H bonds. All frequencies (ν) are given in cm^{-1} and all relative deviations $\Delta\nu$ are in percents.

	ν_s	ν_a	ν(CC)	δ_a	δ_s	γ_a	γ_s	$\rho_\angle$	τ_z	$\rho_\perp$	RMSD
HREELS [137]	2940	2880	1320	1140	950	—	630	—	420	—	—
ν, PBE	2795	2697	1324	1126	950	914	625	469	416	295	88
ν, PBE-D3	2804	2704	1319	1128	954	913	621	479	424	293	84
$\Delta\nu$, PBE	-4.9	-6.4	0.3	-1.2	0.0	—	-0.8		-1.0	—	—
$\Delta\nu$, PBE-D3	-4.6	-6.1	-0.1	-1.1	0.4	—	-1.4		1.0	—	—

of the dispersion correction. The contribution from the diagonal anharmonicity mostly affects in-plane and out-of-plane C − H bending modes. Moreover, symmetric bending modes demonstrate a stronger anharmonic nature than their antisymmetric counterparts. Thus, 1D correction increases the harmonic frequencies of γ_s(CH), δ_s(CH), γ_s(CH) by 10.5%, 3.5%, and 3% respectively. At the same time, both ν_a(CH) and ν_s(CH) frequencies changes by 2.3% but in opposite directions while the 1-D anharmonic effect for other modes (except frustrated rotation) does not exceed 1.5%. While 1-D anharmonicity tends to increase frequencies, 2-D anharmonic corrections decrease them. Again, the most affected modes are CH stretching and bending modes, especially γ_s(CH) (−10.8%) and ν_a(CH) (−3.7%) ones. Occasionally, for almost all modes (including γ_s(CH) mode) 1-D and 2-D contributions compensate each other. At the same time, the sum of 1-D and 2-D contributions for ν_a(CH) and ν_s(CH) modes are very high and lead to a significant underestimation of these modes with respect to the experimental data by -6.4 cm^{-1} and -4.9 cm^{-1} respectively. This causes an increased RMSD error (88 cm^{-1} for PBE PES and 84 cm^{-1} for PBE-D3 PES). This behaviour allows to conclude that the agreement of the harmonic frequencies with the experimentally observed data is caused by an accidental error cancellation, as a consequence of compensation of the DFT PES deficiencies by neglecting anharmonicity.

Table 5.4. The relative deviation of computed harmonic ($\Delta\omega_0$) and anharmonic ($\Delta\nu$) frequencies of C_2H_2 in the gas phase with respect to experimental data. PBE PES was computed using MOLOPT-TZV2P-GTH basis set, while CCSD(T) PES was computed using cc-pVTZ basis set. The mode assignment convention is: ν – stretching mode, δ – bending mode. Labels s and a mark symmetric and asymmetric vibration. RMSD value counts the error from bending modes twice (7 modes in total), as these modes are doubly degenerate. All values are given in cm^{-1}

	ν_s(CH)	ν_a(CH)	ν(CC)	δ_a(CH)	δ_s(CH)	RMSD)
Experiment [146–149]	3373	3295	1974	731	613	—
$\Delta\omega_0$, PBE	68	49	22	10	-16	34
$\Delta\nu$, PBE / 2-D	-81	-160	-16	-5	-24	69
$\Delta\omega_0$, CCSD(T)	138	115	27	15	-35	72
$\Delta\nu$, CCSD(T) / 2-D	-18	-105	-18	-3	-36	45
$\Delta\nu$, CCSD(T) / 3-D	-13	-20	-11	11	-15	14
$\Delta\nu$, CCSD(T) / 4-D	3	-11	-10	-4	-29	17

5.4 Acetylene molecule in the gas phase

The accidental error cancellation mentioned in the previous section is not specific to the adsorbed system under consideration. It also takes place for an acetylene molecule in the gas phase computed at the PBE level of theory. In order to demonstrate the strength of this effect, the fundamental vibrational frequencies have been computed within the harmonic approximation using PBE and CCSD(T) PESs. Besides, the role of anharmonicity has also been studied at the different level of approximations.

The results are summarised in Table 5.4. As for the adsorbed acetylene, the harmonic frequencies computed for an acetylene molecule in the gas phase at the PBE level of theory are in good agreement with the experimental data. Thus, the harmonic frequencies for symmetric [δ_s(CH)] and antisymmetric [δ_a(CH)] $C-H$ bending modes differ from the corresponding experimental values by no more than 16 cm^{-1}. The frequency of the $C-C$ stretching mode is slightly overestimated (by 20 cm^{-1}). The mostly overestimated modes are symmetric (68 cm^{-1}) and antisymmetric (49 cm^{-1}) $C-H$ stretches which are the main contributors to the overall error.

Note that the achieved accuracy (RMSD = 34 cm^{-1}) is very close to that obtained for the adsorbed acetylene on Cu(001) (RMSD = 31 cm^{-1}). Moreover, this agreement is also caused by the accidental error cancellation. Thus, the anharmonic correction computed using PBE PES within a pairwise approximation (2-D) leads to dramatically

underestimated CH stretching modes. The ν_a(CH) frequency is underestimated by 160 cm^{-1} which is very close to that of the adsorbed molecule (190 cm^{-1}). The absolute underestimation of ν_s(CH) frequency (81 cm^{-1}) is two times smaller that the corresponding underestimation in the case of adsorbed acetylene (145 cm^{-1}). However, in both cases the relative values of the blue shifts caused by anharmonic effects are comparable to each other (149 cm^{-1} vs. 177 cm^{-1} respectively).

In contrast with the PBE PES, at the CCSD(T) level of theory the difference between the calculated fundamental transition frequencies and the experimental ones increases slightly for ν(CC) (27 cm^{-1}) and δ_a(CC) (15 cm^{-1}) modes. The δ_s(CH) modes remains underestimated by 35 cm^{-1}, while the harmonic frequencies of both CH stretching modes are overestimated drastically by 138 cm^{-1} and 115 cm^{-1} for the ν_s(CH) and ν_a(CH) respectively. At the same time within the pairwise approximation all frequency are underestimated. The most anharmonic modes are ν_s(CH) and ν_a(CH) which are shifted downward by 158 cm^{-1}and 220 cm^{-1} respectively in comparison with the harmonic frequencies. The pairwise approximation significantly improves the accuracy of the description (RMSD = 45 cm^{-1}). Moreover, higher-order couplings lead to further improvement and approaches the experimentally observed frequencies. Thus, taking into account 3-D reduce RMSD error down to 14 cm^{-1} by improving the description the most problematic ν_a(CH) and δ_s(CH) modes. At the same time, 4-D coupling terms lead to further improvement of (CH) stretching modes at the cost of additional underestimation of the δ_s(CH) frequency. In case of 4-D PES, the achieved RMSD value is equal to 17 cm^{-1}, however with the exception of δ_s(CH) the frequency deviation from the experimental data in this case does not exceed 11 cm^{-1}.

Note that for acetylene in the gas phase, using the CCSD(T) PES instead of the PBE PES gives more accurate anharmonic frequencies within the pairwise approximation. However, within the harmonic approximation the PBE PES gives a better agreement with the experimental data. As for the adsorbed molecule, this improved agreement is the result of accidental error cancellation, that allows us to expect significant improvement of the anharmonic adsorbate frequencies within the

Figure 5.7. The relative deviation (in cm^{-1}) of the anharmonic frequencies from the experimental data. (a) PBE PES and PBE|CCSD(T) PES; (b) PBE-D3 PES and PBE-D3|CCSD(T) PES. The deviation for the γ_a(CH) frequency computed in assumption that modes γ_a(CH) and δ_s(CH) are degenerate.

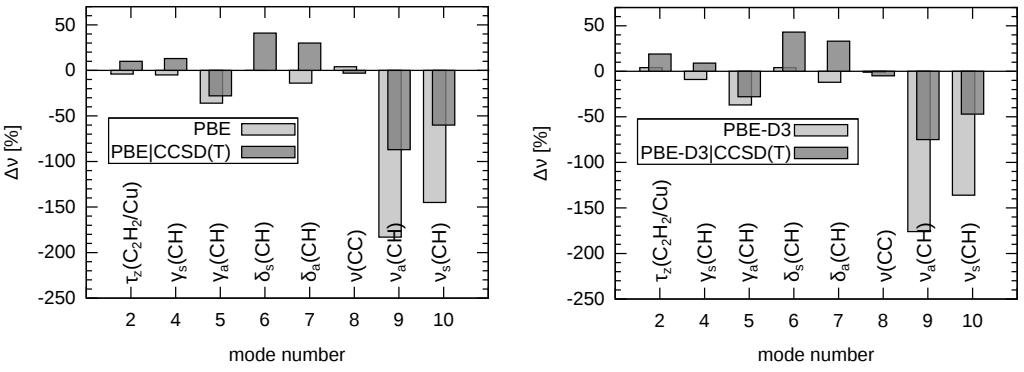

Table 5.5. Anharmonic (ν) fundamental transition frequencies for C_2H_2/Cu(001) calculated using a hybrid PBE|CCSD(T) PES. Vibrational modes along with the corresponding notation are illustrated in Figure 5.2 For simplicity, the labels in brackets are omitted for all adsorbate-substrate modes as well as modes involving C−H bonds. All values are in cm^{-1}.

	ν_s	ν_a	ν(CC)	δ_a	δ_s	γ_a	γ_s	$\rho_\angle$	τ_z	$\rho_\perp$	RMSD
HREELS [137]	2940	2880	1320	1140	950	—	630	—	420	—	—
ν, PBE|CCSD(T)	2880	2793	1317	1170	991	922	643	496	430	309	45
ν, PBE-D3|CCSD(T)	2893	2805	1315	1173	993	922	639	506	439	308	40

fragment method.

5.5 Hybrid correction

The anharmonic frequencies computed within the fragment method using PBE|CCSD(T) and PBE-D3|CCSD(T) hybrid PES are listed in Table 5.5. The relative deviations of these frequencies from experimental data were plotted in Figure 5.7 along with the similar deviation of uncorrected PBE frequencies. It can be seen, that the hybrid PES significantly improves the anharmonic frequencies of the C − H stretching modes. In comparison with the PBE PES, the frequency deviation for the most problematic ν_a(CH) decreases by a factor of two (from -183 cm^{-1} to -87 cm^{-1}). The same is also valid for the ν_s(CH) mode, which also demonstrates an excellent improvement (from -145 cm^{-1} to -60 cm^{-1}). The fragment method slightly alters the predicted ν(CC) stretching frequency which closely approaches the experimental data ($\Delta\omega =$

Figure 5.8. 2-D coupling map between normal modes of acetylene on a Cu(001) surface computed using hybrid PBE|CCSD(T) PES. $C-H$ stretching modes are strongly coupled with themselves as well as with all $C-H$ bending modes. The first three modes which correspond to frustrated rotations and frustrated translations are almost decoupled with the intra-acetylene vibrations.

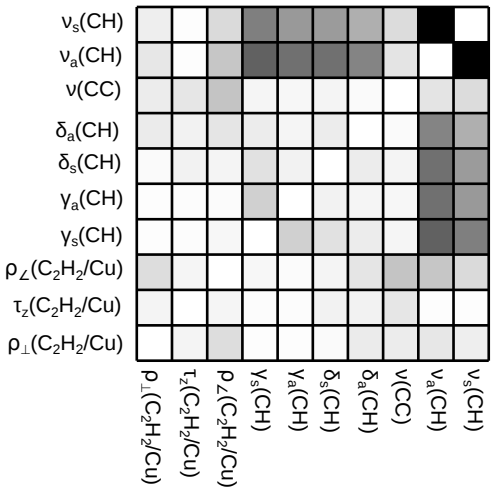

-3 cm^{-1}). At the same time, the $\tau_z(C_2H_2/Cu)$ and $\gamma_s(CH)$ modes becomes slightly overestimated (by 10 cm^{-1} and 13 cm^{-1} respectively) while with no hybrid correction they are underestimated by 4 cm^{-1} and 5 cm^{-1}. The fragment method describes $\delta_a(CH)$ and $\delta_s(CH)$ modes less accurate ($\Delta\omega = 30$ cm^{-1} and 41 cm^{-1} respectively) in comparison with the PBE PES. However in later case the experimental peak at 950 cm^{-1} may be assigned to the $\gamma_a(CH)$ mode which demonstrate improvement from -36 cm^{-1} to -28 cm^{-1}. The dispersion correction slightly improves the RMSD error (from 45 to 40 cm^{-1}), raising CH stretches as well as $\tau_z(C_2H_2/Cu)$ by ~ 10 cm^{-1} but keeping the most problematic CH stretch modes drastically underestimated.

Nevertheless, in comparison with uncorrected results, the fragment method allows to nearly double the accuracy. Thus, it reduces the RMSD error by 43 cm^{-1} (by 44 cm^{-1} with the dispersion correction). Moreover, comparison between the obtained hybrid results and anharmonic frequencies for the free molecule in gas phase computed within the pairwise approximation shows that the RMSD values in both cases are almost identical (~ 45 cm^{-1}). That means that for a suitable description of the periodic surface, the accuracy of the fragment method is limited by the accuracy of *ab initio* method used for the adsorbate. For this reason, 3-D coupling terms should

lead to further improvement of the anharmonic frequencies of the adsorbate.

This is supported by a coupling map computed at the hybrid PBE|CCSD(T) level (see Figure 5.8). It can be seen that all rotational modes are strongly coupled with translational modes which involves the same group of atoms (C − H). The large number of such couplings usually highlights their artificial nature. Such couplings are usually strong in rectilinear normal-mode coordinates, and often can be vanished using coordinates described in section 2.7. Unfortunately, at this stage, curvilinear coordinates have not been implemented in PVSCF for periodic systems. Alternatively, expanding PES up to the 3-D is very time consuming; thus taking into account 3-D couplings even between the six strongly coupled modes would require over 50,000 SPEs. Nevertheless, the accuracy that has already been achieved within the fragment method demonstrates significant improvements against uncorrected data.

Chapter 6

Thiophene on a Au(111) surface

Thiophene is a building block of a class of substances called oligothiophenes and also the monomer unit of polythiophenes. Since their discovery in the 1970s, polythiophenes have applications as materials for light-emission diodes [150], field-effect transistors [151, 152], polymer electrodes [153], and in many other areas [154]. Oligothiophenes are also very promising materials for molecular electronic and solar cells [155]. In addition they have a tendency to form a regular structure – self-assembled monolayers (SAM) [156] – on many transition metal surfaces [157, 158] that allows to vary properties of such surfaces over wide range [159]. In this respect, the adsorption of thiophene on transition metals as a prototype of such materials attracts the attention of researchers.

In particular, the adsorption of thiophene on Au(111) was extensively studied using a variety of experimental techniques, such as scanning tunnelling microscopy (STM) [160, 161], near edge X-ray adsorption fine structure (NEXAFS) [162], and infrared reflection absorption spectroscopy (IRRAS) [163]. It was found that on a Au(111) surface a thiophene molecule prefers on-top adsorption site, but the orientation of the ring is different at different coverage. Thus, according to an STM image [161], at low coverage the molecule lies almost parallel to the surface with a small tilt angle. This tilt angle increases with the coverage, leading to a vertical orientation for a coverage of about one molecule per three gold atoms. This observation is in good agreement with a NEXAFS experiment [162] where this effect

was also observed.

The adsorption of thiophene and several oligothiophenes on Au(111) surface was also studied using vibrational spectroscopy. Thus, the vibrational spectra of the terthiophene (3T) was measured using IRRAS [163], SERS [164] and STM-IETS [165] techniques which allowed to detect over 30 fundamental transitions. However, despite its importance, no detailed spectrum was reported for thiophene adsorbed on a Au(111) surface. In this chapter, a theoretical spectrum of thiophene on a Au(111) surface obtained using the fragmentation method is presented. In addition, a mode assignment of 3T on Au(111) surface is given based on the theoretical spectra of 3T in the gas phase.

6.1 Thiophene in the gas phase

The aim of this section is to discuss an influence of the quality of the used PES on the anharmonic frequencies using a thiophene molecule in the gas phase as a test molecular system. For this purpose, the structure was optimization using three different levels of theory. Then, the Hessian matrix and all diagonal- (1-D) and pair-couplings (2-D) were constructed for each of these levels.

The first PES was computed using periodic DFT approach with the PBE exchange-correlation functional [68]. This functional is widely used in the literature for metallic surfaces and adsorbed systems [166, 167], and for this reason it has to be tested. At this level of theory, calculations were performed using the CP2K (ver. 2.2) program [140]. The unit cell size was $10 \times 10 \times 14$ Å^3 with periodic boundary conditions applied in all three directions. The TZV2P-MOLOPT-GTH basis set [142] was used for all valence electrons, while core electrons were described using Goedecker-Teter-Hutter (GTH) pseudo-potentials [141] optimized for the PBE functional. In addition, a basis of plane waves with a plane wave cutoff of 400 Ry was used within a Gaussian and plane wave scheme (GPW) [139].

The second PES was computed using the B3LYP functional [69] which is used often for organic compounds. At this level, the calculation was carried out using

Figure 6.1. The structure of a thiophene molecule in the gas phase

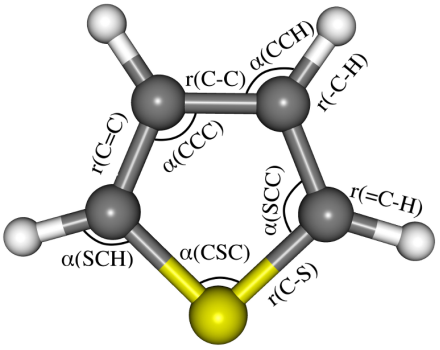

Table 6.1. Calculated and experimental molecular geometries of thiophene in the gas phase. Uncertainties are given with respect to the last digits, for example, 1.7140(14) means 1.7140±0.0014.[1]

	Absolute values			Δ,%			
	B3LYP	PBE	CCSD(T)	B3LYP	PBE	CCSD(T)	Experiment [170]
r(C–S), Å	1.728	1.712	1.722	0.8	-0.1	0.5	1.7140(14)
r(C–C), Å	1.424	1.424	1.429	0.1	0.1	0.4	1.4232(23)
r(C=C), Å	1.364	1.376	1.372	-0.4	0.5	0.2	1.3696(17)
r(–C–H), Å	1.080	1.088	1.081	-0.1	0.7	0.1	1.0805(14)
r(=C–H), Å	1.077	1.085	1.078	-0.1	0.7	0.0	1.0776(15)
α(CSC), °	91.6	92.2	91.9	-0.6	0.0	-0.3	92.17(10)
α(SCC), °	111.5	111.4	111.7	0.0	-0.1	0.2	111.47(23)
α(CCC), °	112.7	112.5	112.4	0.2	0.0	0.0	112.45(18)
α(SCH), °	120.1	120.0	120.2	0.2	0.1	0.3	119.85(78)
α(CCH), °	124.0	124.2	123.4	-0.2	-0.1	-0.7	124.27(7)
RMSD, 10^{-3} Å	6.8	5.6	4.6	0.3	0.4	0.2	MARE (r), %
RMSD, °	0.3	0.1	0.4	0.2	0.1	0.3	MARE (α), %

[1] Reprinted in part with permission from D. M. Benoit, B. Madebene, I. Ulusoy, L. Mancera, Y. Scribano, and **S. Chulkov**, "Towards a scalable and accurate quantum approach for describing vibrations of molecule–metal interfaces", *Beilstein J. Nanotechnol.*, **2**, 427–447 (2011). Copyright 2011, Beilstein Institut.

the GAMESS-US (ver. 1 OCT 2010 (R1)) program [89] along with TZV-2P basis set [168, 169] Finally, a reference PES was constructed at the coupled-cluster singles, doubles and perturbative triples (CCSD(T)) level of theory along with Dunning's correlation consistent triple zeta basis sets (cc-pVTZ) [106]. This calculations was also performed using the GAMESS-US program.

Figure 6.1 shows the structure of a thiophene molecule in the gas phase, while its optimal structural parameters computed at three different levels of theory are listed in Table 6.1. In all three cases the predicted molecular geometry are in good agreement with experimental data, while deviations do not show any regular pattern. Both

B3LYP and CCSD(T) methods overestimate the C–S internuclear distance by 0.8% and 0.5% respectively, while the PBE functional gives a value within experimental accuracy (0.1%). The CCSD(T) method also overestimates the r(C–C) length by 0.4%, while B3LYP and PBE functionals reproduce the experimental value. However, for the double C=C bond the situation is reversed: the least accurate results are those obtained using PBE (0.5%) and B3LYP (-0.4%) levels of theory which are two times larger than those of CCSD(T) (0.2%). In contrast with internuclear distances, almost all predicted values of linear angles lies within the experimental confidential interval. The only exception is two angles α(CSC) and α(CCH) which are both slightly underestimated at B3LYP and CCSD(T) levels.

Despite of the fact that all three electronic structure methods predict similar structure parameters, the difference of their potential energy surfaces (PES) is significant. Thus, this difference has an impact on the computed vibrational frequencies even at the harmonic level. These harmonic frequencies are presented in Table 6.2. Thus, the CCSD(T) method gives reliable results for all low-frequency and middle-frequency modes. The deviation from the experimental data for most of them does not exceed 2% with the exception of one out-of-plane CH bending mode [γ(CH)], one in-plane CH bending mode [δ(CH)], and two CC bending modes [$\nu(\mathrm{C-C})$ and $\nu(\mathrm{C=C})$] whose accuracy lies within a 2-3% interval. At the same time, $\mathrm{C-H}$ stretches [ν(CH)] are significantly overestimated (by more than 4% or 130 cm^{-1}) which is mainly caused neglecting anharmonicity.

At the B3LYP level of theory the harmonic frequencies demonstrates the same tendency. Thus, all ν(CH) and δ(CH) modes are overestimated in average by 4% and 2% respectively. However, in contrast to the CCSD(T) level, the error for torsional modes [γ(CCSC) and γ(CCCC)] and one γ(CH) mode (Nr. 10) exceeds 2%.

In contrast to the CCSD(T) and B3LYP levels, the PBE functional gives surprisingly "accurate" harmonic frequencies for CH stretching modes. Thus, the deviation from the experimental values for these modes does not exceed 1.8% or 59 cm^{-1}. Moreover, the frequencies of all δ(CH) modes are underestimated by a similar value (up to 1.7%) while CCSD(T) and B3LYP methods overestimate them. This leads to a

Table 6.2. Harmonic frequencies ω_0 of thiophene in the gas phase and their relative deviations from the experiment $\Delta\omega$. The mode assignment convention is: ν – stretching, δ – in-plane bending, γ – out-of-plane bending. The symmetry labels denote irreducible symmetry representation in C_{2v}. All harmonic frequencies are given in cm^{-1} and the deviations are given in percents.

Mode number	Sym.	Assignment	PBE		B3LYP		CCSD(T)		Experiment[171]
			ω_0	$\Delta\omega$	ω_0	$\Delta\omega$	ω_0	$\Delta\omega$	
1	B_1	γ(CCSC)	466	3.1	461	2.0	453	0.2	452
2	A_2	γ(CCCC)	571	1.2	581	3.0	566	0.4	564
3	A_1	δ(CSC), ν(SC)	607	-0.3	612	0.5	610	0.2	609
4	A_2	γ(CH)	643	-5.9	688	0.7	688	0.7	683
5	B_1	γ(CH)	691	-2.9	722	1.4	726	2.0	712
6	B_2	δ(CCC), ν(SC)	749	-0.7	743	-1.5	759	0.7	754
7	A_1	δ(CCC), ν(SC)	828	-1.4	833	-0.8	846	0.7	840
8	B_1	γ(CH)	830	-4.2	878	1.4	876	1.2	866
9	B_2	δ(SCC), ν(SC)	856	-1.9	882	1.0	878	0.6	873
10	A_2	γ(CH)	872	-3.1	920	2.2	903	0.3	900
11	A_1	γ(ring)	1035	-0.1	1053	1.6	1052	1.5	1036
12	A_1	δ(CH)	1066	-1.5	1107	2.3	1098	1.5	1082
13	B_2	δ(CH)	1069	-1.5	1107	2.0	1101	1.5	1085
14	B_2	δ(CH)	1235	-1.7	1284	2.2	1279	1.8	1256
15	A_1	δ(CH)	1352	-0.9	1398	2.5	1396	2.3	1364
16	A_1	ν(C − C)	1409	-0.1	1441	2.2	1443	2.3	1410
17	B_2	ν(C = C)	1499	-0.7	1550	2.6	1545	2.3	1510
18	B_2	ν(CH)	3130	1.4	3201	3.7	3214	4.1	3087
19	A_1	ν(CH)	3144	1.5	3214	3.8	3228	4.2	3097
20	B_2	ν(CH)	3179	1.7	3252	4.1	3256	4.2	3125
21	A_1	ν(CH)	3181	1.8	3254	4.1	3259	4.3	3126
		RMSD	28		56		59		—

small RMSD error (22 cm^{-1}) at the PBE level, while in case of B3LYP and CCSD(T) this error is significantly higher and equal to 56 cm^{-1} and 58 cm^{-1} respectively. At the same time, at the harmonic level, PBE significantly overestimates the frequencies of torsional modes (up to 3%) and overestimates all γ(CH) frequencies by 3–6%.

This pattern can be explained by an accidental error cancellation at the PBE level, while B3LYP and CCSD(T) methods overestimate the frequencies at the harmonic level due to the lack of anharmonicity. This is apparent during comparison of relative deviations between the PBE and the reference CCSD(T) harmonic frequencies (see Figure 6.2). Thus, almost all PBE frequencies are constantly underestimated by 2–3%, while for all γ(CH) modes the deviation is even higher and lies within 5–7% interval. As this deviation is caused by the PES inaccuracy, the corresponding

Figure 6.2. Relative deviation (in %) of PBE and B3LYP harmonic frequencies of thiophene in the gas phase from the corresponding harmonic frequencies obtained using CCSD(T) PES. Two torsional modes γ(CCSC) and γ(CCCC) are labelled as γ(ring).

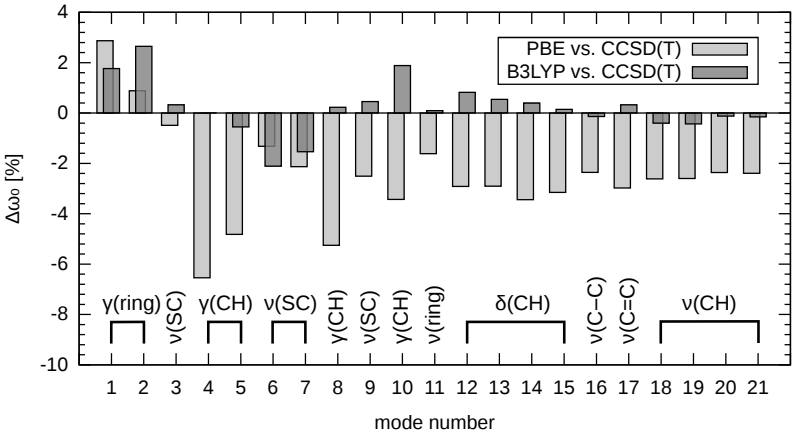

anharmonic frequencies should also be underestimated. At the same time, comparison between the B3LYP and CCSD(T) harmonic frequencies (see figure 6.2) demonstrate a problem in the description of the torsional modes, two ν(SC) modes (Nr. 6 and Nr. 7), and one γ(CH) mode (Nr. 10). For all of these modes the relative error is about 3%.

Going beyond the harmonic approximation, VCIPSI anharmonic frequencies were computed at each level of theory both in rectilinear and curvilinear coordinates. The curvilinear coordinates were defined through a set of inter-atomic distances, angles and dihedral angles. All calculations were performed within the pairwise approximation where all pair-couplings were taken into account. The relative deviations of the VCIPSI anharmonic frequencies from the experimental data for different PES-s are shown in Figure 6.3, while the absolute values are given in Table 6.3. The best agreement with the experimental data is achieved for the CCSD(T) PES. In this case, the RMSD error is equal to 21 cm^{-1} and to 9 cm^{-1} for the PES expressed in rectilinear and curvilinear coordinates respectively. It can be seen, that in case of the CCSD(T) PES, the rectilinear coordinates are a very good choice. The main contribution to this error comes from the $C-H$ stretching mode [ν(CH)] (Nr. 20) whose frequency is underestimated by 2% as well as from two bending [γ(CH)] modes (Nr. 5 and Nr. 8) whose frequencies differ from the experimental data by 5% and

Figure 6.3. Relative deviation of anharmonic frequencies (VCIPSI) of thiophene in the gas phase from experimental data.

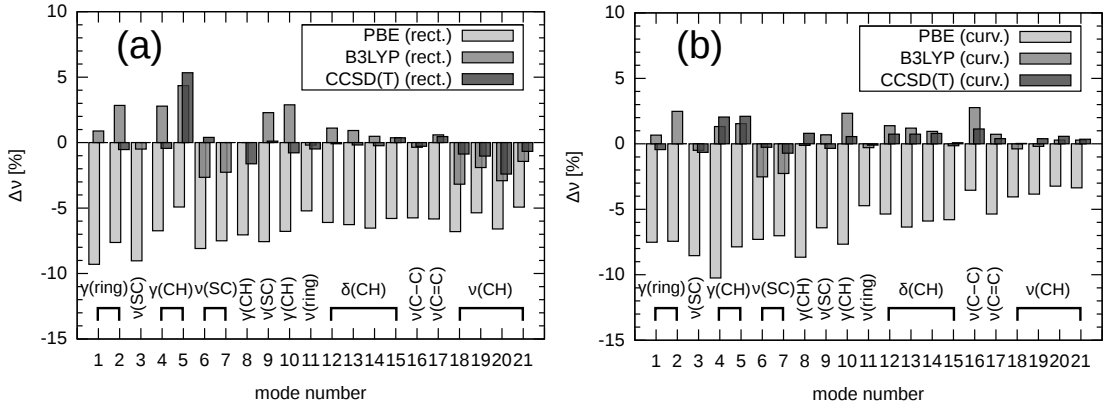

1.5% respectively. This is not surprising, as it was mentioned earlier (see section 2.7) that the rectilinear coordinates lead to artificial couplings between the stretching and bending modes. Curvilinear coordinates improve the accuracy by eliminating these coupling terms and reduce the deviation of all ν(CH) frequencies to below 1%.

For the B3LYP PES, a similar tendency is observed. Thus, in case of the rectilinear coordinates the overall accuracy is equal to 36 cm^{-1}. In rectilinear coordinates, the most inaccurate modes are ν(CH) and γ(CH) due to artificial couplings between them. Similarly to the CCSD(T) results, curvilinear coordinates eliminate these couplings and significantly improve the RMSD error (from 36 cm^{-1} to 14 cm^{-1}). However, the change of coordinate representation does not affect the frequencies of the torsional mode [γ(CCCC)], two stretching modes γ(CS) (Nr. 6 and Nr. 7), and the bending γ(CH) mode (Nr. 10) which leads to the slightly excessive RMSD error in comparison with the CCSD(T) PES (9 cm^{-1}). This insensitivity to the type of coordinates, together with the similar distribution of errors over vibrational modes, at the anharmonic (see Figure 6.3) and harmonic levels (see Figure 6.2) allows to conclude that for the mentioned modes the deviation is caused by a deficiency of the PES.

Finally, all anharmonic frequencies computed at PBE level of theory are significantly underestimated regardless of the coordinate representation used. Curvilinear coordinates improves the RMSD error by 25 cm^{-1} (from 99 cm^{-1} to 74 cm^{-1}) by improving the most problematic high-frequency CH stretching modes. However, the

Table 6.3. Experimental and anharmonic (VCIPSI) frequencies of thiophene in the gas phase for the PBE, B3LYP and CCSD(T) PESs in rectilinear (rect.) and curvilinear (curv.) coordinates. The mode assignment convention is: ν – stretching, δ – in-plane bending, γ – out-of-plane bending. The symmetry labels denote irreducible symmetry representation in C_{2v} of the mode. All frequencies are given in cm^{-1}.[1]

Mode number	Sym.	Assignment	PBE		B3LYP		CCSD(T)		Experiment[171]
			rect.	curv.	rect.	curv.	rect.	curv.	
1	B_1	γ(CCSC)	410	418	456	455	452	450	452
2	A_2	γ(CCCC)	521	522	580	578	561	564	564
3	A_1	δ(CSC), ν(SC)	554	557	606	606	609	605	609
4	A_2	γ(CH)	637	613	702	692	680	697	683
5	B_1	γ(CH)	677	656	743	723	750	727	712
6	B_2	δ(CCC), ν(SC)	693	699	734	735	757	752	754
7	A_1	δ(CCC), ν(SC)	777	781	821	821	840	834	840
8	B_1	γ(CH)	805	791	866	865	852	873	866
9	B_2	δ(SCC), ν(SC)	807	817	893	879	874	870	873
10	A_2	γ(CH)	839	831	926	921	893	905	900
11	A_1	ν(ring)	982	987	1034	1033	1031	1035	1036
12	A_1	δ(CH)	1016	1024	1094	1097	1081	1090	1082
13	B_2	δ(CH)	1017	1016	1095	1098	1083	1093	1085
14	B_2	δ(CH)	1174	1182	1262	1268	1253	1266	1256
15	A_1	δ(CH)	1285	1285	1369	1362	1369	1365	1364
16	A_1	ν(C − C)	1329	1360	1405	1449	1406	1426	1410
17	B_2	ν(C = C)	1422	1429	1519	1521	1517	1516	1510
18	B_2	ν(CH)	2877	2962	2989	3075	3060	3088	3087
19	A_1	ν(CH)	2931	2978	3038	3091	3065	3109	3097
20	B_2	ν(CH)	2919	3024	3034	3134	3050	3143	3125
21	A_1	ν(CH)	2972	3021	3081	3135	3105	3137	3126
		RMSD	99	74	36	14	21	9	—

[1] Reprinted in part with permission from D. M. Benoit, B. Madebene, I. Ulusoy, L. Mancera, Y. Scribano, and **S. Chulkov**, "Towards a scalable and accurate quantum approach for describing vibrations of molecule–metal interfaces", *Beilstein J. Nanotechnol.*, **2**, 427–447 (2011). Copyright 2011, Beilstein Institut.

remaining error is still high, and interpretation of the experimental spectra based of these PBE anharmonic frequencies inevitably leads to mode misassignment. For this reason, it is advisable to use our fragment method to discribe accurately the vibrations of adsorbed thiophene (see below).

Figure 6.4. Optimal geometry of a thiophene molecule adsorbed on a Au(111) surface.

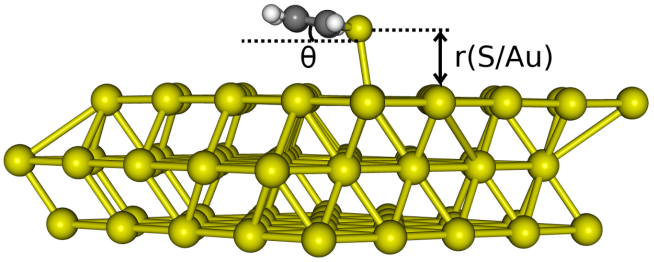

Table 6.4. Optimal geometry and adsorption energy of thiophene adsorbed on a Au(111) surface. r(S/Au) denotes the distance between the sulphur atom and the gold surface, while θ denotes the dihedral angle between the thiophene ring and the gold surface.

	r(C-S), Å	r(C-C), Å	r(S/Au), Å	θ, °	E_{ads}, eV
C_4H_4S/Au(111)	1.729	1.427	2.768	16.9	−0.31
C_4H_4S/gas	1.712	1.424	—	—	—
Experiment [162]	—	—	—	19±10	−0.56

6.2 Thiophene on a Au(111) surface

As starting point a thiophene molecule adsorbed on a Au(111) surface was optimised using periodic DFT method with the PBE functional. The Au(111) surface was simulated as slabs consisting of 6 layers with two fixed lowest layers. A (5×5) unit cell separated by 20 Å of vacuum along the surface normal direction was used. The cell vector was optimized for the whole adsorbed system by performing a set of optimizations with different Au–Au inter-atomic distance. The minimal energy was obtained at the distance of 2.947 Å that is close to the theoretical distance for bulk gold (2.949 Å). The TZV2P-MOLOPT-GTH basis set was used for all atoms except gold, for which the double-zeta valence basis set with one polarization function (DZVP-MOLOPT-SR-GTH) was utilized. Core electrons were described using GTH pseudopotentials. The plane wave cutoff was set to 600 Ry. The coverage was one thiophene molecule per unit cell or per 25 gold atoms.

Figure 6.4 shows the optimal structure of an adsorbed thiophene molecule. In addition the energy of adsorption and some structural parameters are presented in Table 6.4. Note that during adsorption from the gas phase, the thiophene

molecule remains flat preserving its C_{2v} symmetry. The r(C-S) and r(C-C) interatomic distances are elongated by 0.017 Å and 0.003 Å respectively, while other bond lengths remain constant (for clarity these bond length are not shown in Table 6.4). The molecule adsorbs on an on-top site, 2.768 Å above the surface and at an angle of 16.9 degrees relatively to the surface. This angle is in good agreement with an experimentally observed one (19°) which was reported for the same coverage. At the same time, the predicted energy of adsorption is equal to −0.31 eV that is almost two times lower than the corresponding experimental energy (−0.56 eV). However, it is in agreement with another DFT study [172] where a similar adsorption energy (−0.37 eV) was found for slightly higher coverage (one thiophene molecule per 16 gold atoms).

Thiophene in the gas phase has three translational and three rotational modes which are transformed into six extra vibrational modes upon adsorption. Among them are three frustrated translations, one frustrated rotation and two modes corresponding to the alteration of the dihedral angle between the molecule and the surface. However, in normal-mode coordinates these modes does not exist in their pure states but involve gold atoms into vibrations as well. This leads to delocalization of each of these six extra modes among many adsorbate-metal normal modes and renders their interpretation difficult. The thiophene's tilt angle changes during various motions of gold atoms from the top layer into the z direction. It may originate from an inclination of the top gold layer with respect to the other layers, by a "bending" of this top layer, or by numerous intermediate vibrations. The situation is also complicated by mode-mode couplings. Many of these modes are likely coupled together, and their number grows rapidly with the number of atoms in the top layer. Moreover, the inclination of the upper gold layer does not only change the tilt angle θ but also affects the distance between the thiophene molecule and the surface. It couples tilting modes with the frustrated translations and complicates their simulation in rectilinear coordinates.

Unfortunately, the current implementation of curvilinear coordinates in PVSCF does not allow us to use them for periodic systems. For this reason an anharmonic

PES was computed using rectilinear normal-mode coordinates and only mode-mode couplings between 21 adsorbate vibrations were taken into account. By analogy with acetylene on a Cu(001) surface (see chapter 5.5), where all intra-adsorbate and adsorbate-metal vibrations are decoupled, we expect a similar situation to occur in this case too. In fact, the thiophene-gold vibrational modes may be separated from lattice vibrations using a partial Hessian technique (see Section 2.6) by freezing almost all gold atoms. However, within this technique active gold atoms should be chosen with care and each selection requires additional tests. As there are no experimental frequencies reported in the literature for thiophene-gold vibrations we focus exclusively on the intra-thiophene vibrational modes.

The harmonic and anharmonic frequencies of these vibrational modes are shown in Table 6.5. The anharmonic PES was constructed within the pairwise approximation, with all possible 2-D couplings between 21 adsorbate vibrations (210 pair couplings). For each normal mode, 14 single point energies (SPEs) for each 1-D curve and 14×14 SPEs for each 2-D coupling were computed (41454 SPEs in total). The frequencies were computed using the VCIPSI method where the number of possible virtual states was limited up to 7 excitation quanta for each normal mode.

The anharmonic frequencies were also computed within the fragment method, where the thiophene molecule was described at the CCSD(T) *ab initio* level of theory using cc-pVTZ basis set. Because the adsorption has a little effect on the optimal geometry of the thiophene molecule, the wave function of isolated thiophene molecule remains single-reference upon adsorption. This permits to apply the fragment method for this system without adding any extra link atom.

The only available vibrational spectrum of thiophene adsorbed on a Au(111) surface was recorded by Matsuura and Shimoyama [163] using FT-IRRAS technique. They observed only one peak at 720 cm^{-1} and assigned it to a γ(CH) mode based on the transmission IR spectra of thiophene in the liquid state. This peak is in agreement with anharmonic frequencies computed using both PESs (the PBE PES and the hybrid PES), but a single data point does not allow a reliable assessment of the accuracy. For this reason, in addition to the FT-IRRAS spectra, a HREELS

Table 6.5. Harmonic and anharmonic (VCIPSI) and experimental frequencies of thiophene on a Au(111) surface. Modes are sorted in the same order as for thiophene in the gas phase. The mode assignment convention is: ν – stretching, δ – in-plane bending, γ – out-of-plane bending. The symmetry labels denote irreducible symmetry representation in C_{2v} of the mode. The index (w) labels weak bands in experimental spectra. All frequencies are given in cm^{-1}.

Mode number	Sym.	Assignment	Harmonic PBE	VCIPSI PBE	VCIPSI PBE|CCSD(T)	Experiment
1	B_1	γ(CCSC)	436	427	428	430[1]
2	A_2	τ(CCCC)	544	539	538	
3	A_1	δ(CSC), ν(SC)	592	583	590	
4	A_2	γ(CH)	668	679	718	720[2]; 730[1]
5	B_1	γ(CH)	712	730	751	
6	B_2	δ(CCC), ν(SC)	717	703	717	
7	A_1	δ(CCC), ν(SC)	812	797	806	
8	B_1	γ(CH)	844	849	895	
9	B_2	δ(SCC), ν(SC)	852	838	859	860(w)[*,1]
10	A_2	γ(CH)	885	883	912	
11	A_1	ν(ring)	1030	1012	1024	
12	A_1	δ(CH)	1071	1061	1083	1080(w)[1]
13	B_2	δ(CH)	1069	1058	1086	
14	B_2	δ(CH)	1232	1212	1253	
15	A_1	δ(CH)	1343	1317	1360	
16	A_1	ν(C − C)	1400	1359	1394	1400(w)[1]
17	B_2	ν(C = C)	1485	1452	1501	
18	B_2	ν(CH)	3140	2931	3023	
19	A_1	ν(CH)	3150	2964	3053	
20	B_2	ν(CH)	3176	2960	3045	
21	A_1	ν(CH)	3179	3013	3087	3130(w)[1]

[*] In Ref. [173] the frequency is assigned to the mode Nr. 7 according to the IR vapor spectrum from Ref. [174]
[1] HREELS spectrum of C_4H_4S/Cu(100) at 210 K, data from Ref. [173]
[2] FT-IRRAS spectrum of C_4H_4S/Au(111), data from Ref. [163]

spectra of thiophene adsorbed on a Cu(100) [173] surfaces at low coverage was used as a reference one. Similar spectra were also measured for thiophene adsorbed on Pt(111) [175], Mo(100) [176] and Fe(100) [177] surfaces. However, in contrast with Pt, Mo, and Fe, copper and gold atoms have an identical electronic configuration of valence electrons ($d^{10}s^1$). Moreover, despite of the fact that the thiophene molecule adsorbs on Cu(100) on a bridge site [178], rather than on an on-top site, the Cu(100) surface is similar to the Au(111) surface in the sense that the thiophene molecule does not dissociate on it [173].

Harmonic frequencies computed using the PBE PES provide a good match with

Figure 6.5. Relative deviation (in %) of harmonic and anharmonic frequencies of thiophene upon adsorption on Au(111) from the gas phase (PBE PES). At the harmonic level only those modes which correspond to out-of-plane vibrations or moving the sulphur atom along the surface are significantly altered, while all anharmonic frequencies are shifted upward upon adsorption.

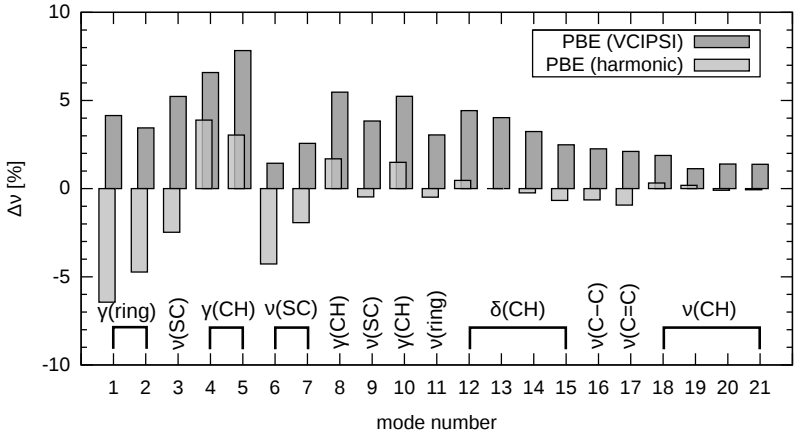

available experimental data. The least accurate modes are the C − H stretches which are overestimated by approximately 50 cm^{-1}, For the other modes the maximal deviation does not exceed 20 cm^{-1} and is on average 6 cm^{-1}. However, comparison between harmonic and anharmonic frequencies suggests that this agreement is the result of error cancellation. In particular, the frequencies of all ν(CH) modes are shifted downward by 6% or by 195 cm^{-1} on average, while other modes show anharmonicity of $\sim 2\%$. There are also modes whose frequencies are increased at the anharmonic level; all of them are correspond to out-of-plane C − H vibrations.

Figure 6.5 shows the frequency shifts of harmonic and anharmonic frequencies upon adsorption. At the harmonic level there is a strong correlation between the type of vibration and the size of the shift. Those modes which involve sulphur atom see a decrease in frequencies upon adsorption due to the interaction between gold and sulphur atoms. Alternatively, all γ(CH) modes increase their frequencies due to the repulsion between the gold and hydrogen atoms. The last group is the modes which correspond to in-plane vibrational motion. These vibrational frequencies are shifted slightly because they represent a motion parallel to the surface. At the same time all anharmonic frequencies are shifted upward during adsorption, while the

value of the shift does not demonstrate any particular pattern.

Alternatively, anharmonic frequencies of CH stretching modes computed using the hybrid PBE|CCSD(T) PES demonstrate systematic improvements with respect to the PBE PES. These frequencies are up-shifted relative to their anharmonic equivalents on average by 85 cm^{-1}. The predicted frequency for symmetric ν(CH) mode (Nr. 21) is lower than the corresponding experimental value by 40 cm^{-1} and is closer than the harmonic one. The fragment method also improves the frequency of the $\nu(C-C)$ and the δ(CH) modes.

6.3 Terthiophene on a Au(111) surface

Maurer and Koslowski [165] recorded a detailed STM-IETS spectra of terthiophene (3T) on the Au(111) surface in the region up to 120 meV (970 cm^{-1}). Vibrational frequencies in this region are especially important, as they particularly sensitive to the location of the adsorbate on the surface [14]. Among them are out-of-plane $C-H$ bending modes. However, in rectilinear normal-mode coordinates these modes are strongly coupled and require high-order coupling terms to describe them accurately. Moreover, this region contains internal rotations which also require curvilinear coordinates. For this reason, as a first approximation the anharmonic frequencies were computed for a 3T molecule in the gas phase, because curvilinear coordinates are still not implemented in PVSCF for adsorbed systems.

The VCIPSI anharmonic frequencies were computed in curvilinear coordinates within the pairwise approximation using the DFT/B3LYP level of theory with TZV2P basis set. By analogy with the thiophene molecule (see section 6.1) using this PES we expect to achieve reasonable accuracy.

The first 33 fundamental frequencies along with the STM-IETS data of 4 independent experiments are listed in Table 6.6. The computed frequencies are in good agreement with the experimental data. Thus, the maximal deviation from the experiment does not exceed 3 meV, that is very close to the experimental accuracy (2 meV). Nevertheless, two experimental peaks remain unassigned. One peak lies

within the interval between 32 meV and 35 meV and it is observed in all four spectra. A similar peak was observed for clean Cu(111) surface by Vitali et al. [179] who concluded that it was caused by the structure of a tip apex. The second unassigned peak is observed between 99 meV and 102 meV that is in the middle between the frequency of out-of-plane CH bending mode and CSC stretching mode. This mode is likely the result of adsorption which shifts one of the modes mentioned above.

Because the experimental spectrum of the adsorbed 3T is in good agreement with gas-phase anharmonic frequencies, it allows us to conclude that there is only a weak interaction between 3T and the Au(111) surface. This also supported by the scanning tunnelling spectroscopy experiments [180] where a similar energy difference between the highest occupied and the lowest unoccupied molecular orbitals were achieved for the adsorbed and free 3T molecules.

An alternative spectrum of 3T on Au(111) was measured by Matsuura and Shimoyama [163] using FT-IRRAS technique. They found one peak at 84 meV and assigned it to out-of-plane CH bending mode. This assignment is based on the selection rules which assumes a parallel orientation of the 3T molecule relative to the surface. However, this assignment contradicts our results based on gas-phase frequencies which assign this frequency to the in-plane antisymmetric CSC stretching mode. However, according to the STM image [180], the 3T molecule is not exactly parallel with the surface and thus it possible to detect this in-plane vibration using RAIRS.

Table 6.6. Theoretical anharmonic frequencies (B3LYP/TZV2P) of 3T/gas and STM-IETS frequencies of 3T/Au(111) obtained from 4 independent experiments. Labels "ip" and "oop" denote in-plane and out-of-plane vibrations about the plane of the molecule. The symmetry labels denote irreducible symmetry representation about the plane in C_s which is perpendicular to the molecular plane. All units are given in meV.

mode	Assignment	Sym.	Direction	VCIPSI B3LYP	Experiment [165]
1	Frustrated ring rotation	A_2	oop	3.1	2.4
2	Frustrated ring rotation	A_1	oop	3.4	
3	Molecular bending	A_1	oop	7.3	6.1, 6.2, 6.7
4	Frustrated ring rotation	A_1	ip	8.2	
5	Ring wag	A_2	oop	18.7	16.7, 18.1, 18.9, 19.9
6	Frustrated ring rotation	A_2	ip	18.9	
7	Inner ring breathing	A_1	ip	25.5	22.5, 23.7, 24,6
8	Ring wag	A_2	oop	29.6	27.5, 27.8, 29.1
	Tip?	—			32.4, 33.6, 34.0, 34.9
9	Frustrated ring translation	A_1	ip	41.3	41.2, 42.1, 43.3
10	Ring wag	A_2	oop	43.2	
11	Frustrated ring translation	A_2	ip	43.7	
12	Ring rotation	A_2	ip	54.7	52.4, 52.9, 54.4, 54.6
13	Ring deformation	A_1	oop	60.7	60.9, 61.0, 63.1
14	Ring deformation	A_2	oop	66.5	66.8, 67.0, 69.4
15	Ring deformation	A_1	oop	73.1	
16	Ring deformation	A_2	oop	75.6	74.7
17	CSC stretch	A_1	ip	75.7	
18	Ring deformation	A_1	oop	78.5	79.3, 80.4, 82.3, 82.5
19	Ring deformation	A_2	oop	79.8	
20	Outer ring CSC stretch	A_2	ip	81.0	
21	CSC stretch	A_2	ip	88.6	86.8, 86.9
22	Outer ring CSC stretch	A_1	ip	91.3	90.6, 91.6, 95.2, 96.4
23	Outer ring CSC stretch	A_2	ip	91.8	
24	Ring breathing	A_1	ip	92.7	
25	Inner ring CH bend	A_1	oop	92.9	
	Shifted mode?				99.7, 101.0, 101.2
26	Outer ring CSC stretch	A_1	ip	104.5	104.5, 106.0, 107.3
27	Outer ring CSC stretch	A_2	ip	106.5	
28	CSC stretch	A_1	ip	109.0	109.1, 110.5, 112.2
29	Outer ring CH bend	A_1	oop	109.8	
30	Outer ring CH bend	A_2	oop	114.3	112.8
31	Outer ring CH bend	A_2	oop	116.2	117.3, 117.9, 119.5
32	Outer ring CH bend	A_1	oop	116.9	
33	CSC stretch	A_2	ip	124.9	

[1] Reprinted with permission from B. Koslowski, N. Maurer, M. Stocker, **S. K. Chulkov**, D. M. Benoit, and P. Ziemann, "Analysis of rich inelastic electron tunneling spectra: Case study of terthiophene on Au(111)", *Rev. Sci. Instrum.*, **84**, 043907 (2013). Copyright 2013, AIP Publishing LLC.

Chapter 7

Summary

Adsorbed systems are very complex from the perspective of electronic structure theory. Indeed, electrons in metals are uniformly distributed. Therefore, such systems are usually described using the density functional theory with an exchange-correlation functional which approaches the uniform electron gas limit. However, the density functional theory is liable to self-interaction problem as it allows electrons to repulse from themselves. Since this self-interaction delocalizes electrons, it is usually not completely compensated by the functionals designed for metals. As the result, such functionals often over-delocalize electrons of adsorbed molecules that softens intra-adsorbate bonds. For the very same reason, the methods that are usually applied for adsorbed molecules do not work properly for their metal support.

The mentioned softening of the molecular bonds may accidentally lead to accurate harmonic frequencies. However these "correct" frequencies are obtained by the wrong reason, due to compensation of this bond weakness by neglecting anharmonicity. Unfortunately, it is impossible to know in advance how accurate the obtained harmonic frequencies are for a particular electronic method and for a particular adsorbed system.

Our fragment method provides an elegant way to overcome this problem. Within this method we estimate the value of the excessive exchange by extracting the molecule and describing it using a suitable level of theory. Applicability of this approach was demonstrated using two examples. For acetylene on Cu(001) this fragment method

doubles the accuracy of anharmonic frequencies (from RMSD = 88 cm^{-1} for PBE PES down to 45 cm^{-1} for PBE|CCSD(T) PES). Moreover, the achieved accuracy is identical to the accuracy of the high-level *ab initio* method used for isolated acetylene molecule. Despite of the large influence of the dispersion correction on acetylene adsorption energy (−0.92 eV) this correction has only small effect on anharmonic frequencies (4 cm^{-1}).

At the same time, the obtained hybrid anharmonic frequencies of a thiophene molecule adsorbed on a Au(111) surface are in agreement with the available single data point. Besides, these frequencies agree closely with an alternative spectrum of a thiophene molecule on a Cu(001) surface, except for high-frequency $C-H$ stretching modes. The similarity between the obtained adsorbate and gas-phase spectra demonstrates the weakness of adsorption. The same weak adsorption is also observed for a terthiophene molecule adsorbed on the Au(111) surface, whose gas-phase anharmonic frequencies are nearly match the corresponding adsorbate frequencies.

The proposed fragment method is relatively simple and does not rely on a specific quantum chemistry program. The method provides a hierarchical way to improve the anharmonic adsorbate frequencies. Thus, the improvement can be achieved by increasing the level of the electronic structure theory. Taking into account higher order terms also helps. In order to make it possible, a general m-dimensional VCI solver was implemented. Despite of the fact that at this stage, this high-order couplings are only tractable for relatively small molecules, the future advances in computer hardware might accelerate the calculations of these couplings.

The low-frequency vibrations between lattice and adsorbate are the main challenge for our fragment method. It can be seen for the acetylene adsorbed on a Cu(001) surface that the acetylene–copper stretching modes is less accurate in comparison with anharmonic frequencies obtained using PBE functional. However, the reason for this weakening is the use of rectilinear normal mode coordinates, which introduce artificial coupling between vibrations. Thus, implementation of this types of coordinates for the adsorbed system remains the main priority.

Nevertheless, the fragment method provides a way to obtain correct frequencies for the right reason. We hope, that it can help to construct a new type of exchange-correlation functionals which overcome limitations of the current functionals.

Bibliography

[1] S. T. Marshall and J. W. Medlin, "Surface-level mechanistic studies of adsorbate–adsorbate interactions in heterogeneous catalysis by metals", *Surf. Sci. Rep.*, **66**, 173–184 (2011).

[2] G. Binnig, H. Rohrer, Ch. Gerber, and E. Weibel, "Surface studies by scanning tunneling microscopy", *Phys. Rev. Lett.*, **49**, 57–61 (1982).

[3] C. Davisson and L. H. Germer, "Diffraction of electrons by a crystal of nickel", *Phys. Rev.*, **30**, 705–740 (1927).

[4] R. E. Schlier and H. E. Farnsworth, "Low-energy electron diffraction investigation of chemisorbed gases on the (100) faces of copper and nickel single crystals", *J. Appl. Phys.*, **25**, 1333–1336 (1954).

[5] C. Ma and J. M. Harris, "Surface-enhanced raman scattering study of the kinetics of self-assembly of carboxylate-terminated n-Alkanethiols on silver", *Langmuir*, **28**, 2628–2636 (2012).

[6] J. A. Stroscio, S. R. Bare, and W. Ho, "The chemisorption and decomposition of ethylene and acetylene on Ni(110)", *Surf. Sci.*, **148**, 499–525 (1984).

[7] A. Politano and G Chiarello, "Vibrational investigation of catalyst surfaces: Change of the adsorption site of CO molecules upon coadsorption", *J. Phys. Chem. C*, **115**, 13541–13553 (2011).

[8] F. M. Hoffman, "Infrared reflection-absorption spectroscopy of adsorbed molecules", *Surf. Sci. Rep.*, **3**, 107–192 (1983).

[9] E. L. Wilson and W. A. Brown, "Low pressure rairs studies of model catalytic systems", *J. Phys. Chem. C*, **114**, 6879–6893 (2010).

[10] K. Kim and K. S. Shin, "Surface-enhanced raman scattering: A powerful tool for chemical identification", *Analyt. Sci.*, **27**, 775–783 (2011).

[11] R. C. Jaklevic and J. Lambe, "Molecular vibration spectra by electron tunneling", *Phys. Rev. Lett.*, **17**, 1139–1140 (1966).

[12] X.-H. Qiu, G. V. Nazin, and W. Ho, "Vibrationally resolved fluorescence excited with submolecular precision", *Science*, **299**, 542–546 (2003).

[13] J. A. Stearns, S. Mercier, C. Seaiby, M. Guidi, O. V. Boyarkin, and T. R. Rizzo, "Conformation-specific spectroscopy and photodissociation of cold, protonated tyrosine and phenylalanine", *J. Phys. Chem. C*, **129**, 11814–11820 (2007).

[14] I. S. Ulusoy, Y. Scribano, D. M. Benoit, A. Tschetschetkin, N. Maurer, B. Koslowski, and P. Ziemann, "Fast degenerate correlation-corrected vibrational self-consistent field calculations of the vibrational spectrum of 4-mercaptopyridine", *Phys. Chem. Chem. Phys.*, **13**, 612–618 (2011).

[15] B. N. J. Persson and A. Baratoff, "Inelastic electron tunneling from a metal tip: The contribution from resonant processes", *Phys. Rev. Lett.*, **59**, 339–342 (1987).

[16] A. Troisi and M. A. Ratner, "Propensity rules for inelastic electron tunneling spectroscopy of single-molecule transport junctions", *J. Chem. Phys..*, **125**, 214709 (2006).

[17] M. Paulsson, T. Frederiksen, H. Ueba, N. Lorente, and M. Brandbyge, "Unified description of inelastic propensity rules for electron transport through nanoscale junctions", *Phys. Rev. Lett.*, **100**, 226604 (2008).

[18] M. D. Halls, J. Velkovski, and H. B. Schlegel, "Harmonic frequency scaling factors for Hartree-Fock, S-VWN, B-LYP, B3-LYP, B3-PW91 and MP2 with the Sadlej pVTZ electric property basis set", *Theor. Chem. Acc.*, **105**, 413–421 (2001).

[19] J. P. Merrick, D. Moran, and L. Radom, "An evaluation of harmonic vibrational frequency scale factors", *J. Phys. Chem. A*, **111**, 11683–11700 (2007).

[20] F. Buatier de Mongeot, A. Cupolillo, U. Valbusa, and M. Rocca, "Anharmonicity of the O_2–Ag(001) chemisorption potential", *J. Chem. Phys.*, **106**, 9297–9304 (1997).

[21] G. Rauhut and P. Pulay, "Transferable scaling factors for density functional derived vibrational force fields", *J. Chem. Phys.*, **99**, 3093–3100 (1995).

[22] J. M. Bowman, "Self-consistent field energies and wavefunctions for coupled oscillators", *J. Chem. Phys.*, **68**, 608–610 (1978).

[23] L. S. Norris, M. A. Ratner, A. E. Roitberg, and R. B. Gerber, "Møller-Plesset perturbation theory applied to vibrational problems", *J. Chem. Phys.*, **105**, 11261–11267 (1995).

[24] P. Daneček and P. Bouř, "Comparison of the numerical stability of methods for anharmonic calculations of vibrational molecular energies", *J. Comput. Chem.*, **28**, 1617–1624 (2007).

[25] S. Carter, J. M. Bowman, and N. C. Handy, "Extensions and tests of "multimode": a code to obtain accurate vibration/rotation energies of many-mode molecules", *Theor. Chem. Acc.*, **100**, 191–198 (1998).

[26] O. Christiansen, "Vibrational coupled cluster theory", *J. Chem. Phys.*, **120**, 2149–2159 (2004).

[27] Y. Scribano and D. M. Benoit, "Iterative active-space selection for vibrational configuration interaction calculations using reduced-coupling vscf basis", *Chem. Phys. Lett.*, **458**, 384–386 (2008).

[28] M. Born and R. Oppenheimer, "Zur quantentheorie der molekeln", *Ann. Phys. (Berlin)*, **84**, 457–484 (1927).

[29] F. Jensen, "*Introduction to computational chemistry*", Wiley (2007), ISBN 0470011874.

[30] I. I. Ippolitov and S. V. Katyurin, "Separation of variables for three-body problems. Application to H_2^+", *Sov. Phys. J.*, **22**, 251–255 (1979).

[31] J. M. Bowman and B. Gazdy, "A movable basis method to calculate vibrational energies of molecules", *J. Chem. Phys.*, **93**, 1774–1784 (1990).

[32] E. B. Wilson, J. C. Decius, and P. C. Cross, "*Molecular vibrations: The theory of infrared and raman vibrational spectra*", Dover Publications (1980), ISBN 048663941X.

[33] C. Eckart, "The kinetic energy of polyatomic molecules", *Phys. Rev.*, **46**, 383–387 (1934).

[34] R. W. Redding and F. O. Meyer III, "On the relation of the Eckart frame to the Eulerian angles", *J. Mol. Spectrosc.*, **74**, 486–487 (1979).

[35] D. R. J. Boyd and H. C. Longuet-Higgins, "Coriolis interaction between vibration and rotation in symmetric top molecules", *Proc. R. Soc. Lond. A*, **213**, 55–73 (1952).

[36] F. R. Gantmakher, "*The theory of matrices*", volume 1, Chelsea (1959), New York, ISBN 0828401314.

[37] G. C. Schatz and T. Mulloney, "Collisional energy transfer in polyatomic molecules: A study of anharmonicity effects in Kr+CO_2", *J. Chem. Phys.*, **71**, 5257–5267 (1979).

[38] P. M. Morse, "Diatomic molecules according to the wave mechanics. II. Vibrational levels", *Phys. Rev.*, **34**, 57–64 (1929).

[39] S. Flügge, P. Walger, and A. Weiguny, "A generalization of the morse potential for diatomic molecules", *J. Mol. Spectrosc.*, **23**, 243–257 (1967).

[40] M. E. Jacox and D. E. Milligan, "Matrix-isolation study of the vacuum-ultraviolet photolysis of methyl chloride and methylene chloride. Infrared and ultraviolet spectra of the free radicals CCl, H_2CCl, and CCl_2", *J. Chem. Phys.*, **53**, 2688–2701 (1970).

[41] P. B. Kelly and S. G. Westre, "Resonance raman spectroscopy of the methyl radical", *Chem. Phys. Lett.*, **151**, 253–257 (1988).

[42] C. C. Marston and G. G. Balint-Kurti, "The Fourier Grid Hamiltonian method for bound state eigenvalues and eigenfunctions", *J. Chem. Phys.*, **91**, 3571–3576 (1989).

[43] G. G. Balint-Kurti, R. N. Dixon, and C. C. Marston, "Grid methods for solving the Schrödinger equation and time dependent quantum dynamics of molecular photofragmentation and reactive scattering processes", *Int. Rev. Phys. Chem.*, **11**, 317–344 (1992).

[44] J. O. Jung and R. B. Gerber, "Vibrational wave functions and spectroscopy of $(H_2O)_n$, n=2,3,4,5: Vibrational selfconsistent field with correlation corrections", *J. Chem. Phys.*, **105**, 10332–10348 (1996).

[45] S. Carter, S. J. Culik, and J. M. Bowman, "Vibrational self-consistent field method for many-mode systems: A new approach and application to the vibrations of CO adsorbed on Cu(100)", *J. Chem. Phys.*, **107**, 10458–10469 (1997).

[46] K. Yagi, T. Taketsugu, K. Hirao, and M. S. Gordon, "Direct vibrational self-consistent field method: Applications to H_2O and H_2CO", *J. Chem. Phys.*, **113**, 1005–1017 (1999).

[47] G. Rauhut, "Efficient calculation of potential energy surfaces for the generation of vibrational wave functions", *J. Chem. Phys.*, **121**, 9313–9322 (2004).

[48] R. B. Gerber, S. K. Chaban, G. M. amd Gregurick, and B. Brauer, "Vibrational spectroscopy and the development of new force fields for biological molecules", *Biopolymers*, **68**, 370–382 (2003).

[49] O. Christiansen, "Møller-Plesset perturbation theory for vibrational wave functions", *J. Chem. Phys.*, **119**, 5773–5781 (2003).

[50] N. Matsunaga, G. M. Chaban, and R. B. Gerber, "Degenerate perturbation theory corrections for the vibrational self-consistent field approximation: Method and applications", *J. Chem. Phys.*, **117**, 3541–3547 (2002).

[51] K. M. Christoffel and J. M. Bowman, "Investigations of self-consistent field, SCF CI and virtual stateconfiguration interaction vibrational energies for a model three-mode system", *Chem. Phys. Lett.*, **85**, 220–224 (1982).

[52] G. M. Chaban, J. O. Jung, and R. B. Gerber, "Ab initio calculation of anharmonic vibrational states of polyatomic systems: Electronic structure combined with vibrational self-consistent field", *J. Chem. Phys.*, **111**, 1823–1829 (1999).

[53] D. M. Benoit, "Efficient correlation-corrected vibrational self-consistent field computation of OH-stretch frequencies using a low-scaling algorithm", *J. Chem. Phys.*, **125**, 244110 (2006).

[54] J. D. Head, "Computation of vibrational frequencies for adsorbates on surfaces", *Int. J. Quantum Chem.*, **65**, 827–838 (1997).

[55] N. A. Besley and J. A. Bryan, "Partial hessian vibrational analysis of organic molecules adsorbed on Si(100)", *J. Phys. Chem. C*, **112**, 4308–4314 (2008).

[56] R. B. Campos, F. Wypych, and H. P. M. Filho, "Theoretical estimates of the IR spectrum of formamide intercalated into kaolinite", *Int. J. Quantum Chem.*, **111**, 2137–2148 (2011).

[57] N. A. Besley and K. A. Metcalf, "Computation of the amide I band of polypeptides and proteins using a partial Hessian approach", *J. Chem. Phys.*, **126**, 035101 (2007).

[58] G. M. Chaban, J. O. Jung, and R. B. Gerber, "Anharmonic vibrational spectroscopy of glycine: Testing of *ab initio* and empirical potentials", *J. Phys. Chem. A*, **104**, 10035–10044 (2000).

[59] D. M. Benoit, "Fast vibrational self-consistent field calculations through a reduced mode-mode coupling scheme", *J. Chem. Phys.*, **120**, 562–573 (2004).

[60] Y. Scribano, D. M. Lauvergnat, and D. M. Benoit, "Fast vibrational configuration interaction using generalized curvilinear coordinates and self-consistent basis", *J. Chem. Phys.*, **133**, 094103 (2010).

[61] A. Nauts and X. Chapuisat, "Momentum, quasi-momentum and hamiltonian operators in terms of arbitrary curvilinear coordinates, with special emphasis on molecular hamiltonians", *Mol. Phys.*, **55**, 1287–1318 (1985).

[62] C. Møller and M. S. Plesset, "Note on an approximation treatment for many-electron systems", *Phys. Rev.*, **46**, 618–622 (1934).

[63] R. J. Bartlett, "Coupled-cluster approach to molecular structure and spectra: A step toward predictive quantum chemistry", *J. Phys. Chem.*, **93**, 1697–1708 (1989).

[64] J. Čížek, "On the correlation problem in atomic and molecular systems. Calculation of wavefunction components in Ursell-type expansion using quantum-field theoretical methods", *J. Chem. Phys.*, **45**, 4256–4266 (1966).

[65] Bartlett. R. J. Noga, J., "he full CCSDT model for molecular electronic structure", *J. Chem. Phys.*, **86**, 7041–7050 (1987).

[66] K. Raghavachari and G. W. Trucks, "A fifth-order perturbation comparison of electron correlation theories", *Chem. Phys. Lett.*, **157**, 479–483 (1989).

[67] P. Hohenberg and W. Kohn, "Inhomogeneous electron gas", *Phys. Rev.*, **136**, B864–B871 (1964).

[68] J. P. Perdew, K. Burke, and M. Ernzerhof, "Generalized gradient approximation made simple", *Phys. Rev. Lett.*, **77**, 3865–3868 (1996).

[69] A. D. Becke, "A new mixing of Hartree-Fock and local density-functional theories", *J. Chem. Phys.*, **98**, 1372–1377 (1993).

[70] M. Ernzerhof and G. E. Scuseria, "Assessment of the Perdew-Burke-Ernzerhof exchange-correlation functional", *J. Chem. Phys.*, **110**, 5029–5036 (1999).

[71] D. Bakowies and W. Thiel, "Hybrid models for combined quantum mechanical and molecular mechanical approaches", *J. Phys. Chem.*, **100**, 10580–10594 (1996).

[72] M. J. Field, P. A. Bash, and M. Karplus, "A combined quantum mechanical and molecular mechanical potential for molecular dynamics simulations", *J. Comput. Chem.*, **11**, 700–733 (1989).

[73] F. Maseras and K. Morokuma, "IMOMM: A new integrated ab initio + molecular mechanics geometry optimization scheme of equilibrium structures and transition states", *J. Comput. Chem.*, **16**, 1170–1179 (1995).

[74] S. Dapprich, I. Komáromi, K. S. Byun, K. Morokuma, and Frisch M. J., "A new ONIOM implementation in Gaussian98. Part I. The calculation of energies, gradients, vibrational frequencies and electric field derivatives", *J. Mol. Struct.: THEOCHEM*, **461-462**, 1–21 (1999).

[75] J. Sauer and M. Sierka, "Combining quantum mechanics and interatomic potential functions in ab initio studies of extended systems", *J. Comput. Chem.*, **21**, 1470–1493 (2000).

[76] A. K. Rappe and W. A. Goddard, "Charge equilibration for molecular dynamics simulations", *J. Phys. Chem.*, **95**, 3358–3363 (1991).

[77] D. Bakowies and W. Thiel, "Semiempirical treatment of electrostatic potentials and partial charges in combined quantum mechanical and molecular mechanical approaches", *J. Comput. Chem.*, **17**, 87–108 (1998).

[78] D. Das, K. P. Eurenius, E. M. Billings, P. Sherwood, D. C. Chatfield, M. Hodošek, and B. R. Brooks, "Optimization of quantum mechanical molecular mechanical partitioning schemes: Gaussian delocalization of molecular mechanical charges and the double link atom method", *J. Chem. Phys.*, **117**, 10534–10547 (2002).

[79] I. Antes and W. Thiel, "Adjusted connection atoms for combined quantum mechanical and molecular mechanical methods", *J. Phys. Chem. A*, **103**, 9290–9295 (1999).

[80] M. A. Nygren, L. G. M. Pettersson, Z. Barandiarán, and L. Seijo, "Bonding between CO and the MgO(001) surface: A modified picture", *J. Chem. Phys.*, **100**, 2010–2018 (1994).

[81] C. Tuma and J. Sauer, "Treating dispersion effects in extended systems by hybrid MP2:DFT calculations-protonation of isobutene in zeolite ferrierite", *Phys. Chem. Chem. Phys.*, **8**, 3955–3965 (2006).

[82] V. Théry, D. Rinaldi, J.-L. Rivail, B. Maigret, and G. G Ferenczy, "Quantum mechanical computations on very large molecular systems: The local self-consistent field method", *J. Comput. Chem.*, **15**, 269–282 (1994).

[83] P. Gao, J. Amara, C. Alhambra, and M. J. Field, "A generalized hybrid orbital (GHO) method for the treatment of boundary atoms in combined QM/MM calculations", *J. Phys. Chem. A*, **102**, 4714–4721 (1998).

[84] N. Reuter, A. Dejaegere, B. Maigret, and M. Karplus, "Frontier bonds in QM/MM methods: A comparison of different approaches", *J. Phys. Chem. A*, **104**, 1720–1735 (2000).

[85] J. P. Perdew and A. Zunger, "Self-interaction correction to density-functional approximations for many-electron systems", *Phys. Rev. B*, **23**, 5048–5079 (1981).

[86] B. G. Janesko, Henderson T. M., and G. E. Scuseria, "Screened hybrid density functionals for solid-state chemistry and physics", *Phys. Chem. Chem. Phys.*, **11**, 443–454 (2010).

[87] S. K. Chulkov and D. M. Benoit, "A fragment method for systematic improvement of anharmonic adsorbate vibrational frequencies: Acetylene on Cu(001)", *J. Chem. Phys.*, **139**, 214704 (2013).

[88] D. M. Benoit, B. Madebene, I. Ulusoy, L. Mancera, Y. Scribano, and S. Chulkov, "Towards a scalable and accurate quantum approach for describing vibrations of molecule–metal interfaces", *Beilstein J. Nanotechnol.*, **2**, 427–447 (2011).

[89] M. W. Schmidt, K. K. Baldridge, J. A. Boatz, S. T. Elbert, M. S. Gordon, J. H. Jensen, S. Koseki, N. Matsunaga, K. A. Nguyen, S. Su, T. L. Windus, M. Dupuis, and J. A. Montgomery, "General Atomic and Molecular Electronic Structure System", *J. Comput. Chem.*, **14**, 1347–1363 (1993).

[90] H.-J. Werner, P. J. Knowles, G. Knizia, F. R. Manby, M. Schütz, P. Celani, T. Korona, R. Lindh, A. Mitrushenkov, G. Rauhut, K. R. Shamasundar, T. B. Adler, R. D. Amos, A. Bernhardsson, A. Berning, D. L. Cooper, M. J. O. Deegan, A. J. Dobbyn, F. Eckert, E. Goll, C. Hampel, A. Hesselmann, G. Hetzer, T. Hrenar, G. Jansen, C. Köppl, Y. Liu, A. W. Lloyd, R. A. Mata, A. J. May, S. J. McNicholas, W. Meyer, M. E. Mura, A. Nicklass, D. P. O'Neill, P. Palmieri, D. Peng, K. Pflüger, R. Pitzer, M. Reiher, T. Shiozaki, H. Stoll, A. J. Stone, R. Tarroni, T. Thorsteinsson, and M. Wang. "Molpro, version 2012.1, a package of ab initio programs", 2012. See http://www.molpro.net.

[91] D. M. Benoit, "Fast vibrational calculation of anharmonic OH-stretch frequencies for two low-energy noradrenaline conformers", *J. Chem. Phys.*, **129**, 234304 (2008).

[92] W. H. Press, S. A. Teukolsky, W. T. Vetterling, and B. P. Flannery, "*Numerical recipes: The art of scientific computing*", Cambridge University Press (2007), ISBN 0521880688.

[93] H. Akima, "Algorithm 760: Rectangular-grid-data surface fitting that has the accuracy of a bicubic polynomial", *ACM T. Math. Software*, **22**, 357–361 (1996).

[94] D. Shepard, "A two-dimensional interpolation function for irregularly-spaced data", In *Proceedings of the 1968 23rd ACM national conference*, ACM '68, pages 517–524. ACM (1968).

[95] R. P. A. Bettens and M. A. Collins, "Learning to interpolate molecular potential energy surfaces with confidence: A Bayesian approach", *J. Chem. Phys.*, **111**, 816–826 (1999).

[96] M. Abramowitz and I. A. Stegun, "*Handbook of mathematical functions with formulas, graphs, and mathematics tables*", Dover (1965), New York, ISBN 0486612724.

[97] K. Yagi, Ch. Oyanagi, T. Taketsugu, and K. Hirao, "*Ab initio* potential energy surface for vibrational state calculations of H_2CO", *J. Chem. Phys.*, **118**, 1653–1660 (2003).

[98] Ch. Oyanagi, K. Yagi, T. Taketsugu, and K. Hirao, "Highly accurate potential-energy and dipole moment surfaces for vibrational state calculations of methane", *J. Chem. Phys.*, **124**, 064311 (2006).

[99] O. Christiansen, "Selected new developments in vibrational structure theory: potential construction and vibrational wave function calculations", *Phys. Chem. Chem. Phys.*, **14**, 6672–6687 (2012).

[100] T. Ishida and G. C. Schatz, "A local interpolation scheme using no derivatives in potential sampling: Application to $O(^1D) + H_2$ system", *J. Comput. Chem.*, **24**, 1077–1086 (2002).

[101] G. Contopoluos, "A third integral of motion in a galaxy", *Z. Astrophys.*, **49**, 273–291 (1960).

[102] M. Henon and C. Heiles, "The applicability of the third integral of motion: Some numerical experiments", *Astron. J.* , **69**, 73–79 (1964).

[103] W. Eastes and R. A. Marcus, "Semiclassical calculation of bound states of a multidimensional system", *J. Chem. Phys.*, **61**, 4301–4306 (1974).

[104] J. M. Bowman, "The self-consistent-field approach to polyatomic vibrations", *Acc. Chem. Res.*, **19**, 202–208 (1986).

[105] J. Pian and C. S. Sharma, "The generalised Brillouin theorem", *J. Phys. A.: Math. Gen.*, **14**, 1261–1270 (1981).

[106] T. H. Dunning, "Gaussian basis sets for use in correlated molecular calculations. I. The atoms boron through neon and hydrogen", *J. Chem. Phys.*, **90**, 1007 (1989).

[107] N. F. Tennyson, J. Zobov, R. Williamson, O. L. Polyansky, and P. F. Bernath, "Experimental energy levels of the water molecule", *J. Phys. Chem. Ref. Data*, **30**, 735–831 (2001).

[108] H. Ibach, H. Hopster, , and B. Sexton, "Analysis of surface reactions by spectroscopy of surface vibrations", *Appl. Surf. Sci.*, **1**, 1–24 (1977).

[109] J. E. Demuth and H. Ibach, "Experimental study of the vibrations of acetylene chemisorbed on Ni(111)", *Surf. Sci.*, **85**, 365–378 (1979).

[110] P. Tiscione and G. Rovida, "Adsorption and decomposition of ethylene and acetylene on cobalt", *Surf. Sci.*, **154**, L255–L260 (1985).

[111] E. L. Muetterties, M.-C. Tasi, and S. R. Kelemen, "Chemistry of acetylene on platinum (111) and (100) surfaces", *Proc. Natl. Acad. Sci. U.S.A.*, **78**, 6571–6575 (1981).

[112] A. Borodziński and G. C. Bond, "Selective hydrogenation of ethyne in ethene-rich streams on palladium catalysts, Part 2: Steady-state kinetics and effects of palladium particle size, carbon monoxide, and promoters", *Catal. Rev.*, **50**, 379–469 (2008).

[113] W. Sesselmann, B. Woratschek, G. Ertl, J. Küppers, and H. Haberland, "Low temperature formation of benzene from acetylene on a Pd(111) surface", *Surf. Sci.*, **130**, 245–258 (1983).

[114] D. Stacchiola, F. Calaza, T. Zheng, and W. T. Tysoe, "Hydrocarbon conversion on palladium catalysts", *J. Mol. Catal. A: Chem.*, **228**, 35–45 (2005).

[115] N. R. Avery, "Adsorption and reactivity of acetylene on a Cu(110) surface", *J. Am. Chem. Soc.*, **107**, 6711–6712 (1985).

[116] H. Erdmann and P. Köthner, "Einige Beobachtungen über Acetylen und dessen Derivate", *Z. Anorg. Allg. Chem.*, **18**, 48–58 (1898).

[117] B. C. Stipe, M. A. Rezaei, and W. Ho, "Single-molecule vibrational spectroscopy and microscopy", *Science*, **280**, 1732–1735 (1998).

[118] B. C. Stipe, M. A. Rezaei, and W. Ho, "Coupling of vibrational excitation to the rotational motion of a single adsorbed molecule", *Phys. Rev. Lett.*, **81**, 1263–1266 (1999).

[119] L. J. Lauhon and W. Ho, "Control and characterization of a multistep unimolecular reaction", *Phys. Rev. Lett.*, **84**, 1527–1530 (2000).

[120] K.-Y. Yu, W. E. Spicer, I. Lindau, P. Pianetta, and S.-F. Lin, "UPS studies of the bonding of H_2, O_2, CO, C_2H_4 and C_2H_2 on Fe and Cu", *Surf. Sci.*, **57**, 157–183 (1976).

[121] D. Arvanitis, U. Döbler, L. Wenzel, K. Baberschke, and J. Stöhr, "Position of the σ-shape and π resonances of C_2H_2, C_2H_4 and C_2H_6 on Cu(100) at 60K: a NEXAFS study", *Surf. Sci.*, **178**, 686–692 (1986).

[122] D. Arvanitis, L. Wenzel, and K. Baberschke, "Direct evidence of a stretched C-C distance for C_2H_2 and C_2H_4 on Cu(100) at 60K", *Phys. Rev. Lett.*, **59**, 2435–2438 (1987).

[123] J. A. N. F. Bernardo, C. G. P. M. amd Gomes, "Cluster model DFT study of acetylene adsorption on the Cu(100) surface", *J. Mol. Struct.: THEOCHEM*, **629**, 251–261 (2003).

[124] P. Geurts and A. Van Der Avoird, "Hartree-Fock-Slater-LCAO studies of the acetylene-transition metal interaction: II. Chemisorption on Fe and Cu; cluster models", *Surf. Sci.*, **103**, 416–430 (1981).

[125] H. Ren, J. Yang, and Y. Luo, "Simulation of inelastic electronic tunneling spectra of adsorbates from first principles", *J. Chem. Phys.*, **130**, 134707 (2009).

[126] N. Mingo and K. Makoshi, "Calculation of the inelastic scanning tunneling image of acetylene on Cu(100)", *Phys. Rev. Lett.*, **84**, 3694–3697 (2000).

[127] K. Hasegawa, W. A. Diño, H. Kasai, and A. Okiji, "Dynamics of STM-induced acetylene dissociation on Cu(100)", *J. Phys. Soc. JPN*, **71**, 569–573 (2002).

[128] W. Liu, J.-S. Lian, and Q. Jiang, "Theoretical study of C_2H_2 adsorbed on low-index Cu surfaces", *J. Phys. Chem. C*, **111**, 18189–18194 (2007).

[129] L.-F. Yuan, J.-L. Yang, Q.-X. Li, and Q.-S. Zhu, "A first-principles study of acetylene and its evolution products on Cu(001)", *J. Chem. Phys.*, **116**, 3104–3108 (2002).

[130] A. D. Becke, "Density-functional exchange-energy approximation with correct asymptotic-behavior", *Phys. Rev. A*, **38**, 3098–3100 (1988).

[131] C. Lee, W. Yang, and R. G. Parr, "Development of the Colle-Salvetti correlation-energy formula into a functional of the electron density", *Phys. Rev. B*, **37**, 785–789 (1988).

[132] J. Chatt and L. A. Duncanson, "Olefin co-ordination compounds. Part III. Infra-red spectra and structure: attempted preparation of acetylene complexes", *J. Chem. Soc.*, **1953**, 2939–2947 (1953).

[133] I. Ulusoy, "*Vibrational anharmonicity of adsorbates on surfaces*", PhD thesis, Faculty of Natural Science, University of Ulm (2009).

[134] M. Herman, A. Campargue, M. I. El Idrissi, and J. V. Auwera, "Vibrational spectroscopic database on acetylene, $\tilde{X}\ ^1\sigma_g^+$ ($^{12}C_2H_2$, $^{12}C_2D_2$, and $^{13}C_2H_2$)", *J. Phys. Chem. Ref. Data*, **32**, 921–1361 (2003).

[135] L. Pauling and L. O. Brockway, "Carbon—carbon bond distances. The electron diffraction investigation of ethane, propane, isobutane, neopentane, cyclopropane, cyclopentane, cyclohexane, allene, ethylene, isobutene, tetramethylethylene, mesitylene, and hexamethylbenzene. Revised values of covalent radii", *J. Am. Chem. Soc.*, **59**, 1223–1236 (1937).

[136] M. D. Harmony, "The equilibrium carbon-carbon single-bond length in ethane", *J. Chem. Phys.*, **93**, 7522–7523 (1990).

[137] Ts. S. Marinova and P. K. Stefanov, "Adsorption and thermal evolution of acetylene on a Cu(100) surface", *Surf. Sci.*, **191**, 66–74 (1987).

[138] N. Lorente, M. Persson, L. J. Lauhon, and W. Ho, "Symmetry selection rules for vibrationally inelastic tunneling", *Phys. Rev. Lett.*, **86**, 2593–2596 (2001).

[139] J. VandeVondele, M. Krack, F. Mohamed, M. Parrinello, T. Chassaing, and J. Hutter, "QUICKSTEP: Fast and accurate density functional calculations using a mixed Gaussian and plane waves approach", *Comput. Phys. Commun.*, **167**, 103–128 (2005).

[140] *Cp2k developers home page*, URL `http://cp2k.org`.

[141] S. Goedecker, M Teter, and J. Hutter, "Separable dual-space gaussian pseudopotential", *Phys. Rev. B*, **54**, 1703–1710 (1996).

[142] J. VandeVondele and J Hutter, "Gaussian basis sets for accurate calculations on molecular systems in gas and condensed phases", *J. Chem. Phys.*, **127**, 114105 (2007).

[143] S. Grimme, J. Antony, S. Ehrlich, and H. Krieg, "A consistent and accurate ab initio parametrization of density functional dispersion correction (dft-d) for the 94 elements h-pu", *J. Chem. Phys.*, **132**, 154104 (2010).

[144] F. E. Olsson, M. Persson, N. Lorente, L. J. Lauhin, and W. Ho, "Stm images and chemisorption bond parameters of acetylene, ethynyl, and dicarbon chemisorbed on copper", *J. Phys. Chem. B*, **106**, 8161–8171 (2002).

[145] J. Bamidele, A. Brndiar, J. Gulans, L. Kantorovich, and I. Štich, "Critical importance of van der Waals stabilization in strongly chemically bonded surfaces: Cu(110):O", *J. Chem. Theory Comput.*, **9**, 5578–5584 (2013).

[146] K. F. Palmer, M. E. Mickelson, and K. N. Rao, "Investigations of several infrared bands of $^{12}C_2H_2$ and studies of the effects of vibrational rotational interactions", *J. Mol. Spectrosc.*, **44**, 131–144 (1972).

[147] W. J. Lafferty and A. S. Pine, "Spectroscopic constants for the 2.5 and 3.0 μm bands of acetylene", *J. Mol. Spectrosc.*, **141**, 223–230 (1990).

[148] Y. Kabbadj, M. Herman, G. Di Lonardo, L. Fusina, and J. W. C. Johns, "The bending energy levels of C_2H_2", *J. Mol. Spectrosc.*, **150**, 535–565 (1991).

[149] H. G. M. Edwards, "Vibration—rotational raman spectra of acetylene, $^{12}C_2H_2$", *Spectrochim. Acta A*, **46**, 97–106 (1990).

[150] J. H. Burroughes, D. D. C. Bradley, A. R. Brown, R. N. Marks, K. Mackay, R. H. Friend, P. L. Burns, and A. B. Holmes, "Light-emitting diodes based on conjugated polymers", *Nature*, **347**, 539–541 (1990).

[151] A. Hoppe, T. Balster, T. Muck, and V. Wagner, "Scaling limits and MHz operation in thiophene-based field-effect transistors", *Phys. Status Solidi A*, **205**, 612–625 (2008).

[152] C. B Nielsen and I. McCulloch, "Recent advances in transistor performance of polythiophenes", *Prog. Polym. Sci.*, **38**, 2053–2069 (2013).

[153] M. A. DelValle, F. R. Díaz, M. E. Bodini, T. Pizarro, R. Córdova, H. Gómez, and R. Schrebler, "Polythiophene, polyaniline and polypyrrole electrodes modified by electrodeposition of Pt and Pt + Pb for formic acid electrooxidation", *J. Appl. Electrochem.*, **28**, 943–946 (1998).

[154] R. D. McCullough, "The chemistry of conducting polythiophenes", *Adv. Mater.*, **10**, 93–116 (1998).

[155] K. Schulze, C. C. Uhrich, R. Schüppel, K. Leo, M. Pfeiffer, E. Brier, E. Reinold, and P. Bäuerle, "Efficient vacuum-deposited organic solar cells based on a new low-bandgap oligothiophene and fullerene C_{60}", *Adv. Mater.*, **18**, 2872–2875 (2006).

[156] A. Ulmann, "Formation and structure of self-assembled monolayers", *Chem. Rev.*, **96**, 1533–1554 (1996).

[157] X. Chen, E. R. Frank, and R. J. Hamers, "Spatially and rotationally oriented adsorption of molecular adsorbates on Ag(111) investigated using cryogenic scanning tunneling microscopy", *J. Vac. Sci. Technol. B*, **14**, 1136–1140 (1996).

[158] T. Toshiyuki, K. Shigeru, N. Osamu, K. Masato, and N. Tomonobu, "Octithiophene on Cu(111) and Au(111): Formation and electronic structure of molecular chains and films", *J. Nanosci. Nanotechnol.*, **12**, 4007–4011 (2012).

[159] H. Ma, H.-L. Yip, F. Huang, and A. K.-Y. Jen, "Interface engineering for organic electronics", *Adv. Funct. Mater.*, **20**, 1371–1388 (2010).

[160] J. Noh, E. Ito, K. Nakajima, J. Kim, H. Lee, and M. Hara, "High-resolution STM and XPS studies of thiophene self-assembled monolayers on Au(111)", *J. Phys. Chem. B*, **106**, 7139–7141 (2002).

[161] G.-J. Su, H.-M. Zhang, L.-J. Wan, and C.-L. Bai, "Phase transition of thiophene molecules on Au(111) in solution", *Surf. Sci.*, **531**, L363–L368 (2003).

[162] A. Nambu, H. Kondoh, I. Nakai, K. Amemiya, and T. Ohta, "Film growth and X-ray induced chemical reactions of thiophene adsorbed on Au(111)", *Surf. Sci.*, **530**, 101–110 (2003).

[163] T. Matsuura and Y. Shimoyama, "Growth kinetics of self-assembled monolayers of thiophene and terthiophene on Au(111): An infrared spectroscopic study", *Eur. Phys. J. E*, **7**, 233–240 (2002).

[164] Y. Alaverdyan, P. Johansson, and M. Käll, "Photo-induced transformations in 2,2':5',2"-terthiophene thin films on silver", *Phys. Chem. Chem. Phys.*, **8**, 1445–1450 (2006).

[165] B. Koslowski, N. Maurer, M. Stocker, S. K. Chulkov, D. M. Benoit, and P. Ziemann, "Analysis of rich inelastic electron tunneling spectra: Case study of terthiophene on Au(111)", *Rev. Sci. Instrum.*, **84**, 043907 (2013).

[166] B. Koslowski, A. Tschetschetkin, N. Maurer, and P. Ziemann, "4,4'-Dithiodipyridine on Au(111): A combined STM, STS, and DFT study", *J. Phys. Chem. C*, **117**, 20060–20067 (2013).

[167] C. Bürker, N. Ferri, A. Tkatchenko, A. Gerlach, J. Niederhausen, T. Hosokai, S. Duhm, J. Zegenhagen, N. Koch, and F. Schreiber, "Exploring the bonding of large hydrocarbons on noble metals: Diindoperylene on Cu(111), Ag(111), and Au(111)", *Phys. Rev. B*, **87**, 165443 (2013).

[168] T. H. Dunning, "Gaussian basis functions for use in molecular calculations. III. Contraction of (10s6p) atomic basis sets for the firstrow atoms", *J. Chem. Phys.*, **55**, 716 (1971).

[169] A. D. McLean and G. S. Chandler, "Contracted gaussian basis sets for molecular calculations. I. Second row atoms, Z=11–18", *J. Chem. Phys.*, **72**, 5639–5648 (1980).

[170] B. Bak, D. Christensen, L Hansen-Nygaard, and J. Rastrup-Andersen, "The structure of thiophene", *J. Mol. Spectrosc.*, **7**, 58–63 (1962).

[171] T. D. Klots, R. D. Chirico, and M. V. Steele, "Complete vapor phase assignment for the fundamental vibrations of furan, pyrrole and thiophene", *Spectrochim. Acta A*, **50**, 765–795 (1994).

[172] J. Zhou, Y.-X. Yang, P. Liu, N. Camillone, and M. G. White, "Electronic structure of the Thiophene/Au(111) interface probed by two-photon photoemission", *J. Phys. Chem. C*, **114**, 13670–13677 (2010).

[173] B. A. Sexton, "A vibrational and TDS study of the adsorption of pyrrole, furan and thiophene on Cu(100): Evidence for π-bonded and inclined species", *Surf. Sci.*, **163**, 99–113 (1985).

[174] M. Rico, J. M. Orza, and J. Morcillo, "Fundamental vibrations of thiophene and its deuterated derivatives", *Spectrochim. Acta*, **21**, 689–719 (1965).

[175] J. Stöhr, J. L. Gland, E. B. Kollin, R. J. Koestner, Allen L. Johnson, E. L. Muetterties, and F. Sette, "Desulfurization and structural transformation of thiophene on the Pt(111) surface", *Phys. Rev. Lett.*, **53**, 2161–2164 (1984).

[176] F. Zaera, E. B. Kollin, and J. L. Gland, "Vibrational characterization of thiophene decomposition on the Mo(100) surface", *Surf. Sci.*, **184**, 75–89 (1987).

[177] A. B. Cheng, L. Bocarsly, S. L. Bernasek, and T. A. Ramanarayanan, "Adsorption and reaction of thiophene on the Fe(100) surface: Selective dehydrogenation and polymerization", *Surf. Sci.*, **374**, 357–372 (1997).

[178] A. Imanishia, S. Yagib, T. Yokoyamaa, Y. Kitajimac, and T. Ohtaa, "Structural and electronic properties of adsorbed C_4H_4S on Cu(100) and Ni(100) studied by S K-XAFS and S-1s XPS", *J. Electron Spectrosc.*, **80**, 151–154 (1985).

[179] L. Vitali, S. D. Borisova, G. G. Rusina, E. V. Chulkov, and K. Kern, "Inelastic electron tunneling spectroscopy: A route to the identification of the tip-apex structure", *Phys. Rev. B*, **81**, 153409 (2010).

[180] B. Koslowski, A. Tschetschetkin, N. Maurer, E. Mena-Osteritz, P. Bäuerle, and P. Ziemann, "Towards a scalable and accurate quantum approach for describing vibrations of molecule-metal interfaces", *Beilstein J. Nanotechnol.*, **2**, 561–568 (2011).

Appendix A

Copyright permissions

A.1 Beilstein-Institut Open Access License Agreement

(Identical to the 'Creative Commons Attribution License' Version 2.0)

Publisher:	Beilstein-Institut
Publication:	Beilstein Journal of Nanotechnology
Article Title:	Towards a scalable and accurate quantum approach for describing vibrations of molecule-metal interfaces
Author(s):	D. M. Benoit, B. Madebene, I. Ulusoy, L. Mancera, Y. Scribano, and S. Chulkov
Online Publication Date:	Aug 10, 2011
Volume Number:	2
Pages:	427–447

Brief summary of the agreement:

Anyone is free:

- to copy, distribute, and display the work;
- to make derivative works;
- to make commercial use of the work;

under the following conditions: Attribution:

- the original author must be given credit;
- for any reuse or distribution, it must be made clear to others what the license terms of this work are;
- any of these conditions can be waived if the authors gives permission.

Statutory fair use and other rights are in no way affected by the above.

The full version of the 'Beilstein-Institut Open Access License Agreement' is available at http://www.beilstein-journals.org/bjnano/submission/copyright.htm.

A.2 AIP permissions

License Number:	3398990749423
Publisher:	AIP Publishing LLC
Publication:	Review of Scientific Instruments
Article Title:	Analysis of rich inelastic electron tunneling spectra: Case study of terthiophene on Au(111)
Author(s):	B. Koslowski, N. Maurer, M. Stocker, S. K. Chulkov, D. M. Benoit, and P. Ziemann
Online Publication Date:	Apr 25, 2013
Volume Number:	84
Issue Number:	4
Type of Use:	Thesis/Dissertation
Requester Type:	Author (original article)
Format:	Print and electronic
Portion:	Figure/Table
Number of figures/tables:	1
Title of your thesis / dissertation:	Towards an *ab Initio* Description of Adsorbate Vibrations
Estimated size (number of pages):	120

License Number:	3398990470940
Publisher:	AIP Publishing LLC
Publication:	Journal of Chemical Physics
Article Title:	A fragment method for systematic improvement of anharmonic adsorbate vibrational frequencies: Acetylene on Cu(001)
Author(s):	Sergey K. Chulkov, David M. Benoit
Online Publication Date:	Dec 4, 2013
Volume Number:	139
Issue Number:	21
Type of Use:	Thesis/Dissertation
Requester Type:	Author (original article)
Format:	Print and electronic
Portion:	Excerpt (> 800 words)
Will you be translating?	No
Title of your thesis / dissertation:	Towards an *ab Initio* Description of Adsorbate Vibrations
Estimated size (number of pages):	120

License Number:	3398990596034
Publisher:	AIP Publishing LLC
Publication:	Journal of Chemical Physics
Article Title:	A fragment method for systematic improvement of anharmonic adsorbate vibrational frequencies: Acetylene on Cu(001)
Author(s):	Sergey K. Chulkov, David M. Benoit
Online Publication Date:	Dec 4, 2013
Volume Number:	139
Issue Number:	21
Type of Use:	Thesis/Dissertation
Requester type:	Author (original article)
Format:	Print and electronic
Portion:	Figure/Table
Number of figures/tables:	8
Will you be translating?	No
Title of your thesis / dissertation:	Towards an *ab Initio* Description of Adsorbate Vibrations
Estimated size (number of pages):	120

A.3 AIP terms and conditions

AIP Publishing LLC ("AIPP") hereby grants to you the non-exclusive right and license to use and/or distribute the Material according to the use specified in your order, on a one-time basis, or the specified term, with a maximum distribution equal to the number that you have ordered. Any links or other content accompanying the Material are not the subject of this license.

1. You agree to include the following copyright and permission notice with the reproduction of the Material: "Reprinted with permission from [FULL CITATION]. Copyright [PUBLICATION YEAR], AIP Publishing LLC." For an article, the copyright and permission notice must be printed on the first page of the article or book chapter. For photographs, covers, or tables, the copyright and permission notice may appear with the Material, in a footnote, or in the reference list.
2. If you have licensed reuse of a figure, photograph, cover, or table, it is your responsibility to ensure that the material is original to AIPP and does not contain the copyright of another entity, and that the copyright notice of the figure, photograph, cover, or table does not indicate that it was reprinted by AIPP, with permission, from another source. Under no circumstances does AIPP, purport or intend to grant permission to reuse material to which it does not hold copyright.
3. You may not alter or modify the Material in any manner. You may translate the Material into another language only if you have licensed translation rights. You may not use the Material for promotional purposes. AIPP reserves all rights not specifically granted herein.
4. The foregoing license shall not take effect unless and until AIPP or its agent, Copyright Clearance Center, receives the Payment in accordance with Copyright Clearance Center Billing and Payment Terms and Conditions, which are incorporated herein by reference.
5. AIPP or the Copyright Clearance Center may, within two business days of granting this license, revoke the license for any reason whatsoever, with a full refund payable to you. Should you violate the terms of this license at any time, AIPP, AIP Publishing LLC, or Copyright Clearance Center may revoke the license with no refund to you. Notice of such revocation will be made using the contact information provided by you. Failure to receive such notice will not nullify the revocation.
6. AIPP makes no representations or warranties with respect to the Material. You agree to indemnify and hold harmless AIPP, AIP Publishing LLC, and their officers, directors, employees or agents from and against any and all claims arising out of your use of the Material other than as specifically authorized herein.
7. The permission granted herein is personal to you and is not transferable or assignable without the prior written permission of AIPP. This license may not be amended except in a writing signed by the party to be charged.
8. If purchase orders, acknowledgments or check endorsements are issued on any forms containing terms and conditions which are inconsistent with these provisions, such inconsistent terms and conditions shall be of no force and effect. This document, including the CCC Billing and Payment Terms and Conditions, shall be the entire agreement between the parties relating to the subject matter hereof.

Related publications

1. S. K. Chulkov and D. M. Benoit, "A fragment method for systematic improvement of anharmonic adsorbate frequencies: Acetylene on Cu(001)", *J. Chem. Phys.*, **139**, 214704 (2013).

2. B. Koslowski, N. Maurer, M. Stocker, S. K. Chulkov, D. M. Benoit, and P. Ziemann, "Analysis of rich inelastic electron tunneling spectra: Case study of terthiophene on Au(111)", *Rev. Sci. Instrum.*, **84**, 043907 (2013).

3. D. M. Benoit, B. Madebene, I. Ulusoy, L. Mancera, Y. Scribano, S. Chulkov, "Towards a scalable and accurate quantum approach for describing vibrations of molecule-metal interfaces", *Beilstein J. Nanotechnol.*, **2**, 427–447 (2011).

Conference posters

1. S. K. Chulkov and D. M. Benoit, "Vibrational Properties of Thiophene in Gas Phase and on Surfaces", 46^{th} Symposium on Theoretical Chemistry, September 26-30, 2010, Münster, Germany.

2. S. K. Chulkov and D. M. Benoit: "Realistic Anharmonic Calculations for Molecules Adsorbed on Metal Surfaces", 47^{th} Symposium on Theoretical Chemistry, August 21-25, 2011, Sursee, Switzerland.

Acknowledgements

I would like to take this opportunity to thank all who support me during my doctoral program and especially:

- Dr. David M. Benoit for inviting me in his group and for his excellent guidance, helpful discussion and invaluable help with transfer to Hull;
- Dr. Norbert Maurer and Dr. Berndt Koslowski for recording the STM-IETS spectrum and for data analysis;
- Deutsche Forschungsgemeinschaft (DFG) (project SFB 569 TP - N1) and the University of Hull for financial support.
- bwGRiD initiative for millions of CPU·hours,
- All group members of the Theory Group SFB 569, the Theory of Condensed Matter Group, and the Surfactant and Colloid Group of the University of Hull and especially Bastian Boegel, Anupam Das, Dr. Mattias Desribats, Dr. Dominik Domin, Christopher Jay, Dr. Andrew Johnson, Dr. Kieron Taylor, Helmut Lang, Saeed Mashinchi, Dr. Luis Mancera, Christina Roggatz, Dr. Marius Rutkevicius, and Dr. Inga Ulusoy for enjoyable time;
- Dr. Ilya G. Ryabinkin, Dr. Dmitry S. Bezrukov, Dr. Alex Gaiduk, and Arseny Kovyrshin for motivation and enthusiasm;
- My parents, Konstantin Chulkov and Lyudmila Chulkova, all family members and relatives for inspiration and sincere support;
- Maxim Schmidt, Sergey Hofsetz, Dr. Igor Polyakov, Dr. Valentin Usachev, and many others for pleasant associations with Ulm.